THE CALCULATION OF FLUID FLOW THROUGH A TORQUE CONVERTER TURBINE AT STALL

By

Joachim Christoffel van der Merwe

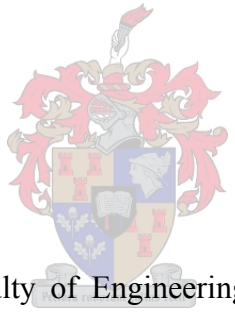

A thesis submitted to the faculty of Engineering, University of Stellenbosch, in partial fulfilment of the requirements for the degree of Master of Science in Engineering.

Thesis supervisor: Prof. TW von Backström
Department of Mechanical Engineering
University of Stellenbosch

November 2005

DECLARATION

I, Joachim Christoffel van der Merwe, the undersigned, hereby declare that the work contained in this thesis is my own work and has not been submitted for any degree or examination at any other university.

Signature of candidate

……

……. day of …… 2005

SUMMARY

The two-dimensional flow-field through the stationary blade row of a radial inflow turbine in a torque converter was analysed by means of a potential flow model and a viscous flow model. The purpose was to compare the accuracy with which the two flow models predict the flow field through the static turbine blade row. The freestream turbulence level necessary to optimise the accuracy of the viscous flow model was also investigated.

A first order source-vortex panel method with flat panels was used to apply the potential flow model. A radial inflow freestream was used. It was found that the stator blade row directly upstream of the turbine had to be included in the analysis to direct the flow at the turbine inlet. Even then the panel method did not satisfactorily predict the pressure distribution on a typical blade of the static 2nd turbine blade row.

A two-dimensional viscous flow model gave excellent results. Furthermore, the two-dimensional viscous flow model was simple to set up due to the fact that symmetry boundary conditions could be used. This facilitated useful predictions of the salient features of the two-dimensional flow through the middle of the radial turbine blade row.

OPSOMMING

Die tweedimensionele vloeiveld deur die statiese lemry van ’n radiale invloei turbine in ’n wringomsetter is met ‘n potensiaalvloei model en ’n viskose vloei model ontleed. Die doel van die studie was om die akkuraatheid waarmee die twee modelle die vloeiveld deur die statiese turbine lemry voorspel te vergelyk. Die vrystroom turbulensievlak wat nodig is om die akkuraatheid van die viskose vloeimodel te optimeer is ook ondersoek.

’n Eerste orde bron-werwel paneelmetode met plat panele is gebruik om die potensiaalvloei model toe te pas. ’n Radiaal invloeiende vrystroom is gebruik. Die stator lemry direk stroomop van die turbine lemry is in die analise ingesluit om die vloei by die inlaat van die turbine lemry te rig. Nogtans het die paneel metode nie die drukverdeling oor ’n tipiese lem van die statiese 2de turbine lemry van die toets wringomsetter bevredigend voorspel nie.

’n Twee-dimensionele viskose vloei model het uitstekende resultate gelewer. Die model was eenvoudig om op te stel omdat simmetriese randwaardes gebruik kon word. Dit het nuttige voorspellings van die belangrikste eienskappe van die vloei deur die middel van die radiale invloei turbine lemry moontlik gemaak.

ACKNOWLEDGEMENTS

I would like to express my grateful appreciation to some individuals and organisations who gave invaluable support in completing this project.

- Prof. T.W. von Backström for his patience, guidance and insightful suggestions.
- Dr. Thomas Harms for his assistance with the first paper that originated from this project.
- The Department of Transport and Public Works of the Provincial Administration of the Western Cape for financial support.
- My wife, Brenda Zondagh, for the loving encouragement and support that she continues to bestow so abundantly on her husband.

Big whirls have little whirls, which feed on their velocity, and little whirls have lesser whirls, and so on to viscosity. (Richardson, 1922).

DEDICATED TO MY WIFE

Brenda, I love you.

CONTENTS

LIST OF FIGURES

LIST OF TABLES

LIST OF SYMBOLS

Roman symbols

C_p	Dimensionless pressure coefficient: equation (3-5)
$C_i(x,y)$	Source influence coefficient, equation (3-28)
$\boldsymbol{G}$	Gravitational acceleration in vector form
$G_i(x,y)$	Vortex influence coefficient, equation (3-36)
$\sqrt{g}$	Determinant of metric tensor
H	Enthalpy
I	Freestream turbulence level, equation (4-17)
K	Thermal conductivity
k	Turbulence kinetic energy: equation (4-6)
l	Index number (Chapter 3),characteristic length (Chapter 4).
p	Pressure [N/m^2], Static pressure
r	Distance of a singularity from the origin of the coordinate system.
s	Surface coordinate
s_i	Momentum component source term
s_m	Mass source term
s_{ij}	The rate-of-strain tensor, i = 1, 2, 3 and j = 1, 2, 3
S	Total distance along a surface
t	Time
$\boldsymbol{T}$	Unit normal tangential vector
T	Temperature
U	Mean freestream speed
u, v, w or u_i	Cartesian velocity components in direction x_i, i = 1, 2, 3
$\tilde{u}_i$	$u_j - u_{cj}$ the relative velocity between the fluid and the local coordinate frame that moves with velocity u_{cj}
$\mathbf{V}$, V	Velocity vector, speed (scalar value)
v^*	$(\tau_w/\rho_w)^{1/2}$ wall-friction velocity
x, y, z or x_i,	Cartesian coordinates, i = 1, 2, 3

y^+	$\frac{\rho u_\tau y}{\mu}$, with $u_\tau = \sqrt{\frac{\tau_w}{\rho}}$ the so-called friction velocity

Greek symbols

α	freestream flow angle
γ	Vortex strength per unit length
ε	Turbulent dissipation, equation (4-7)
η, ξ	Position coordinates of a potential singularity
θ	Panel angle
μ	Molecular viscosity
ν	Kinematic viscosity
ρ	Density
τ_{ij}	Stress tensor
ϕ	Disturbance velocity potential
Γ	Circulation
Λ	Source strength

Dimensionless groups

C_p	Pressure coefficient: $C_p \equiv \frac{p - p_\infty}{\frac{1}{2}\rho_\infty V_\infty^2}$

Subscripts

CS	Control surface
CV	Control volume
Eff	Effective
P	Constant pressure
Surf	Surface
T	Turbulent
T	Constant temperature
w	At the wall or boundary
∞	Far field or some appropriate reference point

Superscripts

-	Averaged time
′	Turbulent fluctuation, value per unit span, differentiation
+	Law-of-the-wall variable

Special symbols

δ_{ij}	Kronecker delta, (1 if $i = j$; 0 if $i \neq j$).
$\frac{D}{Dt}$	Particle differential $\frac{\partial}{\partial t} + (\mathbf{V} \cdot \nabla)$
∇	Del operator: $(\ )_{,i}$

Chapter 1

BACKGROUND

1.1. INTRODUCTION

The study of fluid flow in the flow circuits of torque converters is fascinating and ever evolving. Researchers in this field are confronted with an extremely complex flow field. Until recently designers relied on fairly simple one-dimensional techniques to design new torque converters. Due to increasingly stringent economic and operational requirements the demand for more efficient and smaller designs intensified. In order to satisfy this demand it is imperative to study the fluid flow characteristics of torque converters very closely. The blossoming of numerical methods in fluid flow analysis added further impetus to the study of fluid flow in torque converter flow circuits. In vogue with this trend, the objective of this project is to study the flow through the second blade row of a torque converter by means of computational fluid dynamics. This is done by comparing the results of a two-dimensional viscous and a two-dimensional potential flow model and drawing conclusions about the applicability of each to the section of the torque converter under investigation.

1.2. BASIC PRINCIPLES OF TORQUE CONVERTERS

A torque converter is a hydrodynamic device that smoothly transfers mechanical power, often from an engine to a gearbox system. Its primary function is torque multiplication. For the main part of its operating range it produces a larger torque on its output shaft than the torque applied to its input shaft. The maximum torque multiplication ratio, which may be as high as 3.5, occurs at stall and decreases without step to a value of unity as the angular velocity of the turbine approaches the angular velocity of the pump.

Foettinger developed one of the first torque converters in the early part of the twentieth century for ship propulsion [Wislicenus (1965) and Jandasek (1963)]. Since

then, torque converters came into widespread use. They were developed for a vast variety of applications including earth-moving plant, passenger cars, busses, diesel train locomotives and military vehicles.

1.2.1. Geometrical arrangement

Torque converters belong to the class of transmission devices known as hydrodynamic transmissions. A hydrodynamic transmission transfers mechanical power by means of momentum changes in a closed fluid circuit.

Figure (1-1), derived from Strachan et. al. (1992), illustrates the arrangement of a typical three-element torque converter. It consists of the three elements present in all torque converters namely the stator, impeller and turbine. The impeller is attached to the power-input shaft, the turbine to the power-output shaft and the stator to the grounded member. The pump may be a mixed flow or centrifugal pump and is directly attached to the driven shaft. The turbine, which may also be of the mixed flow or radial inflow type, is attached to the power output shaft. If only a pump and a turbine element are present, the device is classified as a fluid coupling. The feature that distinguishes a torque converter from a pure fluid coupling is the presence of the stator and the ability of torque multiplication that it imparts. The stator may be of an axial flow, mixed flow or radial flow type. It is attached to a non-rotating member, usually by means of a one-way clutch.

In order to improve efficiency, a torque converter may also be equipped with a lock-up clutch. It is a device that couples the turbine and pump directly to each other in order to transmit torque from the power input shaft mechanically to the power output shaft. In this way the inefficiencies attached to power transmission through the torque converter fluid circuit are eliminated.

Low viscosity oil is usually used as the working fluid in torque converters. It serves as a lubricant and is dense enough to ensure that relatively low angular velocities are sufficient for the necessary momentum transfer between the pump, turbine and stator elements. The oil completely fills the flow passages inside the torque converter.

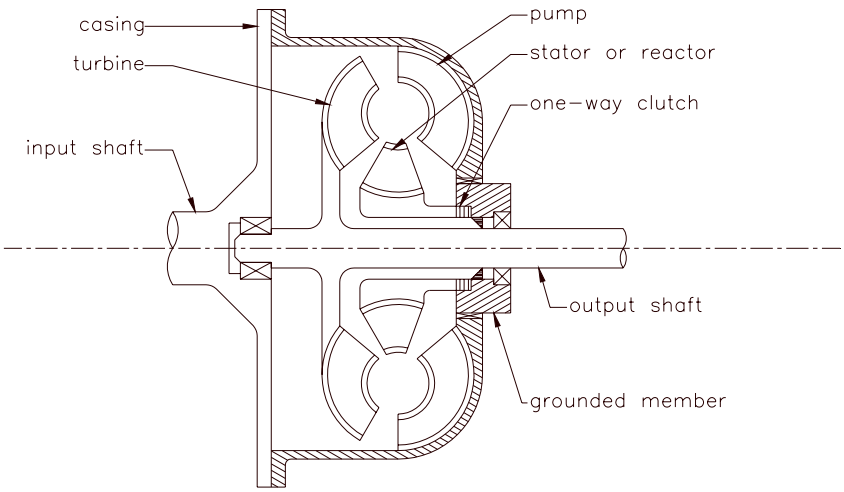

Figure 1-1. A typical three-element torque converter.

1.2.2. Internal operation

The flow in a torque converter follows an intricate route through the torque converter elements. These elements operate in a closed fluid circuit and are arranged symmetrically around a common axis as shown in figure (1-1).

The fluid enters the pump at the pump intake near its centre and is forced through the pump impeller channels until it is discharged at the pump outlet. In the process the pump changes the average linear and angular momentum of the fluid. From the pump outlet the fluid is turned back in the direction of the common axis of rotation and flows into the turbine inlet. Through the turbine it flows towards the centre of the torque converter. The turbine vanes change the average angular momentum of the fluid which causes reaction forces on them. These reaction forces on the turbine vanes impart a torque on the turbine shaft. From the turbine outlet the fluid flows through the stator where it exits the stator axially with respect to the common axis of rotation. The stator also changes the angular momentum of the fluid before it is discharged back into the pump intake to repeat the flow cycle.

The flow path described above, in which the tangential motion of the fluid with respect to the common axis is neglected, is the meridional flow path. The fluid also has a tangential velocity component with respect to the common axis of rotation due to the rotation of the pump and turbine. The flow path caused by the tangential ve-

locity component superimposed on the meridional flow path through the torque converter elements, results in a helical flow path in a toroidal envelope through the pump, stator and turbine elements surrounding the common axis of rotation.

The vanes of the stator are angled in such a way that the external torque exerted on the grounded member to keep it stationary must be applied in the same direction as the external torque exerted on the pump impeller's shaft. Considering only the external moments exerted on the pump, turbine and stator, it is clear that under steady state operating conditions the magnitude of the external moment on the turbine is equal to the magnitude of the external moments on the pump and stator combined. The direction of the external moment applied to the turbine is in the opposite direction of the external moments applied to the pump and stator. Consequently, the stator increases the output shaft torque. Air friction on the outside of the torque converter is usually insignificant in comparison with the three main externally applied torque vectors under discussion and need not be taken into account here.

The operating conditions of a torque converter can be classified into four distinct categories. These are torque multiplication, fluid coupling, mechanical coupling and coasting conditions. The torque multiplication mode occurs while the turbine is stationary or runs significantly slower than the pump. For a specific pump rotational speed, the fluid velocity in the meridional plane is a maximum when the turbine is stationary. This is the stalled state. Because the turbine shaft is stationary, the turbine shaft does no work. In this case the efficiency of the torque converter, which is the ratio of the work done by the turbine shaft to the work done on the pump shaft, is zero. The stalled condition is responsible for one of the salient parameters of torque converters namely the maximum torque ratio. It is therefore an important aspect of torque converter performance that needs careful investigation.

When the turbine begins to turn against the braking torque, the turbine shaft begins to deliver power. The efficiency of the torque converter therefore increases from zero. However, as the speed of the turbine increases, the fluid begins to whirl around the common axis of rotation with the pump and turbine. This causes the build up of a centrifugal head that counters the head of the pump impeller. This decreases the mass flow rate in the meridional flow path. The increase in the mean

tangential velocity in the direction of the spinning turbine and pump blades and the decrease in the velocity in the meridional flow path cause the angle of attack of the stator blades as well as the mean flow speed through the stator blades to decrease. Consequently, the changes in angular momentum and thus the reaction force on the stator decreases. As the speed of the turbine is allowed to increase further, the angle with which the fluid enters the stator eventually reaches a point where the torque exerted on the stator becomes zero. This implies that the torque magnitude on the turbine shaft has diminished to the point where it equals the torque magnitude on the pump shaft. Thus, while the turbine increases its speed from the stalled state the torque ratio decreases from its maximum at the stalled state to unity. When the torque ratio reaches unity, the torque converter is operating at its coupling point. Now it almost operates like a fluid coupling due to the fact that the stator plays no significant role from this point on. If the turbine speed increases further, the one-way clutch of the stator allows it to rotate freely to prevent the stator from interfering with the operation of the torque converter. This is the coasting condition. The torque and efficiency curves shown in figure (1-2) are those of the Borg & Beck WH11 torque converter coupled to a Perkins 1004-4T C1550 engine and are typical of torque converters in general.

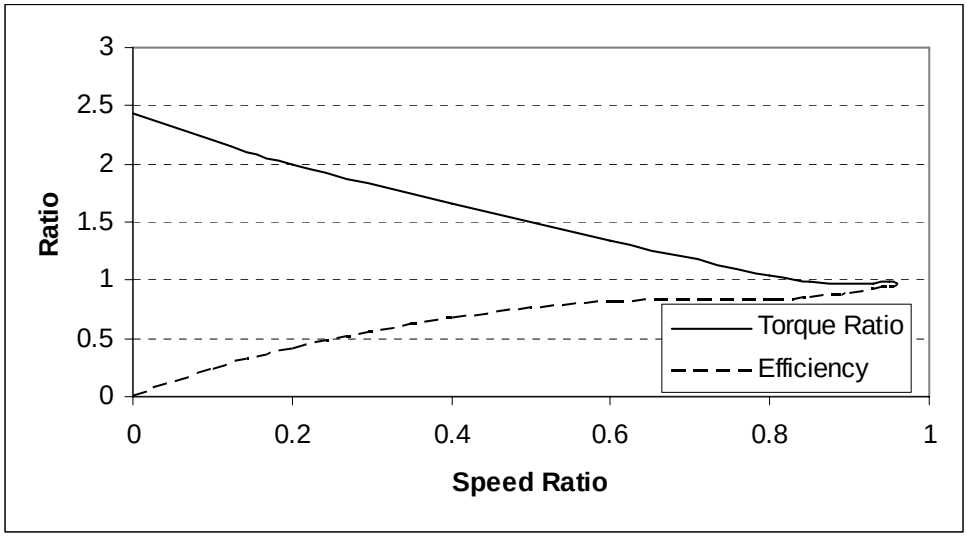

Figure 1-2. Torque ratio and efficiency of a Borg & Beck WH11 torque converter.

Finally, a torque converter operates in the mechanical coupling state when the clutch that is splined to the turbine is engaged. This provides a direct mechanical coupling between the pump and turbine. This eliminates the small amount of slippage during the fluid coupling state and results in a more efficient transmission of mechanical power.

1.3. PURPOSE OF THE THESIS

1.3.1. Background

Although a torque converter is structurally a relatively simple device, it has an extremely complex internal flow field. The flow circuit is three-dimensional and completely enclosed by a core and a shell that form a doughnut-shaped ring. It is lined with at least three close-coupled blade rows. The oil in the flow circuit is viscous and incompressible and is being continuously recirculated. The incompressible fluid causes pressure disturbances to propagate three-dimensionally through the flow field. The closely spaced blade rows cause time dependent interaction effects. The blade rows also operate under widely varying conditions with angles of attack that may vary by as much as 90 degrees or more through the operating range. The flow may be two-phased due to cavitation that occurs under certain operating conditions. Viscous interaction occurs within the narrow blade rows, at clearance gaps and between casing and blade. Due to these geometrical and operational properties the flow field is dominated by significant levels of freestream turbulence that can be in the order of 5% or more [Marathe et. al. (1996)], local boundary layer separation, vortices, blade wakes, unsteadiness and high local pressure and velocity gradients.

In the quest for more efficient designs, shorter design times and more compact designs for applications where space is a premium an improved grasp of the flow field is an essential prerequisite. Competition requires more careful optimisation of designs. For example, the premium placed on space in automotive engineering requires that torque converters must be axially as compact as possible. Where the axial length to diameter ratio was traditionally roughly 0.3, it decreased to as low as 0.23 in later designs (By and Mahoney, 1989). The cross section of the flow circuit also changed from a nearly circular shape as shown in figure (1-1) to an elliptical

shape as the axial length to diameter ratio of the later designs diminished. An example of a flow circuit cross section with a highly elliptical shape is shown in figure (A-1) in appendix A. Designers must be able to analyse the effects of design changes on a flow field in order to quickly and efficiently improve their designs.

1.3.2. Research and development.

The techniques employed in the design process to predict the properties of a torque converter differ in sophistication. Design technologies that are employed during different stages of the design of turbo machinery can be grouped into three different classes. These are

- one-dimensional **streamline theory** enhanced by **empirical loss models** and correlations of experimental torque converters,
- two- and three-dimensional **potential flow analysis** with or without interactive boundary layer analysis and
- two- and three-dimensional **viscous numerical analysis** based on the complete Navier-Stokes equations.

Until the early eighties of the 20th century, the design of torque converters was based mostly on the one-dimensional model of performance analysis, the overall performance data of previously built torque converters and a scaling method (By and Mahoney, 1989). Jandasek (1962) describes an exemplary design procedure that utilises these methods. Houchun and Oh (1999) reports that much work has been done in this regard since the early 1940's, for example by Eksergian (1943), Spannhake (1949), Ishihara and Emori (1966) and Kotwicki (1982). This approach led to several difficulties however:

- It is expensive and time consuming to develop an entirely new torque converter that works satisfactorily.
- Torque converters can be scaled from well-designed models only as long as they are geometrically similar.
- Experiments are an effective means of measuring global parameters like drag, lift and pressure coefficients. For improved designs, however, it is also important to concentrate on the details of the flow field, like flow separation and vortices. To analyse these phenomena experimentally may prove to be too costly

and, in some cases, even impossible due to the local flow interferences caused by probes in the flow field. To study the details that are due to geometry and eventually, fluid viscosity too, streamline theory does not suffice.

To cater for the shortcomings of the one-dimensional model, potential flow analysis and viscous flow analysis are employed on an ever-increasing scale. Until about 1980 pure experimental and classical theoretical fluid dynamics were the research tools available to fluid dynamics practitioners. Since then, the development of computer hardware and software reached a stage where the hitherto experimental science of computational fluid dynamics came of age and became a full-fledged third partner in the triad of research tools now available to designers of torque converters.

The reasons for the ascendance of computational fluid dynamics, or CFD in short, are varied and numerous. Computational fluid dynamics opened new avenues of research that were not possible with the two traditional approaches. Numerical experiments can now be conducted of flow situations that could not hitherto have been conducted by the traditional methods. The low cost of an analysis project, the speed with which an analysis can be done, the ability to study a complete flow field and the ability to simulate the real condition instead of having to use a scale model further contributed to the increasing popularity of CFD. For these reasons CFD is an ideal tool with which to study the flow field inside torque converters since it does not suffer from the drawbacks of the experimental and theoretical methods.

Research in the industry and at universities into the complexities of the flow field inside a torque converter continues unabated. It involves both surface pressure measurements, flow field pressure measurements and flow field velocity measurements. Pressure measurements on the surface of blades were done by By and Lakshminarayana (1991) and (1995). Bahr et al. (1990), Brun et al. (1996), Marathe et al. (1996) and Gruver et al. (1996) conducted velocity measurements. This research shed new light on the complexities of the flow field and led to suggestions for improvements by Von Backström and Lakshminarayana (1996). Dedicated computational fluid dynamics programs were developed by researchers like Schulz et al. (1996), Marathe et al. (1996) and By et al. (1995) to study specific details of the flow field.

1.3.3. Local work

At South African universities, Lamprecht (1983), Reynaud (1991) and Groiss (1991) developed one-dimensional prediction models, enhanced by empirical correlations. Strachan et al. (1992) introduced a new incidence loss model that takes blade thickness into account. The torque converter's geometry and fluid properties must be entered into these models. They predict the performance characteristics like torque ratio and efficiency. One-dimensional models like these may be used in the preliminary design stages to design the basic layout of a new torque converter.

Venter (1993) furthered the earlier research by contributing to the second class of design technologies referred to in section 1.2.2. The fluid in the torque converter is approximated as incompressible and inviscid while the flow field is modelled as irrotational, steady and two-dimensional. This allowed the use of a two-dimensional panel method to predict the pressure distribution on a blade of an isolated stationary turbine blade row. The aim was to develop a tool with which to study and refine the design of single blade rows. Venter (1993) modelled the second turbine blade row of the experimental torque converter in isolation surrounded by a free spiral vortex as a freestream. The panel method did not predict the measured entrance velocity direction and the pressure distribution on a turbine blade very accurately.

1.3.4. Thesis aims

The primary objective of this thesis is to supplement the local research work by making a contribution to the second and third class of design technologies. As stated in section 1.2.2, this encompasses the application of inviscid and viscous flow models to the torque converter flow field. Both the viscid and inviscid flow models employed here share the assumption that the fluid in the torque converter flow field is incompressible. This assumption together with the assumption that the flow is irrotational enable the reduction of the inviscid model to the potential flow model as will be explained in chapter 2. This model can be applied by means of a panel method. Initially, only the viscous flow model was employed due to the failure of the panel method to accurately predict the pressure distribution on a turbine blade as demonstrated by Venter (1993). However, due to the success achieved by the vis-

cous flow model when the influence of the upstream stator blade row was taken into account together with a radial inflow freestream [Van der Merwe et. al. (1996)] it was decided to extend the research to test the performance of the panel method with the inclusion of the stator blade row too. The aims of the thesis are therefore to

- Implement the potential flow model by means of a panel method and develop it to handle multiple bodies in a radial freestream.
- Develop a Windows based computer program to implement the panel method.
- Validate the Windows based computer program.
- Include the stator in the analysis of the second turbine flow field and compare the results of the two-dimensional potential flow model, applied by means of a panel method with empirical results. Conclusions must then be drawn regarding the applicability of this model to the flow field inside a torque converter.
- Compare the results of the two-dimensional viscous flow model, applied by means of a commercial CFD program with empirical results and draw conclusions regarding the applicability of this model to the flow field inside a torque converter.
- Make recommendations regarding the applicability of the two dimensional viscous and potential flow models to the flow field inside a torque converter. It is hoped that one or both of these simple, inexpensive methods can be utilised to make useful predictions of the salient flow field characteristics through some blade rows of torque converters.

The computer resources available restricted the research to a two-dimensional model that includes at the utmost two consecutive blade rows. Bearing in mind that viscous three-dimensional effects dominate the flow field of the torque converter, an area of the torque converter flow field had to be chosen that might be amenable to two-dimensional analysis. Venter (1993) and Steenkamp (1996) obtained empirical data of the flow in the region of the second turbine blade row of an experimental torque converter. This torque converter is concisely described in appendix A. From figure (A-1) it is clear that the geometry in this area as well as in the area around the stator blade row that precedes it is almost completely two-dimensional. The region at the trailing edges of the second turbine blade row begins to turn toward the intake side of the pump and departs from the two-dimensional geometry that precedes it. It

is only a small part of the two-dimensional region around the stator blade row and the second turbine blade row though. This then is the ideal place where a two-dimensional flow model may be applied in the complex flow field inside a torque converter. The availability of empirical data with which to compare the predicted results of the potential flow model and the viscous flow model enables the necessary comparisons between predicted and empirical data to be made. The flow field surrouding the second turbine blade row will therefore be calculated with the stator blade row included due to the influence it might have on the flow field under study by virtue of its close proximity to the second blade row.

1.4. THE STATOR AND SECOND TURBINE BLADE ROW.

The geometrical specifications of the blade rows involved are needed to specify the boundary values of the fluid flow models described in chapters 3 and 4. These blade rows are the stator and the second turbine blade rows. The Department of Mechanical Engineering of the University of Stellenbosch supplied the design data.

The second turbine blade row of the experimental torque converter has 20 blades that are uniformly spaced in an axial symmetric cascade. The profiles are constructed from arcs and straight lines which are depicted in table (1-1) and figure (1-3). The stator blade row consists of 48 blades. A stator blade is depicted in figure (1-4) with the data of the arcs and lines depicted in table (1-2).

In the tables, the subtended angle is the angle subtended by the blade segment. The radius is the radius of the circle that is used to construct the blade segment. The circle's centre coordinates are given by the circle centre x coordinate and circle centre y coordinate in the tables. Only the blade segments consisting of arcs have subtended angles, radiuses and circle centre coordinate points. The segment start x coordinate and segment start point y coordinate give the starting point coordinates of the segment. The segment ends at the starting point of the next segment.

Blade segment	Sub-tended angle	Ra-dius	Circle centre x coordinate	Circle cen-tre y coor-dinate	Segment start point x coordi-nate	Segment start point y coordi-nate
line a					-84.84	6.87
arc b	14.11	86.56	-140.53	72.82	-85.20	6.25
arc c	40.00	22.14	-112.63	14.76	-103.1	-5.23
arc d	31.82	14.09	-114.72	6.98	-118.17	-6.68
arc e	134.31	4.02	-121.98	0	-124.86	-2.81
arc f	12.84	20.13	-121.78	-16.11	-121.98	4.02
line g					-117.5	3.56
arc h	42.24	38.25	-104.14	39.90	-112.05	2.47

Table 1-1. Curves of the second turbine blade.

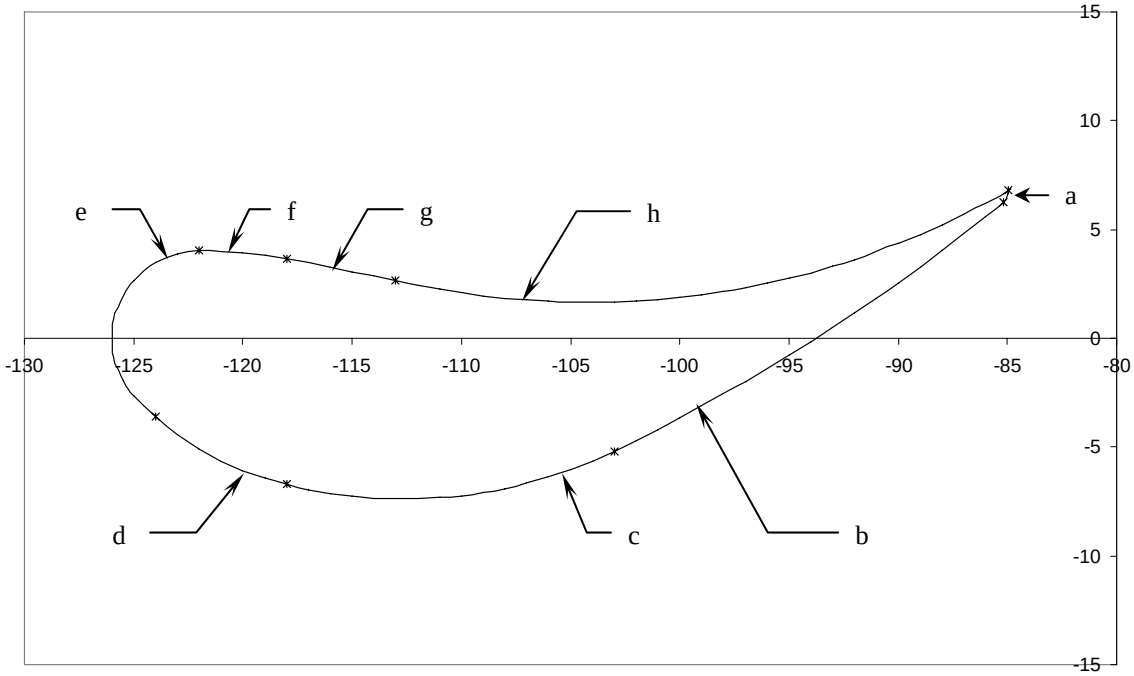

Figure 1-3. Second turbine blade.

Blade segment	Sub-tended angle	Ra-dius	Circle centre x coordinate	Circle centre y coordinate	Segment start point x coordinate	Segment start point y coordinate
line a					-132.96	-12.98
arc b	12.17	69.96	-197.64	-39.33	-133	-12.58
arc c	51.30	5.81	-144.87	-2.85	-140.09	0.44
arc d	128.72	2.95	-144.68	0	-144.45	2.94
arc e	32.71	4.53	-143.37	0.88	-147.12	-1.66
line f					-145.15	-3.28
arc g	37.34	20.38	-150.66	-23.09	-142.72	-4.32

Table 1-2. Curves of the stator blade.

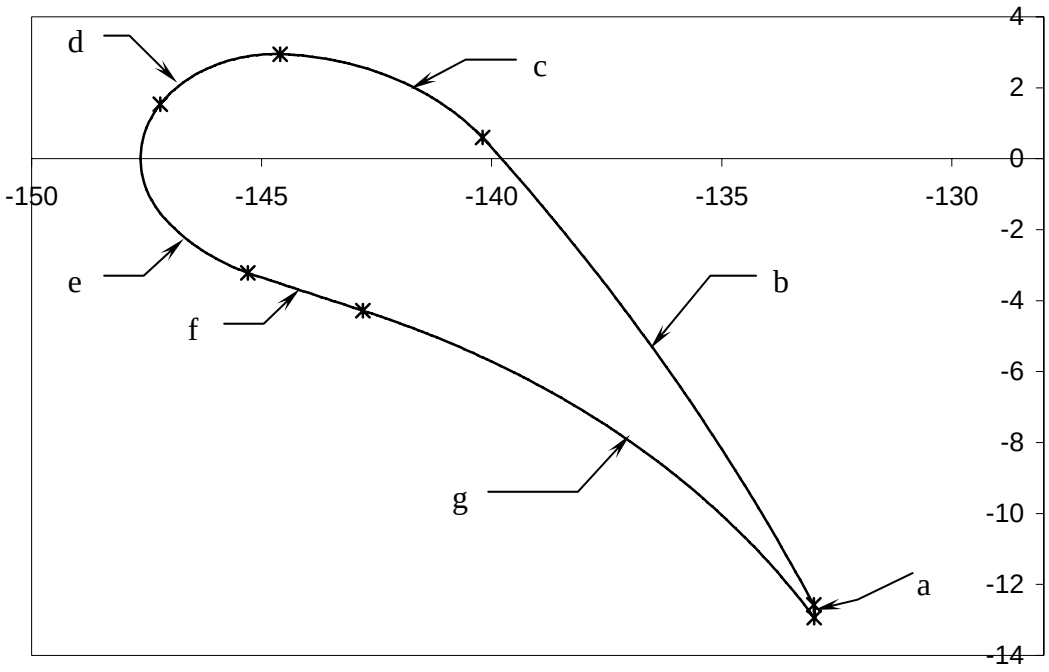

Figure 1-4. Stator blade.

1.5. OUTLINE OF THE THESIS

Chapter 1 provides the background and the aims of the thesis. Chapter 2 describes the flow models applied to the flow through the torque converter's second turbine when stalled. The applicability of inviscid flow models on the flow in the torque converter is discussed. The shortcomings of the inviscid flow model and the reasons for using viscous flow models are also discussed. The parameters that define the properties of the working fluid in the experimental torque converter are chosen and motivated. Measurements reported in the literature, such as Bahr, et. al. (1990), show that the turbulence levels present in the torque converter flow field is significant. Therefore, aspects of turbulence and parameters related to its modelling at the inlet boundaries are explained.

Chapter 3 describes the application of the panel method to analyse the two-dimensional flow field through the second blade row of the torque converter. The application of a first order source-vortex based panel method to a single body in a freestream is explained. The method is then extended to handle multiple bodies in a freestream. This method is further improved to handle multiple bodies in both a lin-

ear and a radial flow field. The bodies can be arranged at random. Conclusions about the applicability of the model to the flow field under scrutiny are drawn.

The application of a two-dimensional viscous flow model is described in chapter 4. The theory underlying the commercial computational fluid dynamics program, Flo++ 3.02, is concisely discussed.

The empirical data obtained by Venter (1993) and Steenkamp (1996) in the vicinity of the second turbine blade row of the experimental torque converter is used to evaluate the validity of both the inviscid and viscous flow models as applied by means of the panel method and Flo++ respectively in chapters 3 and 4.

Chapter 5 contains the most important conclusions gleaned from the preceding analysis as well as recommendations for further research in torque converters.

Chapter 2

FLUID AND FLOW FIELD MODELLING

2.1. Introduction

To solve any flow problem the governing equations of fluid flow needs to be solved. In this instance, the equations need to be solved for the flow field surrounding the second turbine blade row. This chapter presents the governing equations and shows the need to simplify them. Computational fluid dynamics is recommended as a practical method to predict the forces on the second turbine blade row in chapters 3 and 4. In this way, the primary goal of this thesis, namely to investigate the applicability of various viscous and inviscid flow models to the flow fields inside torque converters, is achieved.

2.2. Fundamental equations of fluid flow.

The equations that control viscous fluid flow are generally considered to consist of three basic relations supplemented by four auxiliary relations (White, 1991). The three basic equations are the three laws of conservation for physical systems applied to a suitable fluid model. These three laws are the conservation laws of mass, momentum and energy.

Applying the law for the conservation of mass to an infinitesimal fluid element moving along a streamline yields the continuity equation:

$$\frac{D\rho}{Dt} + \rho \nabla \cdot \mathbf{V} = 0 \qquad (2\text{-}1)$$

The momentum equations results from applying the law of the conservation of momentum to the same fluid model as above: The momentum equations for a viscous flow are known as the Navier-Stokes equations:

$$\rho\frac{D\mathbf{V}}{Dt}=\rho\mathbf{g}-\nabla p+\frac{\partial}{\partial x_j}\left[\mu\left(\frac{\partial u_i}{\partial x_j}+\frac{\partial u_j}{\partial x_i}\right)+\delta_{ij}\lambda\mathrm{div}\mathbf{V}\right] \tag{2-2}$$

The energy conservation law yields the third basic equation, the energy equation, which is included here just for completeness:

$$\rho\frac{Dh}{Dt}=\frac{Dp}{Dt}+\mathrm{div}\left(k\nabla T\right)+\left[\mu\left(\frac{\partial u_i}{\partial x_j}+\frac{\partial u_j}{\partial x_i}\right)+\delta_{ij}\lambda\mathrm{div}\mathbf{V}\right]\frac{\partial u_i}{\partial x_j} \tag{2-3}$$

White (1991) and Schlichting (1979) among others, give detailed derivations of these equations. Frederick and Chang (1972) derived these equations from a continuum mechanical perspective using Einstein's tensor notation.

From this set of equations the velocity $\mathbf{V}(x,y,z,t)$, thermodynamic pressure $p(x,y,z,t)$ and absolute temperature $T(x,y,z,t)$ must be solved simultaneously for a given set of boundary conditions. The values of **V**, *p* and *T* must be specified for each point on the boundary of the flow field. The three basic equations also contain the thermodynamic variables density ρ, enthalpy *h*, thermal conductivity *k* and viscosity μ. These thermodynamic variables are determined by the two thermodynamic values of *p* and *T*:

$$\rho=\rho(p,T) \tag{2-4a}$$

$$\mu=\mu(p,T) \tag{2-4b}$$

$$h=h(p,T) \tag{2-4c}$$

$$k=k(p,T) \tag{2-4d}$$

The four auxiliary relations (2-4) are equations of state that are valid under conditions of local thermodynamic equilibrium.

In the development of a mathematical model, it is important to note under what conditions the model is valid. Thus far, the conditions under which this system of equations holds are

- The fluid forms a mathematical continuum.
- The fluid is in thermodynamic equilibrium.
- The only body forces are due to gravity.

- Heat conduction follows Fourier's law.
- There are no internal heat sources.
- The stress is proportional to the time rate of strain, i.e. the fluid is Newtonian.

2.3. The need for numerical analysis

The governing equations for viscous fluid flow that are concisely discussed in section 2.2 are a coupled system of nonlinear partial differential equations. No general analytical method for solving them for an arbitrary viscous flow field exists except for some special geometries (White, 1991). These special geometries and fluid properties allow simplifications to be made that uncouple the energy equation from the continuity and momentum equations. It further cause some terms of these equations to become zero or negligibly small. In almost all practical cases however not even the simplified equations can be solved analytically. Computational fluid dynamics (CFD) affords a way to solve the equations accurately enough for practical purposes.

CFD does not yield exact results however. Three sources of error are inherent in a CFD analysis to some extend:

- **Modelling errors** are caused by the approximating simplifications that are made to the governing fluid flow equations as described in section 2.2.
- **Discretisation errors** are caused by discretising the conservation equations of the fluid flow model. These errors are defined as the difference between the exact solution of the mathematical model's equations to be discretised and the exact solution of the algebraic system of equations obtained by the discretising process.
- **Convergence errors** that are caused by the difference between the exact solution of the discretised algebraic equations and the actual numerical results obtained. Errors caused by numerical truncation, limited number of iterations and spacing of discrete points where the equations are applied are included under this heading.

2.4. The need to simplify the governing equations of fluid flow

Laminar flows can be computed almost exactly by direct numerical analysis on a digital computer. Turbulent flows contain such fine detail that they can currently be computed by direct numerical analysis only for very low Reynolds numbers. This method is very expensive and requires very expensive and sophisticated computers. It also produces much more detailed information of the flow field than what is normally required. Direct numerical analysis is therefore totally impractical for the purposes of this project. The introduction of simplifying assumptions into the governing equations are therefore necessary to develop practical flow models. These simplifications give rise to two broad groups of flow models namely an inviscid flow model and a viscous flow model based on Reynolds averaging together with a suitable viscosity model.

The viscous flow model is applied throughout the flow field. It is widely applicable and generally gives excellent results. Its accuracy is influenced to some extent by the applicability of the viscosity model to the boundary conditions that pertain. Observing that the effects of viscosity in high Reynolds number flows are restricted to a thin boundary layer on the solid surface allows the simplification of this model. The thin boundary layer in which viscous effects dominate is described by boundary layer theory. Outside the boundary layer the flow is essentially inviscid and irrotational. The pressure at a specific position on a body varies negligibly through the boundary layer in high Reynolds number flow regimes. Under such flow conditions therefore, inviscid flow theory can be used to predict the measured surface pressure distribution at solid walls while boundary layer theory can be used to predict the shear stress on the wall. Boundary layer theory will also predict boundary layer separation. This viscous boundary layer model loses its accuracy in the presence of boundary layer separation though.

If the only information desired is the pressure distribution on the bodies in the freestream it is practical and customary to use inviscid flow theory in well behaved high Reynolds number flows with an essentially irrotational freestream. In these cases inviscid, irrotational flow theory simplifies the mathematical model to such an extent that simple numerical models like the panel method for incompressible flow

or the method of characteristics for compressible flow can be devised for predicting the pressure distribution.

In many cases the assumption of an irrotational flow field through our torque converter is problematic though. In the complex flow field inside a torque converter, the assumption of inviscid, irrotational flow is not entirely accurate. Significant levels of freestream turbulence that can be as high as 5% have been measured inside torque converters. Wakes from the close proximity stator as well as hub and shroud boundary layers occur in the flow field. It behoves us therefore to investigate and compare the accuracy of the mathematical model that takes viscosity into account with the accuracy of the simple inviscid, irrotational and incompressible model. The accuracy of these models is determined by comparing their results with empirical data.

2.5. Simplifying assumptions

The following assumptions are made to arrive at a tractable viscous flow model and a potential flow model.

2.5.1. Temperature

Assumption: $T = 40°C$

Motivation: Venter (1993) and Steenkamp (1996) acquired the empirical data used in this project. Venter (1993) made his measurements by keeping the working fluid in the experimental torque converter at 35 to 40°C. It is not known at what working fluid temperature Steenkamp (1996) made his measurements. Both these researchers used the same experimental set-up with water as the working fluid. Appendix A concisely describes the experimental set-up. It is therefore assumed that Steenkamp (1996) also ensured that the temperature of the working fluid remained in the region of 40°C when he acquired his data.

The influence of a 5°C variation in water temperature on density and molecular viscosity is illustrated in figure (2-1). The water density varies with 0.15% and the molecular viscosity with 11.8% between 35°C and 40°C. Although the variation in

density is negligible, the variation of almost 12% in molecular viscosity requires further investigation regarding its influence on the predicted flow field.

Viscosity only plays a role in the viscous flow model. The turbulence model used in the viscous flow analysis adds a perceived turbulent eddy viscosity to the molecular viscosity of the fluid. The effective viscosity used in the viscous flow model is the sum of the molecular viscosity of the fluid and the perceived turbulent eddy viscosity of the flow field. This model is discussed in chapter 4. The perceived turbulent eddy viscosity of the flow field is defined by equation (4-10). This view of the influence of turbulence on the flow field causes a much higher effective viscosity than the molecular viscosity of the water alone.

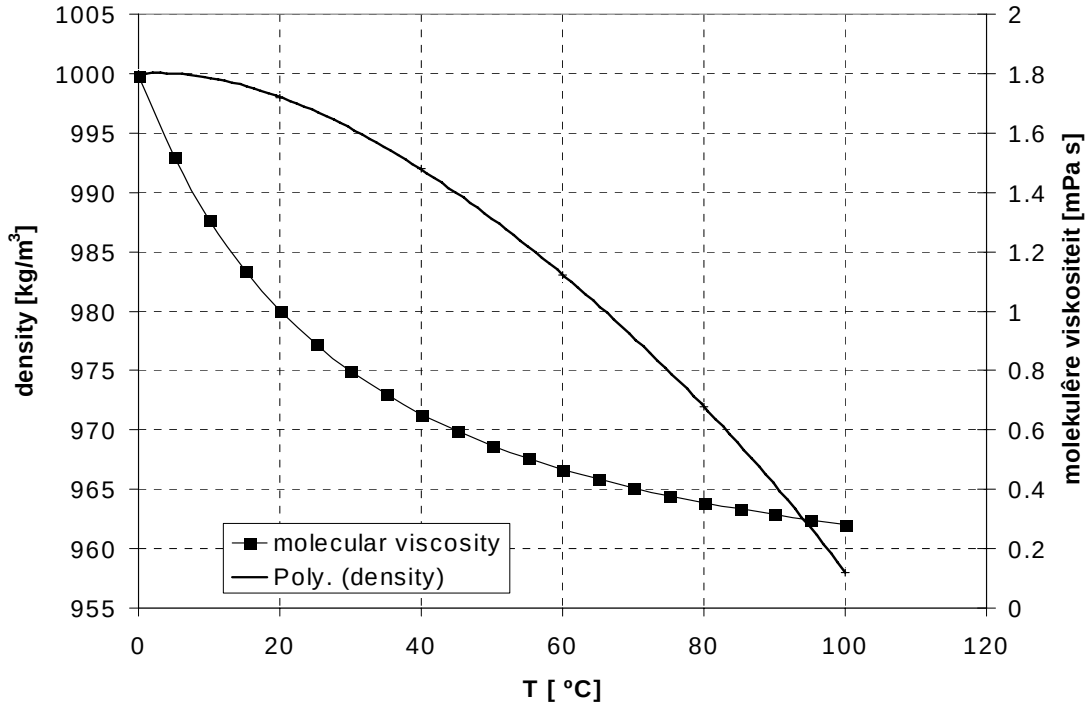

Figure 2-1. Influence of temperature on water density and viscosity.

According to White (1991) the turbulent eddy viscosity in a turbulent flow field is in the order of ten to hundred times larger than the molecular viscosity. Rodi (1980) also states in this regard that in most flow regions the turbulent stresses and fluxes are much larger than their laminar counterparts that are therefore often negligible. Therefore, a significant variation like 12% in the molecular viscosity actually influences the effective viscosity in the turbulent flow field by less than 1% which is insignificant enough for engineering purposes. The temperature of the working fluid

is then assumed to be a constant because of the negligible influence that a variation of between 35°C and 40°C has on the effective viscosity and the density $\rho|_p(T)$.

For this project, the temperature of the working fluid is assumed to remain constant at 40°C because exact data of fluid properties is available in the literature [White (1991)] for this temperature.

This assumption renders the conservation law for energy superfluous for this project. Consequently, only equations (2-1) and (2-2) of the three conservation equations are used.

The preceding discussion hints at the possibility of keeping density, $\rho(p,T)$, and molecular viscosity, $\mu(p,T)$ constant. It is only necessary to establish whether $\rho(p,T)$ and $\mu(p,T)$ changes significantly with pressure.

2.5.2. Density

Assumption: $\rho = 992\text{kg/m}^3$

Motivation: It is generally accepted that a fluid, as opposed to a gas, is incompressible. Furthermore, at atmospheric pressure, the density at the test temperature of 40°C is 992 kg/m^3. Therefore, a uniform density of $\rho|_{T=40°C}$ = 992 kg/m^3 is assumed constant for this project.

2.5.3. Molecular viscosity

Assumption: $\mu = 0.653\text{mPa}\cdot\text{s}$

Motivation: Standard steam tables show that the viscosity of water at 40°C remains almost constant while the water pressure is allowed to vary in the vicinity of atmospheric pressure. Therefore, any deviations in the value of the molecular viscosity at standard atmospheric pressure caused by water pressures different from atmospheric pressure would be insignificant. The value of the molecular viscosity at atmospheric pressure and at a temperature of 40 is 0.653mPa·s. This value is then used for the molecular viscosity of the working fluid in the experimental torque converter.

2.5.4. Steady flow

Assumption: The flow is steady and the interaction effects between the pump and other elements are negligible.

Motivation: The turbine of the experimental torque converter was fixed while the velocity and pressure measurements were done. There were therefore no time dependent interactions between the stator and the two turbine blade rows straddling it. Von Backström en Lakshminarayana (1996) showed that the influence of the pump blade position on the second turbine outlet is minimal. Their observations were made on data obtained by laser anemometry at a specific point in time. There might, however, be a measurable time dependent influence on the inlet side of the first turbine blade row, which is the blade row closest to the pump outlet. The empirical data obtained by Venter (1993) and Steenkamp (1996) that is used in this project was obtained by instruments that would not have registered small, high frequency fluctuations superimposed on the average measurement in the flow field. Therefore, the empirical data used for validating purposes in this project are only measurements with the small high frequency fluctuations averaged out. The flow fields in the numerical models are therefore specified as steady.

2.5.5. Two-dimensional, axi-simmetric flow conditions

Assumption: It is assumed in some cases that the flow field is two-dimensional and axi-symmetric.

Motivation: In reality, the flow situation in a torque converter is so complex that a two-dimensional, axi-symmetric analysis will not be able to capture significant three-dimensional flow phenomena like secondary flow patterns, boundary layer separation and vortices. The flow channels in the vicinity of the first and second turbines as well as the stator are fortunately highly two-dimensional. Because of this the flow field at midspan of the second turbine blade row will hopefully be relatively two-dimensional. The flow fields obtained in this way will yield valuable engineering data like the pressure distribution on the surfaces of the stator and turbine blades at midspan. A two-dimensional approach saves large amount of time and requires much less computer resources in the form of speed and memory.

2.6. The inviscid, irrotational and incompressible flow model.

As discussed in section 2.5.1. the energy equation can be discarded because the fluid temperature is already known. Together with the energy equations the enthalpy *h* also disappears. Under the assumptions of incompressible Newtonian flow with constant transport properties the continuity and momentum equations respectively reduce to

$$\nabla \cdot \mathbf{V} = 0 \tag{2-5}$$

and

$$\rho \frac{D\mathbf{V}}{Dt} = \rho \mathbf{g} - \nabla p + \mu \nabla^2 \mathbf{V} \tag{2-6}$$

Irrotational flow is defined as a flow where the vorticity is zero throughout the flow field. This is mathematically expressed as follows:

$$\nabla \times \mathbf{V} = 0 \tag{2-7}$$

There also exists a vector identity which has a similar form than equation (2-7). Instead of a vector variable **V** it contains a scalar variable ϕ:

$$\nabla \times (\nabla \phi) = 0 \tag{2-8}$$

When equation (2-7) is compared to equation (2-8), it is clear from inspection that the velocity vector $\mathbf{V}$ in equation (2-7) can be replaced by $\nabla \phi$. Therefore, in the case of an irrotational flow field, equation (2-7) is valid and this allows the velocity vector to be replaced by a scalar function as follows:

$$\mathbf{V} = \nabla \phi \tag{2-9}$$

The scalar function ϕ in equation (2-9) is therefore defined for irrotational flow fields and is known as the velocity potential. Thus, a velocity potential has been defined that reduces the problem of finding the velocity field from a vector problem to a scalar one.

To derive the governing equation for an incompressible, inviscid and irrotational flow field in terms of the velocity potential which is defined by equation (2-9), the velocity potential is substituted into the continuity equation for incompressible fluids with constant transport properties, equation (2-5) to yield

$$\nabla \cdot (\nabla \phi) = 0$$

or

$$\nabla^2 \phi = 0 \tag{2-10}$$

For a two-dimensional flow field in a Cartesian coordinate system equation (2-10) becomes

$$\frac{\partial^2 \phi}{\partial x^2} + \frac{\partial^2 \phi}{\partial y^2} = 0 \tag{2-11}$$

Equation (2-10) is the well known Laplace equation.

Hence, the continuity equation for inviscid, irrotational and incompressible flow fields yields the Laplace equation. Because it is a linear partial differential equation the sum of any number of particular solutions of the Laplace equation is also a solution of that equation. For an irrotational, incompressible flow a complicated flow pattern can therefore be synthesised by adding together a number of elementary flows that are also irrotational and incompressible. This is the grand strategy of the panel method that is used in chapter 3 to analyse the flow through the stationary torque converter turbine.

The momentum equation for incompressible, inviscid flow with no body forces and constant transport properties, equation (2-6), can be rewritten in its three Cartesian coordinate components as follows:

$$\rho \mathbf{V} \cdot \nabla u + \frac{\partial p}{\partial x} = 0 \tag{2-12a}$$

$$\rho \mathbf{V} \cdot \nabla v + \frac{\partial p}{\partial y} = 0 \tag{2-12b}$$

$$\rho \mathbf{V} \cdot \nabla w + \frac{\partial p}{\partial z} = 0 \tag{2-12c}$$

Introducing the restriction of irrotational flow by means of the velocity potential into equation (2-12a) yields:

$$\rho \nabla \phi \cdot \nabla \frac{\partial \phi}{\partial x} + \frac{\partial p}{\partial x} = 0$$

$$\rho \nabla \phi \cdot \frac{\partial \nabla \phi}{\partial x} + \frac{\partial p}{\partial x} = 0$$

$$\frac{\rho}{2} \frac{\partial}{\partial x} \left(\nabla \phi \cdot \nabla \phi \right) + \frac{\partial p}{\partial x} = 0$$

$$\frac{\rho}{2}\frac{\partial}{\partial x}V^2+\frac{\partial p}{\partial x}=0$$

$$\frac{\partial}{\partial x}\left(\frac{\rho V^2}{2}+p\right)=0$$

This implies that $p+\frac{\rho V^2}{2}$ is independent of *x*. Similarly from equations (2-12b) and (2-12c) it can be shown that $p+\frac{\rho V^2}{2}$ is independent of *y* and *z* too. Thus, having established that $p+\frac{\rho V^2}{2}$ is constant in all directions of the flow field it is clear that $p+\frac{\rho V^2}{2}$ is constant throughout the flow field or

$$p+\tfrac{1}{2}\rho V^2=\text{const} \qquad (2\text{-}13)$$

This is the well-known Bernoulli equation. Hence, when the velocity field of an inviscid, incompressible and irrotational flow field has been determined from equations (2-11) and (2-9), the pressure field can be obtained from equation (2-13).

2.7. The viscous flow model

Although the complete governing equations for viscous flow, the Navier-Stokes equations, cannot be solved analytically for flow situations in general, they have been modeled by means of finite difference methods and finite elements. With finite difference methods the equations are discretised by means of Taylor series derivative truncations or by means of control-volume techniques. Flo++ for instance employs the latter technique. The numerical predictions are excellent for low Reynolds number flows that are still in the laminar flow regime. However, White (1991) reports that the number of grid points needed for accuracy increases drastically with increasing Reynolds numbers. At relatively low Reynolds numbers, in the region of 5000, the computational requirements exceed the available computing power of even the best computers. Direct numerical simulation of the Navier-Stokes equations is therefore limited to very low Reynolds number flows.

Apart from the fact that the calculation of the fine detail of viscous flow for general problems is impractical, engineers are not interested in the fine detail. The interest lies rather in the mean values of velocity, pressure or shear stress. The compromise solution therefore is to calculate the time-averaged variables of turbulent flow. Equations containing these variables are obtained by averaging procedures applied to the governing Navier-Stokes equations. The standard approach is to separate the fluctuating property of a variable from its time-mean value. The raw variables in the governing equations are substituted with their time-mean and fluctuating components. The time average of the resulting equations is then taken. The terms in the governing equations now contain the time-mean components of the original variables but due to the non-linearity of the governing equations new terms that contain the fluctuating components arise. These terms account for turbulent effects. They cannot be represented in terms of the mean flow variables however. The result is that the Reynolds averaged Navier-Stokes equations contain more variables than the number of available equations. The system of equations is therefore open. To obtain closure the fluctuating components must be me modelled in terms of the time-mean flow variables. The detailed equations used by the Flo++ programme that is utilised to apply this viscous flow model to the torque converter are given in chapter 4.

Chapter 3

INVISCID, IRROTATIONAL, INCOMPRESSIBLE FLOW FIELD MODELLING: THE SOURCE-VORTEX PANEL METHOD

3.1. Introduction

The equations for the inviscid, irrotational, incompressible flow model, i.e. potential flow, are much simpler to solve than the complete Navier-Stokes equations that also take viscosity and compressibility into account. Every potential flow solution is an exact solution of the Navier-Stokes equations [White (1991)]. This implies that if the influence of viscosity on the flow is insignificant, the simpler potential flow equations instead of the complete Navier-Stokes equations can be used to solve the flow problem. Due to the simplicity and potential accuracy of this flow model it is useful to explore its accuracy when applied to our torque converter.

The purpose of this chapter is to evaluate the applicability of the two-dimensional inviscid, irrotational, incompressible flow model on the fluid flow through the second turbine of our torque converter. The governing equations for this flow model are derived. This is followed by a discussion of the appropriate boundary conditions. From the governing equations and the boundary conditions the basic source-vortex panel method for a single body in a linear flow field is developed. This model is then extended to predict the flow field that surrounds multiple bodies in a radial freestream. This two-dimensional source-vortex panel method is then applied to the flow field through the stationary second turbine blade row together with the preceding stator blade row of the torque converter. Finally the results are evaluated.

3.2. Governing equations for inviscid, irrotational, incompressible flow

In chapter 2 the governing equations of the inviscid, irrotational, incompressible flow model are derived from the governing equations of the real flow model by means of two simplifying assumptions. These assumptions are that the flow is (1)

incompressible and (2) inviscid and irrotational. The continuity equation reduced to Laplace's equation, equation (2-10) under these assumptions. With the further restriction of two-dimensional flow, equation (2-10) further reduces to equation (2-11) for a Cartesian coordinate system:

$$\frac{\partial^2 \phi}{\partial x^2} + \frac{\partial^2 \phi}{\partial y^2} = 0 \tag{2-11}$$

The momentum equation reduced to Bernoulli's equation, equation (2-13):

$$p + \tfrac{1}{2}\rho V^2 = \text{const} \tag{2-13}$$

Laplace's equation is a second order linear differential equation. Because it is a linear differential equation, the sum of any number of particular solutions of equation (2-11) is also a solution of the equation. It is this characteristic that enables a complex inviscid, irrotational and incompressible flow field to be constructed from a number of elementary inviscid, irrotational, incompressible flow fields that individually satisfy equation (2-11). This is the core strategy of the panel method.

If the velocity field is constructed in such a way that the velocity at any particular point is the sum of the undisturbed freestream velocity and a disturbance velocity, then the freestream can be constructed from an elementary flow that satisfies equation (2-11). The freestream is the undisturbed flow field without any obstacles or solid surfaces. The disturbance velocity is the velocity caused by the obstacles or bodies in the freestream as a result of their wall boundary conditions. The total velocity is therefore calculated by adding the freestream velocity and the disturbance velocity. From equation (2-9) it follows that

$$\mathbf{V} = \mathbf{V}_\infty + \nabla \phi \tag{3-1}$$

where ϕ is the disturbance velocity potential and $\mathbf{V}_\infty$ is the freestream velocity. With the free stream specified, the disturbance velocity must be solved by means of equation (2-11) and the boundary conditions that pertain.

3.3. Boundary conditions

The boundary conditions are vital in the formulation of the flow model. Different two-dimensional, irrotational, incompressible flows are governed by the same equa-

tion, namely equation (2-11) but are differentiated by their particular boundary conditions. Each particular arrangement of boundary conditions has a unique solution under equation (2-11). The blades studied in this thesis are modelled as bodies that are totally immersed in a flow field. Two types of boundaries bound this flow field namely (1) the boundary at an infinite distance away from the body where freestream flow occurs and (2) the surface of the body itself.

3.3.1. Infinity boundary conditions

For only freestream flow conditions to occur at an infinite distance away from the body, the influence of the solid surfaces in the flow field must vanish. These influences are the velocity changes caused by the solid surfaces in the flow field. The variable used in the analysis of inviscid, irrotational, incompressible flow fields, is the disturbance velocity potential. The infinity boundary condition can therefore be modelled as:

$$\nabla\phi \to 0 \text{ at infinity} \tag{3-2}$$

where ϕ is the disturbance velocity potential caused by the body or solid surfaces in the flow field model.

3.3.2. Wall boundary conditions

As explained by White (1991) potential flows cannot satisfy the no-slip condition at a solid wall. The no-slip condition at a wall requires both the normal and tangential velocity components to vanish. Because flow cannot penetrate a solid surface, the velocity component normal to a surface must be zero. This leaves the velocity component tangential to the surface to be considered. Euler's equations of motion that govern inviscid flow has only first order velocity derivatives which means that only one velocity condition can be satisfied at a solid wall. In order to enforce the non-through flow property of a solid wall, this must be the condition that states that the velocity component normal to a solid wall is zero. No restraints can therefore be placed on the velocity component tangential to a solid surface. This means that the tangential velocity component at a solid wall must be allowed to take on finite, non-zero values. This is also a realistic physical consequence of the inviscid flow model.

Due to the assumption of an inviscid fluid, it slips without friction tangentially to the wall resulting in a finite tangential velocity component. Therefore the wall boundary condition can be written as $V_n(fluid) = V_n(wall)$. If the wall is stationary this equation reduces to

$$\mathbf{V} \cdot \mathbf{n} = 0 \text{ on } S(x, y, t) \tag{3-3}$$

where $S(x, y, t)$ is the surface of the bodies in the freestream and $\mathbf{n}$ is the unit outward normal vector on the surface. To obtain the wall boundary condition in terms of the disturbance potential equation (3-1) is substituted into equation (3-3) to yield:

$$\nabla\phi \cdot \mathbf{n} = -\mathbf{V}_\infty \cdot \mathbf{n} \text{ on } S(x, y, t) \tag{3-4}$$

3.4. Solution method

Having established the governing equations and boundary conditions for the inviscid, irrotational, incompressible flow model, the formulation of the model is completed. The general method to solve this flow model entails the following steps:

- Solve Laplace's equation for the disturbance potential ϕ together with the boundary conditions.
- Obtain the flow velocity from equation (3-1).
- Obtain the pressure distribution from Bernoulli's equation $p + \frac{1}{2}\rho V^2 = \text{const}$.

Bernoulli's equation can only be used throughout the flow field if it can be assumed to be steady, frictionless and incompressible without an unacceptable loss of accuracy. Because these are the assumptions of the flow model utilised in this chapter, the Bernoulli equation can be applied to the results that are obtained here. The assumption of steady flow furthermore allows the time variable in equations (3-3) and (3-4) to be dropped.

For a specific experiment it is far more useful to scale the predicted pressure distribution in terms of the pressure coefficient C_p than to present it in its original form. The pressure coefficient is a standard dimensionless parameter and is defined as:

$$C_p \equiv \frac{p - p_\infty}{\frac{1}{2}\rho_\infty V_\infty^2} \tag{3-5}$$

where ρ_∞ and V_∞ are the density and velocity respectively at an appropriate reference point. This definition permits an easy way to calculate the pressure coefficient in an irrotational, steady and incompressible flow field where Bernoulli's equation is applicable. Because Bernoulli's equation can be applied to the flow model utilised in this chapter, it is applied to equation (3-5) to yield:

$$C_p \equiv \frac{p - p_\infty}{\frac{1}{2}\rho_\infty V_\infty^2} = 1 - \left(\frac{V}{V_\infty}\right)^2 \tag{3-6}$$

Equation (3-6) is then used to calculate the pressure coefficient for this flow model.

3.5. Solving the disturbance potential

3.5.1. Background

The panel method popularised by Hess and Smith (1967) is a practical direct numerical method to obtain the disturbance potential ϕ with which to calculate a flow field's velocity and pressure distributions. Various panel method schemes were subsequently developed. See for instance Moran (1984). According to Moran (1984) the source-based Smith-Hess method and the doublet-based linear potential method are usually more accurate than most of the other methods for a four-digit NACA airfoil of reasonable thickness for a given number of panels. The Smith-Hess method however cannot handle very thin airfoils well. When the thickness approaches zero the source strength may vanish. If the Kutta condition is then applied, the circulation also vanishes. The Smith-Hess method is nevertheless a very accurate method that is also applicable to multi-element flow situations. It was also found that higher order methods give very little increase in accuracy for exterior flows about convex bodies [Hess, 1973]. It was therefore decided to use the widely publicised first order source-based Smith-Hess method and adapt it to handle multiple bodies in a radial inflow freestream.

The disadvantage of panel methods is that they break down when the local Mach number approaches unity because a linearised approximation to the full potential equation is solved. This is remedied by using so called field methods as described

by Sinclair (1986). The Mach number for flow field in this project is nowhere near unity, therefore field methods are not further discussed.

The source-based Smith-Hess method entails the following steps:

- Place a continuously varying source distribution and a continuous vorticity distribution of constant strength on the surface of a two-dimensional body in the freestream. This yields an integral equation for the calculation of the disturbance potential at an arbitrary point in the flow field.
- Discretise the integral equation obtained in the previous step by approximating the arbitrary surface with a sufficient number of discrete surface panels that are small compared to the rest of the body. Place a constant strength source distribution that is allowed to differ between panels on each panel. In addition to the source distribution place a constant strength vortex distribution on each panel that has the same strength for all panels.
- Apply the discretised potential equation to the tangency boundary condition and the Kutta condition to obtain a set of linear equations with which the unknown source strengths on each panel and the total vortex strength for the body can be solved. The tangency boundary condition is applied at a control point on each panel in turn and the Kutta condition to the control points of the two adjacent panels where the flow must leave the body.
- With the source and vortex strengths known, the desired velocities and pressure coefficients can be obtained at each panel's control point from equations (3-1) and (3-6).

3.5.2. Discretising the governing equations

The disturbance velocity potential at a distance r from a point source in the (x, y)-plane is given by

$$\phi = \frac{\Lambda}{2\pi} \ln r \tag{3-7}$$

where Λ is defined as the source strength. The point source is one of the elementary flows that satisfy equation (2-11), the governing equation for inviscid, irrotational, incompressible flow. Figure 3-1 illustrates source flow induced by a point source.

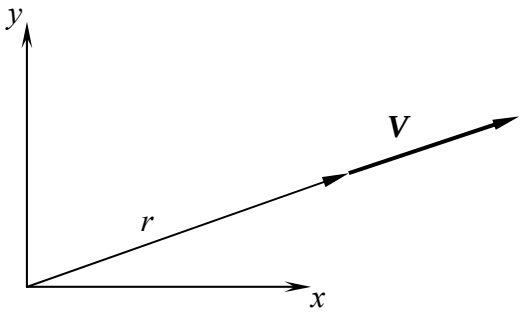

Figure 3-1. Source flow

To calculate the disturbance potential caused by a solid body, an infinite number of infinitesimally small point sources are placed side by side in a continuous line on the surface of the body in the freestream. The strength of each point source is infinitesimally small. If we define $\sigma = \sigma(s)$ as the source strength per unit length in the s direction, i.e. along the surface of the body, then the strength of an infinitesimally small line of sources ds is $\sigma\, ds$. This is an infinitesimally small source, which induces an infinitesimally small velocity potential given by

$$d\phi = \frac{\sigma\, ds}{2\pi} \ln r \tag{3-8}$$

From equation (3-8) it follows that for a source located at a point (ξ, η) on the surface of a body the velocity potential at an arbitrary point (x, y) somewhere in the flow field is given by

$$d\phi = \frac{\sigma(\xi,\eta) ds}{4\pi} \ln\left[(x-\xi)^2 + (y-\eta)^2\right] \tag{3-9}$$

The disturbance velocity potential of the continuous source distribution on the complete surface S of the body is therefore given by

$$\phi(x,y) = \oint_S \frac{\sigma(\xi,\eta)}{4\pi} \ln\left[(x-\xi)^2 + (y-\eta)^2\right] ds \tag{3-10}$$

With only a continuous source distribution on the surface of the body, the resulting flow pattern around the body will only be non-lifting flow due to the absence of circulation in the flow field surrounding the body. From the Kutta-Joukowski theorem it is clear that the presence of circulation is essential for finite lift on a body:

$$L' = \rho_\infty V_\infty \Gamma \tag{3-11}$$

where L' is lift per unit span of the body in the freestream and Γ is the circulation around any closed curve enclosing the body. Hence, to calculate lifting flow about a

body in a freestream, a finite circulation in the flow surrounding the body must be induced. In order to accomplish this, a continuous vortex distribution is placed on the surface S of the body in addition to the source distribution. Because the continuously varying source distribution already takes care of the thickness distribution of the body surface, a constant strength vortex distribution will suffice to take care of the required circulation as dictated by the Kutta condition (to be described shortly).

The vortex distribution is constructed in the same fashion as the source distribution. The two-dimensional vortex point singularity that induces vortex flow is another elementary flow that satisfies the governing equation for irrotational, incompressible flow. The velocity potential induced by a two-dimensional vortex point singularity is given by

$$\phi = -\frac{\Gamma}{2\pi}\theta \tag{3-12}$$

where θ is the angle between the x-axis and the position vector of the point where the velocity potential is calculated. Γ is the circulation around a closed curve surrounding the vortex point singularity also called the strength of the vortex flow. A vortex flow field induced by a point vortex is depicted in figure 3-2.

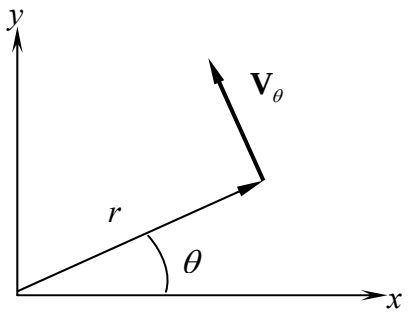

Figure 3-2. Vortex flow.

Equation (3-12) satisfies the governing equation for irrotational, incompressible flow, equation (2-11), as well as the infinity boundary condition, equation (3-2). Due to the linear nature of equations (2-11) and (3-2) the potential due to any sum or continuous distribution of infinitesimal vortex points will then also satisfy these two equations. We therefore proceed to place a continuous distribution of infinitesimally small vortex points on the surface of the two-dimensional body. Let

$\gamma = \gamma(s)$ be the vortex strength per unit length along the two-dimensional surface of the body. Then the velocity potential caused by an infinitesimal section ds in the x-y-plane is given by

$$d\phi = -\frac{\gamma\, ds}{2\pi}\theta \tag{3-13}$$

For a vortex located at a point (ξ, η) on the surface of a body the velocity potential at an arbitrary point (x, y) somewhere in the flow field is given by

$$d\phi = -\frac{\gamma(\xi,\eta)ds}{2\pi}\arctan[(y-\eta)/(x-\xi)] \tag{3-14}$$

The potential of the vortex distribution on the complete surface S of the body is therefore given by

$$\phi(x,y) = -\oint_S \frac{\gamma(\xi,\eta)}{2\pi}\arctan[(y-\eta)/(x-\xi)]ds \tag{3-15}$$

that satisfies equations (2-11) and (3-2).

Due to the linear nature of the governing equations (2-11) and (3-2) the disturbance velocity potentials caused by the source and vortex distributions as calculated by means of equations (3-10) and (3-15) respectively can be added to yield a velocity potential that is the result of both source flow and vortex flow distributions. The resulting disturbance velocity potential is then calculated by:

$$\phi(x,y) = \oint_S \frac{\sigma(\xi,\eta)}{4\pi}\ln\left[(x-\xi)^2 + (y-\eta)^2\right]ds \tag{3-16}$$
$$-\oint_S \frac{\gamma(\xi,\eta)}{2\pi}\arctan[(y-\eta)/(x-\xi)]ds$$

Because no general method to solve equation (3-16) analytically for an arbitrary body exists it must be discretised and solved numerically. To accomplish this, the surface of the body in the freestream is approximated by a series of straight panels. Then the source strength $\sigma(s)$ per unit length is taken to be constant over a panel but allowed to vary between the panels. Each panel will now assume its own constant source strength σ_i. The vortex distribution is discretised in a similar fashion. Only the total circulation Γ around the body is needed to provide lift in such a way that the Kutta condition is satisfied. The purpose of this technique is to solve the

unknown source strengths σ_i and the unknown circulation Γ in such a way that the body surface becomes a streamline of the flow and the Kutta condition is satisfied. The body surface becomes a streamline of the flow because the solid surface boundary condition is the same as the definition for a streamline: the flow velocity component perpendicular to the surface vanishes. This is the remaining boundary condition that needs to be satisfied because the infinity boundary condition and the governing equation for inviscid, irrotational, incompressible flow are already satisfied by equation (3-16).

A control point must be defined on each panel where the boundary and Kutta conditions are to be applied. The slope of the body contour at the point opposite the panel's midpoint will be the same as the slope of the panel if the contour subtending the panel is a section of a circle. If the panels are chosen carefully to ensure that the contours subtending them approximate a section of a circle, the point where the slope of the contour best approximates the slope of the corresponding panel will be the point opposite the midpoint of the panel. Because the slope of the contour at a particular point defines the direction of zero normal velocity to the solid surface of the body, the control point where the surface boundary and Kutta conditions are applied is taken as the midpoint of the panel. The surface boundary condition stating that the normal component of the flow velocity is zero on the surface is applied at each control point. Furthermore, the Kutta condition is applied at the control points of the two adjoining panels where the flow leaves the body.

From the definition of vortex strength (Anderson, 1991) the total circulation is the integral of the distribution of vortex strengths on the airfoil:

$$\Gamma = \oint_S \gamma(\xi,\eta)ds \tag{3-17}$$

We can take the vorticity distribution to be constant over each element because there are no constraints that prevent us from doing this. The only constraint is that the Kutta condition must be satisfied. This constraint requires the distribution of vortex strengths to add up to the unique circulation around the body that will cause the Kutta condition to be satisfied. The source strengths that are calculated simultaneously with the vortex distribution will adapt to satisfy the prescribed boundary

conditions. For the case of a constant vorticity distribution on the surface of the body in the freestream, it follows from equation (3-17) that

$$\gamma = \Gamma / S \tag{3-18}$$

where S is the total length of the surface of the body. Substituting equation (3-18) into equation (3-16) and applying the result to the ith panel on the panelled body, the velocity potential induced at an arbitrary point *(x,y)* in the flow by the ith panel is:

$$\phi_i(x,y) = \frac{\sigma_i}{4\pi}\int_{S_i} \ln\left[(x-\xi)^2 + (y-\eta)^2\right] ds \tag{3-19}$$
$$-\frac{\Gamma}{2\pi S}\int_{S_i} \arctan\left[(y-\eta)/(x-\xi)\right] ds$$

While the integral is taken over the ith panel only, the source strength per unit length σ_i could be taken out of the integral because it is constant over the panel. The velocity potential induced at an arbitrary point *(x,y)* in the flow by the complete body is obtained by summing the velocity potentials induced by each panel as calculated in equation (3-19):

$$\phi(x,y) = \sum_{i=1}^{N} \phi_i(x,y) \tag{3-20}$$
$$= \sum_{i=1}^{N} \frac{\sigma_i}{4\pi}\int_{S_i} \ln\left[(x-\xi)^2 + (y-\eta)^2\right] ds$$
$$-\frac{\Gamma}{2\pi S}\sum_{i=1}^{N}\int_{S_i} \arctan\left[(y-\eta)/(x-\xi)\right] ds$$

where N is the number of panels on the body as shown in figure 3-3.

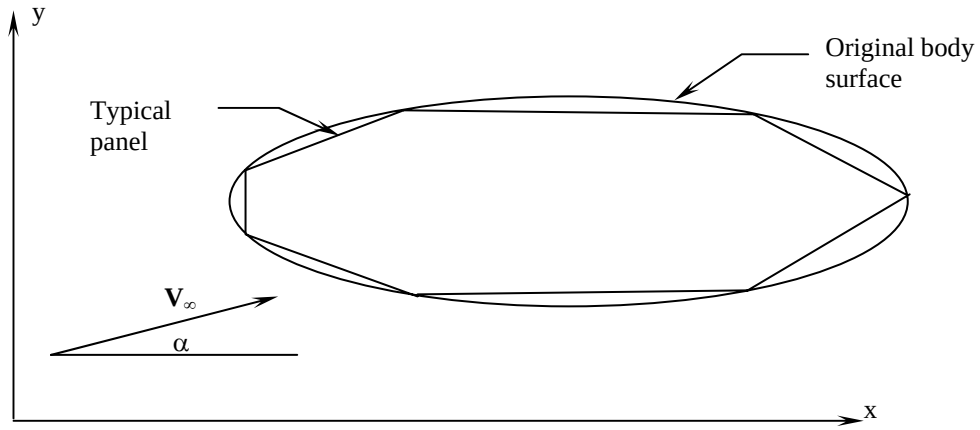

Figure 3-3. Panelling of a typical body.

The integrals in equation (3-20) can be construed as influence coefficients allowing equation (3-20) to be rearranged as follows:

$$\phi(x,y) = \sum_{i=1}^{N} \frac{\sigma_i}{4\pi} C_i(x,y) - \frac{\Gamma}{2\pi S} \sum_{i=1}^{N} G_i(x,y) \tag{3-21}$$

where $C_i(x,y)$ and $G_i(x,y)$ represents the integrals in equation (3-21).

To solve for the N unknown σ_i as well as the unknown Γ the solid wall boundary condition is applied at each panel's control point. This approach yields a system of N linear algebraic equations. The system is still singular because there are N+1 unknown quantities due to the presence of the unknown Γ in the equations. In order to make the system non-singular, a further equation is needed. This equation is obtained by applying the Kutta condition at the control points of the two adjacent panels across which the flow leaves the body. We must therefore still ensure that the problem satisfies the Kutta condition and the solid wall boundary conditions as pointed out earlier.

3.5.3. The wall condition

The solid wall boundary condition is satisfied by substituting equation (3-21) into equation (3-4) which states that the velocity component perpendicular to a solid surface is zero. This boundary condition is applied at the control point of panel j:

$$\sum_{i=1}^{N} \frac{\sigma_i}{4\pi} \left[n_{xj} C_{xi}(x_j, y_j) + n_{yj} C_{yi}(x_j, y_j) \right] \tag{3-22}$$
$$- \frac{\Gamma}{2\pi S} \sum_{i=1}^{N} \left[n_{xj} G_{xi}(x_j, y_j) + n_{yj} G_{yi}(x_j, y_j) \right] = -\mathbf{V}_{\infty j} \cdot \mathbf{n}_j$$

where $C_{xi}(x_j, y_j)$ and $C_{yi}(x_j, y_j)$ are the components of $\nabla C(x_j, y_j)$;

$G_{xi}(x_j, y_j)$ and $G_{yi}(x_j, y_j)$ are the components of $\nabla G(x_j, y_j)$;

$\mathbf{V}_{\infty j}$ is the freestream velocity at the control point of panel j;

$\mathbf{n}_j$ is the unit outward normal vector on panel j with components $n_{xj} = -\sin\theta_j$ and $n_{yj} = \cos\theta_j$ in the x- and y-directions respectively as depicted in figure 3-4.

As shown in figure (3-4) the angle θ_j is the angle between the panel bottom (the side on the inside of the body) and the global x-axis of the global xy-coordinate system. Its value is obtained from

$$\theta_j = \arctan\left(\frac{y_{jbegin} - y_{jend}}{x_{jbegin} - x_{jend}}\right) \tag{3-23}$$

To correctly evaluate $\sin\theta_j$ and $\cos\theta_j$ in subsequent equations, the angle θ_j must be evaluated in the range $(-\pi, \pi)$ by taking proper account of the quadrant in which the angle is evaluated. Considering the individual signs of the numerator and denominator of equation (3-23) accomplishes this.

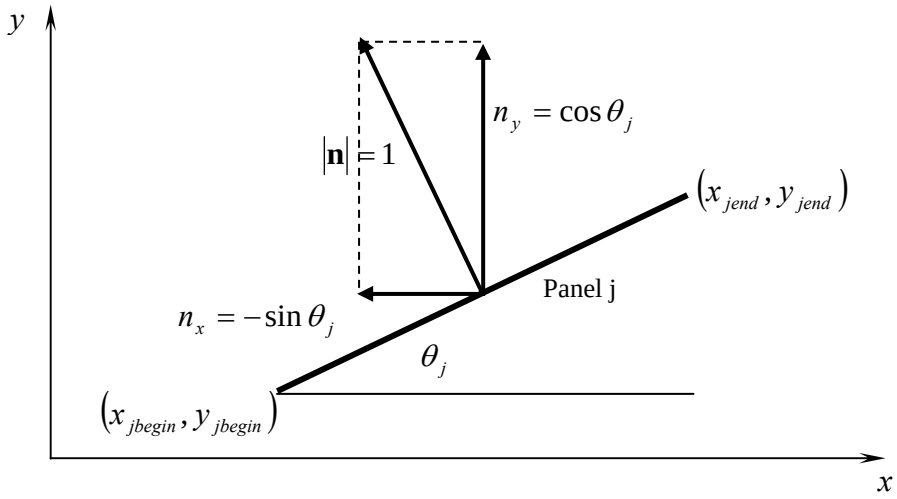

Figure 3-4. Typical panel with unit outward normal vector.

By applying the solid boundary condition as calculated by equation (3-22) to each panel at its control point, a set of N linear algebraic equations with N+1 unknown dependent variables is created:

$$\sum_{i=1}^{N} \frac{\sigma_i}{4\pi}\left[n_{xj} C_{xi}(x_j, y_j) + n_{yj} C_{yi}(x_j, y_j)\right] - \frac{\Gamma}{2\pi S}\sum_{i=1}^{N}\left[n_{xj} G_{xi}(x_j, y_j) + n_{yj} G_{yi}(x_j, y_j)\right] = -\mathbf{V}_{\infty j} \cdot \mathbf{n}_j \quad \text{for } j = 1,2,\ldots,N \tag{3-24}$$

The remaining equation required to ensure that the system is determinant, is obtained by applying the Kutta condition to the two adjacent panels *m* and *n* across which the flow leaves the body.

3.5.4. The Kutta condition

The assumption of inviscid flow may cause large deviations between the real flow field and the one predicted by inviscid flow theory. These deviations are often most notable in the flow patterns around the solid boundary walls and the difference in the predicted net forces on them. Finite net forces on a body in a freestream are the consequence of the viscosity of the freestream fluid. For high Reynolds number flows like the flows studied here the effects of viscosity are limited to a very thin boundary layer on the wall of the body. The behaviour of that boundary layer though can cause a totally different pressure distribution on the body surface from the pressure distribution predicted by purely inviscid flow theory. In normal viscous flow the boundary layer, while attached, causes the flow to smoothly leave an airfoil at its trailing edge. This causes the freestream surrounding this body to alter its pressure distribution on the surface resulting in a finite force perpendicular to the freestream on the body. Other viscous effects like skin friction will cause a force in the direction of the average freestream flow. Viscous effects may also cause the boundary layer to separate from the surface of the body causing another alteration in the lift and drag forces exerted on the body surface. These effects are not computable by means of inviscid flow theory alone and are outside the scope of this study. We are only interested in the well-behaved flow field observed in our torque converter. To analyse non-separated flow conditions at high Reynolds numbers economically, boundary layer predictions can be patched onto inviscid flow field analysis as described for instance by White (1991) and Hirsch (1988). Purely two-dimensional, subsonic, inviscid flow theory however predicts that the components of the pressure distribution in the average direction of the freestream flow will exactly cancel causing zero drag. This phenomenon is the so-called D'Alembert paradox. The same is true for the pressure components perpendicular to the average freestream direction.

Fortunately the lift on a body can be calculated by means of potential flow theory with the aid of an artificial condition to simulate certain effects of real flows around slender bodies with sharp trailing edges. This technique does not work for bluff bodies though. The existence of a functional relationship between the lift force

caused by the pressure distribution on a body in a freestream and the circulation in the freestream surrounding it enables this calculation. This relationship is expressed by the Kutta-Joukowski law, equation (3-11), which applies to all 2-D potential flows. The wall boundary condition that the freestream forms a streamline to simulate the boundary of the body in all cases causes the flow to be calculated in such a way that no net forces exist on the body. This flow pattern will cause the rear stagnation point to depart from the position it would have had in a physically realistic flow field except for some non-lifting flow situations. In the case of lifting flows the required circulation in the freestream surrounding such a body can be induced by a vortex singularity or a combination of vortex singularities in or on that body. As was pointed out earlier vortex flow is a valid elementary potential flow.

In cases where no flow separation exists, i.e. well behaved flow, the vortex strength distribution on the body surface that causes that unique amount of circulation in the flow field around the body that occurs when the flow smoothly leaves the body at the trailing edge has to be specified or calculated. For our application we specify the flow velocity at the two adjacent panels forming the sharp trailing edge of the body where the flow smoothly leaves it. This specification fixes the circulation around the aerofoil and, because the circulation is determined by the total vortex strength, also the total vortex strength on the panels of the aerofoil. This method is only applicable to slender bodies with sharp trailing edges in a freestream since in viscous flow with no boundary layer separation, the point where the flow leaves the body coincides with the sharp trailing edge. This is the essence of the Kutta condition. A more precise description of the Kutta condition is given by Moran (1984).

The trailing edge of a slender body in a freestream can have either a finite included angle or it can be cusped. Let us denote the velocities at the top and bottom edges of the trailing edge as V_t and V_b respectively. For a finite included angle at the trailing edge, V_t is parallel to the top surface at the trailing edge. Similarly V_b is parallel to the bottom edge at the trailing edge. If these velocities were finite at the trailing edge, then there would have been two different velocities at the same point. This is physically impossible. The only remaining possibility is that $V_t = V_b = 0$ for a finite angle trailing edge. For a cusped trailing edge though, V_t and V_b have the same di-

rection at the trailing edge and hence both V_t and V_b can be finite. The pressure at the trailing edge though is unique. Applying Bernoulli's equation at the top and bottom surfaces at the trailing edge yields

$$p + \tfrac{1}{2}\rho V_t^2 = p + \tfrac{1}{2}\rho V_b^2 \tag{3-25}$$

where p is the pressure at the trailing edge. From equation (3-25) it follows that $V_t = V_b$. Hence, for cusped and finite angle trailing edges, the velocities at the top and bottom edges next to the trailing edge are equal. Denoting the control point at the top panel as *m* and the control point at the bottom panel as *n*, the Kutta condition can be expressed mathematically as follows:

$$\begin{aligned} &\mathbf{V}_m \cdot \mathbf{t}_m = -\mathbf{V}_n \cdot \mathbf{t}_n \text{ or} \\ &[\mathbf{V}_{\infty m} + \nabla\phi(x_m, y_m)]\cdot \mathbf{t}_m = [\mathbf{V}_{\infty n} + \nabla\phi(x_n, y_n)]\cdot \mathbf{t}_n \end{aligned} \tag{3-26}$$

Here $\mathbf{t}_m$ and $\mathbf{t}_n$ are the unit tangential vectors on the top and bottom panels respectively. The tangential unit vector is depicted in figure 3-5. The numerical approximation for the Kutta condition is obtained by substituting equation (3-21) into equation (3-26):

$$\begin{aligned} &\sum_{i=1}^{N} \frac{\sigma_i}{4\pi}\begin{bmatrix} t_{xm}C_{xi}(x_m, y_m) + t_{ym}C_{yi}(x_m, y_m) \\ + t_{xn}C_{xi}(x_n, y_n) + t_{yn}C_{yi}(x_n, y_n) \end{bmatrix} \\ &-\frac{\Gamma}{2\pi S}\sum_{i=1}^{N}\begin{bmatrix} t_{xm}G_{xi}(x_m, y_m) + t_{ym}G_{yi}(x_m, y_m) \\ + t_{xn}G_{xi}(x_n, y_n) + t_{yn}G_{yi}(x_n, y_n) \end{bmatrix} \\ &= -\mathbf{V}_{\infty m}\cdot\mathbf{t}_m - \mathbf{V}_{\infty n}\cdot\mathbf{t}_n \end{aligned} \tag{3-27}$$

If the two adjacent trailing edge panels on which the Kutta condition is numerically applied are large and the airfoil has a highly loaded trailing edge, the pressures at their control points may differ significantly from each other. Care must therefore be taken to specify the two trailing edge panels in such a way that the difference in the pressure between these two control points is kept within acceptable limits. Specifying smaller trailing edge panels can accomplish this. Equation (3-27) together with equation (3-24) yield the required non-singular set of N+1 linear algebraic equations with which the N source strengths σ_i as well as the total circulation Γ can be solved.

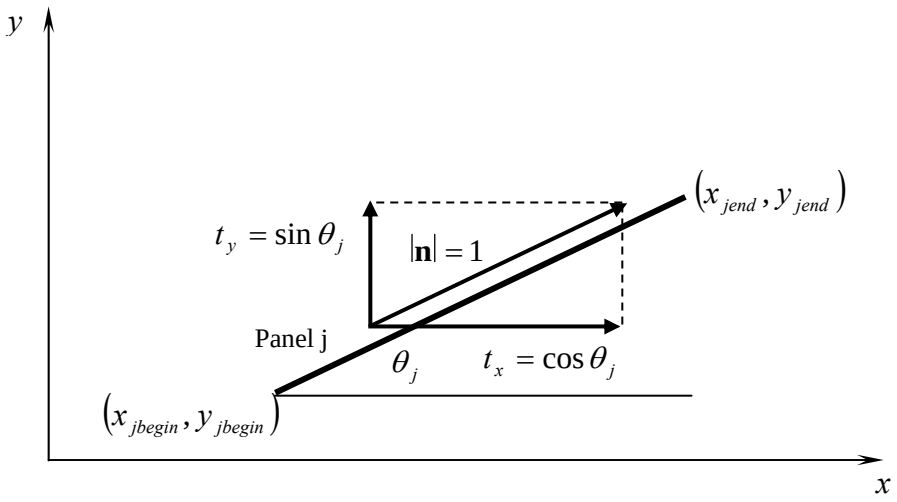

Figure 3-5. Typical panel with unit tangential vector.

3.5.5. The influence coefficients and velocity calculations

To obtain the numerical values of the quotients of the sources σ_i and the total circulation Γ, the influence coefficients must be solved. The influence coefficients due to the source distribution are

$$C_i(x,y) = \int_{S_i} \ln\left[(x-\xi)^2 + (y-\eta)^2\right] ds \tag{3-28}$$

$$C_{xi}(x,y) = \frac{\partial C_i}{\partial x} = 2\int_{S_i} \frac{x-\xi}{(x-\xi)^2 + (y-\eta)^2} ds \tag{3-29}$$

$$C_{yi}(x,y) = \frac{\partial C_i}{\partial y} = 2\int_{S_i} \frac{y-\eta}{(x-\xi)^2 + (y-\eta)^2} ds \tag{3-30}$$

In order to simplify the integration along *ds*, the integration is done in a coordinate system based on the element. The x-axis of the local coordinate system is aligned with the panel while the y-axis is aligned with the outward unit normal vector of the panel. The origin of the local coordinate system is placed on the control point of the panel. The local coordinate system is depicted in figure 3-6.

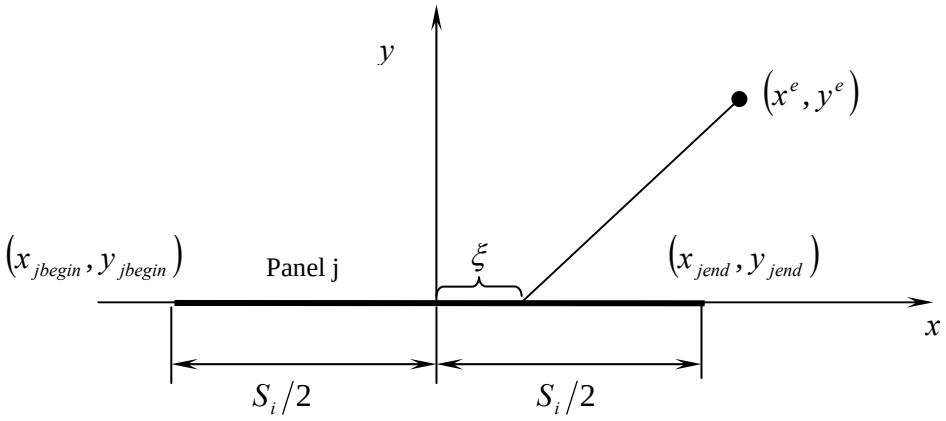

Figure 3-6. Integration over a line segment with local coordinate system.

With this technique integration is done with respect to one coordinate only instead of both coordinates, as is the case when the integration is done in terms of the global coordinate system. The relationship between the global coordinates (x, y) and the local coordinates (x^e, y^e) is given by the coordinate transformation

$$\begin{aligned} x^e &= (x - x_c)\cos\theta + (y - y_c)\sin\theta \\ y^e &= (y - y_c)\cos\theta - (x - x_c)\sin\theta \end{aligned} \tag{3-31}$$

where (x_c, y_c) are the coordinates of the origin of the local coordinate system that coincides with the control point of the panel and θ is the angle of the panel with respect to the global coordinate system as given by equation (3-23). The influence coefficients at the point (x^e, y^e) are now integrated on the x-axis only with ξ the running variable:

$$\begin{aligned} C^e_{xi}(x^e, y^e) &= 2\int_{-S_i/2}^{S_i/2} \frac{x^e - \xi}{(x^e - \xi)^2 + y^{e2}} d\xi \\ &= \ln\left[\frac{(x^e + S_i/2)^2 + y^{e2}}{(x^e - S_i/2)^2 + y^{e2}}\right] \end{aligned} \tag{3-32}$$

$$C_{yi}^{e}\left(x^{e},y^{e}\right)=2\int_{-S_i/2}^{S_i/2}\frac{y^{e}}{\left(x^{e}-\xi\right)^{2}+y^{e2}}d\xi \tag{3-33}$$
$$=2\left[\arctan\left[\frac{x^{e}+S_i/2}{y^{e}}\right]-\arctan\left[\frac{x^{e}-S_i/2}{y^{e}}\right]\right]$$
$$=2\arctan\left[\frac{y^{e}S_i}{x^{e2}+y^{e2}-\left(S_i/2\right)^{2}}\right]$$

The inverse tangent of equation (3-33) must also be evaluated in the range $\left(-\pi,\pi\right)$ by taking proper account of the quadrant in which the angle is evaluated. The individual signs of the numerator and denominator of equation (3-33) indicate the quadrant in which the angle is evaluated. It follows from equations (3-32) and (3-33) that the value of $C_{xi}^{e}=0$ and the value of $C_{yi}^{e}=2\pi$ at the control point of a panel.

When considering that the disturbance velocity caused only by the source distribution on the ith panel at $\left(x,y\right)$ as given by

$$\mathbf{V}_{dist}\left(x,y\right)=\nabla\phi\left(x,y\right)=\mathbf{i}\sum_{i=1}^{N}\frac{\sigma_i}{4\pi}C_{xi}\left(x,y\right)+\mathbf{j}\sum_{i=1}^{N}\frac{\sigma_i}{4\pi}C_{yi}\left(x,y\right) \tag{3-34}$$

it is clear that C_{xi} and C_{yi} are actually velocity components in terms of the global coordinate system while C_{xi}^{e} and C_{yi}^{e} are the velocity components written in terms of each element's own local coordinate system as defined by figure 3-6. The values of C_{xi} and C_{yi} can therefore be computed by transforming the values of C_{xi}^{e} and C_{yi}^{e} back to the global coordinate system:

$$\begin{aligned}C_{xi}\left(x,y\right)&=C_{xi}^{e}\left(x^{e},y^{e}\right)\cos\theta-C_{yi}^{e}\left(x^{e},y^{e}\right)\sin\theta\\C_{yi}\left(x,y\right)&=C_{yi}^{e}\left(x^{e},y^{e}\right)\cos\theta+C_{xi}^{e}\left(x^{e},y^{e}\right)\sin\theta\end{aligned} \tag{3-35}$$

The remaining influence coefficients are those due to the vortex distribution:

$$G_i\left(x,y\right)=\int_{S_i}\arctan\left[\left(y-\eta\right)/\left(x-\xi\right)\right]ds \tag{3-36}$$

$$G_{xi}\left(x,y\right)=\frac{\partial G_i}{\partial x}=-\int_{S_i}\frac{y-\eta}{\left(x-\xi\right)^{2}+\left(y-\eta\right)^{2}}ds \tag{3-37}$$

$$G_{yi}(x,y)=\frac{\partial G_i}{\partial y}=\int_{S_i}\frac{x-\xi}{(x-\xi)^2+(y-\eta)^2}\,ds \tag{3-38}$$

A comparison between equation (3-37) and equation (3-30) as well as between equation (3-38) and equation (3-29) shows that

$$G_{xi}(x.y)=-\frac{C_{yi}(x,y)}{2} \tag{3-39}$$

$$G_{yi}(x,y)=\frac{C_{xi}(x,y)}{2} \tag{3-40}$$

This concludes the first of the three steps in the panel method outlined in section 3.4. The second step is to solve the velocities on the surface of the body by means of equation (3-1). Remember that the wall boundary condition requires that the velocity be tangent to the surface of the body. The control point of a panel of the body is the position where the numerical model is required to satisfy the no-penetration condition at a solid wall. Hence the control point of a panel must also be the place where the velocity on that part of the body surface that is represented by the panel is calculated by the numerical model. From equation (3-1) it follows that the surface velocity at panel *j* is given by

$$\mathbf{V}(x_j,y_j)=\mathbf{V}_{\infty j}+\nabla\phi(x_j,y_j) \tag{3-41}$$

Writing equation (3-41) in terms of its vector components and substituting equation (3-21) into equation (3-41) yields

$$\begin{aligned}&\mathbf{i}V_x(x_j,y_j)+\mathbf{j}V_y(x_j,y_j)\\&=\mathbf{i}V_{\infty x}(x_j,y_j)+\mathbf{j}V_{\infty y}(x_j,y_j)\\&+\mathbf{i}\left[\sum_{i=1}^{N}\frac{\sigma_i}{4\pi}C_{xi}(x_j,y_j)-\frac{\Gamma}{2\pi S}\sum_{i=1}^{N}G_{xi}(x_j,y_j)\right]\\&+\mathbf{j}\left[\sum_{i=1}^{N}\frac{\sigma_i}{4\pi}C_{yi}(x_j,y_j)-\frac{\Gamma}{2\pi S}\sum_{i=1}^{N}G_{yi}(x_j,y_j)\right]\end{aligned} \tag{3-42}$$

From equation (3-42) it can be seen from inspection that

$$V_x(x_j,y_j)=V_{\infty x}(x_j,y_j)+\sum_{i=1}^{N}\frac{\sigma_i}{4\pi}C_{xi}(x_j,y_j)-\frac{\Gamma}{2\pi S}\sum_{i=1}^{N}G_{xi}(x_j,y_j) \tag{3-43}$$

$$V_y(x_j,y_j)=V_{\infty y}(x_j,y_j)+\sum_{i=1}^{N}\frac{\sigma_i}{4\pi}C_{yi}(x_j,y_j)-\frac{\Gamma}{2\pi S}\sum_{i=1}^{N}G_{yi}(x_j,y_j) \tag{3-44}$$

Equations (3-41) and (3-42) therefore give the velocity on the surface of the body.

The third step in the panel method outlined in section 3.4 is to solve the pressure distribution on the surface of the body by means of Bernoulli's equation:

$$C_p\left(x_j, y_j\right) = 1 - \frac{V_x^2\left(x_j, y_j\right) + V_y^2\left(x_j, y_j\right)}{V_\infty^2} \tag{3-45}$$

This method for a single body in a freestream must now be extended to solve the problem of multiple bodies in a radial freestream.

3.5.6. The non-uniform freestream

For potential flow fields, a radial freestream must be simulated by a source or sink flow because it is the only type of radial flow that satisfies the continuity equation. Unlike the usual uniform flow pattern that is used as a freestream, the value of a radial freestream may differ from point to point in a flow field. The freestream velocity at a point is therefore a function of the position at that point:

$$\mathbf{V}_\infty(x, y) = \mathbf{i} V_\infty(x, y)\cos\alpha_\infty(x, y) + \mathbf{j} V_\infty(x, y)\sin\alpha_\infty(x, y) \tag{3-46}$$

where $V_\infty(x, y)$ is the speed of the freestream at (x, y) and $\alpha_\infty(x, y)$ is the direction of the freestream at (x, y) in relation to the global coordinate system's x-axis. For the uniform flow freestream with speed V_∞ and direction α_∞ the values are constant throughout the flow field, i.e.

$$V_\infty(x, y) = V_\infty \tag{3-47}$$

$$\alpha_\infty(x, y) = \alpha_\infty \tag{3-48}$$

For the radial flow freestream that is calculated by means of the source flow method:

$$V_\infty(x, y) = \frac{\Lambda}{2\pi\sqrt{x^2 + y^2}} \tag{3-49}$$

$$\alpha_\infty(x, y) = \arctan\frac{y}{x} \tag{3-50}$$

The source singularity is placed at the origin of the global coordinate system. The source strength is denoted by Λ which is physically the rate of volume flow from the source, per unit depth perpendicular to the page. Again, the inverse tangent must be evaluated in the range $(-\pi, \pi)$ by taking proper account of the quadrant in which

the angle is evaluated. The individual signs of the numerator and denominator of equation (3-50) indicate the quadrant in which the angle is evaluated.

Substituting equation (3-46) into the numerical model of the inviscid, incompressible flow field as detailed by equations (3-24) and (3-27) yields

$$\sum_{i=1}^{N}\frac{\sigma_i}{4\pi}\left[n_{xj}C_{xi}\left(x_j,y_j\right)+n_{yj}C_{yi}\left(x_j,y_j\right)\right] \qquad (3\text{-}51)$$
$$-\frac{\Gamma}{2\pi S}\sum_{i=1}^{N}\left[n_{xj}G_{xi}\left(x_j,y_j\right)+n_{yj}G_{yi}\left(x_j,y_j\right)\right]$$
$$=-n_{xj}V_{\infty j}\cos\alpha_j-n_{yj}V_{\infty j}\sin\alpha_j$$
$$j=1,2,\ldots,N$$

and

$$\sum_{i=1}^{N}\frac{\sigma_i}{4\pi}\begin{bmatrix}t_{xm}C_{xi}\left(x_m,y_m\right)+t_{ym}C_{yi}\left(x_m,y_m\right)\\+t_{xn}C_{xi}\left(x_n,y_n\right)+t_{yn}C_{yi}\left(x_n,y_n\right)\end{bmatrix} \qquad (3\text{-}52)$$
$$-\frac{\Gamma}{2\pi S}\sum_{i=1}^{N}\begin{bmatrix}t_{xm}G_{xi}\left(x_m,y_m\right)+tn_{ym}G_{yi}\left(x_m,y_m\right)\\+t_{xn}G_{xi}\left(x_n,y_n\right)+tn_{yn}G_{yi}\left(x_n,y_n\right)\end{bmatrix}$$
$$=-V_{\infty m}\left(t_{xm}\cos\alpha_m+t_{ym}\sin\alpha_m\right)-V_{\infty n}\left(t_{xn}\cos\alpha_n+t_{yn}\sin\alpha_n\right)$$

This then is the set of equations for the more general case of a freestream that is a function of position from which the unknown source strengths and vorticity can be calculated. The velocities are calculated by means of equations (3-43) and (3-44) and the pressure distribution by equation (3-45).

3.5.7. Parabolic vorticity strength distribution on a body surface

Equations (3-51) and (3-52) represent the case for a constant strength vorticity distribution over the body surface. For airfoils with cusped trailing edges though, better results are obtained by means of a parabolic vorticity distribution that varies along the surface length around the body with a zero value at the trailing edge on both the upper and lower surfaces. In appendix B it is shown that a parabolic vorticity distribution along the surface of an airfoil is given by

$$\gamma(s)=-\frac{6\Gamma}{S^3}s^2+\frac{6\Gamma}{S^2}s \qquad (3\text{-}53)$$

where s is the distance from the trailing edge along the surface of the airfoil taken in an anti-clockwise direction and S is the total length of the surface of the airfoil.

To replace the constant vortex distribution with the parabolic vortex distribution, equation (3-53) is substituted into equation (3-16). Applying the result to the ith panel on the panelled body yields the disturbance velocity potential induced at an arbitrary point (x, y) in the flow by the ith panel

$$\phi_i(x,y) = \frac{\sigma_i}{4\pi}\int_{S_i} \ln\left[(x-\xi)^2 + (y-\eta)^2\right] ds \qquad (3\text{-}54)$$
$$-\frac{3\Gamma}{\pi S^2}\Sigma_i\left(1-\frac{\Sigma_i}{S}\right)\int_{S_i} \arctan\left[(y-\eta)/(x-\xi)\right] ds$$

where

$\Sigma_i = \sum_{j=1}^{i} s_j$ = length of all the panels from the trailing edge up to

and including panel *i* and

$S = \Sigma_N = \sum_{j=1}^{N} s_j$ = total length of all the panels on the airfoil

The disturbance velocity potential at (x, y) induced by the varying source and the elliptical vortex distribution on all N panels is given by the sum of the disturbance velocity potentials of the individual panels:

$$\phi(x,y) = \sum_{i=1}^{N} \phi_i(x,y) \qquad (3\text{-}55)$$
$$= \sum_{i=1}^{N} \frac{\sigma_i}{4\pi}\int_{S_i} \ln\left[(x-\xi)^2 + (y-\eta)^2\right] ds$$
$$-\frac{3\Gamma}{\pi S^2}\sum_{i=1}^{N}\left\{\Sigma_i\left(1-\frac{\Sigma_i}{S}\right)\int_{S_i} \arctan\left[(y-\eta)/(x-\xi)\right] ds\right\}$$

The integrals are the same influence coefficients defined in equation (3-21). Therefore equation (3-61) can be rewritten in a simpler form:

$$\phi(x,y) = \sum_{i=1}^{N} \frac{\sigma_i}{4\pi} C_i(x,y) - \frac{3\Gamma}{\pi S^2}\sum_{i=1}^{N}\Sigma_i\left(1-\frac{\Sigma_i}{S}\right) G_i(x,y) \qquad (3\text{-}56)$$

Equation (3-56) satisfies both the governing equation for inviscid, irrotational, incompressible flow expressed by equation (2-11) and the infinity boundary condition expressed by equation (3-2). The remaining boundary condition is the solid boundary condition as expressed by equation (3-4). In order to satisfy this boundary con-

dition, equation (3-56) is substituted into equation (3-4) and applied at every panel on the body to yield

$$\sum_{i=1}^{N}\frac{\sigma_i}{4\pi_i}\left[n_{xj}C_{xi}\left(x_j,y_j\right)+n_{yj}C_{yi}\left(x_j,y_j\right)\right] \tag{3-57}$$
$$-\frac{3\Gamma}{\pi S^2}\sum_{i=1}^{N}\Sigma_i\left(1-\frac{\Sigma_i}{S}\right)\left[n_{xj}G_{xi}\left(x_j,y_j\right)+n_{yj}G_{yi}\left(x_j,y_j\right)\right]$$
$$=-n_{xj}V_{\infty j}\cos\alpha_j-n_{yj}V_{\infty j}\sin\alpha_j$$
$$j=1,2,...,N$$

where $\left(x_j,y_j\right)$ denotes the coordinates of the control point of panel j, n_{xj} and n_{yj} denotes the x- and y-components of the unit vector normal to panel j respectively and $V_{\infty j}$ and α_j denotes the freestream speed and freestream angle respectively at the control point of panel j. They are functions of position and calculated by means of equations (3-49) and (3-50).

Together with equations (3-57) the extra equation created by the application of the Kutta condition leads to the non-singular set of linear algebraic equations that can be solved for the unknown sources σ_i and total circulation Γ. Substituting equation (3-56) into equation (3-26) yields the new equation for the Kutta condition:

$$\sum_{i=1}^{N}\frac{\sigma_i}{4\pi}\begin{bmatrix}t_{xm}C_{xi}\left(x_m,y_m\right)+t_{ym}C_{yi}\left(x_m,y_m\right)\\+t_{xn}C_{xi}\left(x_n,y_n\right)+t_{yn}C_{yi}\left(x_n,y_n\right)\end{bmatrix} \tag{3-58}$$
$$-\frac{3\Gamma}{\pi S^2}\sum_{i=1}^{N}\Sigma_i\left(1-\frac{\Sigma_i}{S}\right)\begin{bmatrix}t_{xm}G_{xi}\left(x_m,y_m\right)+t_{ym}G_{yi}\left(x_m,y_m\right)\\+t_{xn}G_{xi}\left(x_n,y_n\right)+t_{yn}G_{yi}\left(x_n,y_n\right)\end{bmatrix}$$
$$=-V_{\infty m}\left(t_{xm}\cos\alpha_m+t_{ym}\sin\alpha_m\right)-V_{\infty n}\left(t_{xn}\cos\alpha_n+t_{yn}\sin\alpha_n\right)$$

As in the case for a constant vortex distribution on the surface of the body, the velocities are again calculated at the control points of the panels. Substituting equation (3-56) into equation (3-41) yields the components of the velocity vector at the control point of a panel. The resulting equations for the velocity components are:

$$V_x\left(x_j,y_j\right)=V_{\infty x}\left(x_j,y_j\right)+\sum_{i=1}^{N}\frac{\sigma_i}{4\pi}C_{xi}\left(x_j,y_j\right) \tag{3-59}$$
$$-\frac{3\Gamma}{\pi S^2}\sum_{i=1}^{N}\Sigma_i\left(1-\frac{\Sigma_i}{S}\right)G_{xi}\left(x_j,y_j\right)$$

$$V_y(x_j, y_j) = V_{\infty y}(x_j, y_j) + \sum_{i=1}^{N} \frac{\sigma_i}{4\pi} C_{yi}(x_j, y_j) \qquad (3\text{-}60)$$
$$- \frac{3\Gamma}{\pi S^2} \sum_{i=1}^{N} \Sigma_i \left(1 - \frac{\Sigma_i}{S}\right) G_{yi}(x_j, y_j)$$

The pressure distribution around the body are calculated at the control points of the panels by means of equation (3-45).

3.5.8. Multiple bodies in a non-uniform freestream

The last objective is to expand equations (3-57) and (3-28) to cover the more general case of having more than one body in the freestream. For several profiles simultaneously equation (3-56) for one body is summed over all the bodies and becomes:

$$\phi(x, y) = \sum_{k=1}^{M} \left[\sum_{i=1}^{N_k} \frac{\sigma_{ik}}{4\pi} C_{ik}(x, y) - \frac{3\Gamma_k}{\pi S_k^2} \sum_{i=1}^{N_k} \Sigma_{ik} \left(1 - \frac{\Sigma_{ik}}{S_k}\right) G_{ik}(x, y) \right] \qquad (3\text{-}61)$$
$$= \sum_{k=1}^{M} \sum_{i=1}^{N_k} \frac{\sigma_{ik}}{4\pi} C_{ik}(x, y) - \sum_{k=1}^{M} \frac{3\Gamma_k}{\pi S_k^2} \sum_{i=1}^{N_k} \Sigma_{ik} \left(1 - \frac{\Sigma_{ik}}{S_k}\right) G_{ik}(x, y)$$

where k is the profile index and i the panel on the profile k's index. As stated earlier, due to the linear nature of the problem, the summation of the particular solutions presented by equation (3-56), also leads to a solution of the governing equation as well as the infinity boundary condition. Therefore equation (3-61) also satisfies the governing equation and the infinity boundary condition. To satisfy the wall boundary condition at all the wall boundaries, equation (3-61) is substituted into equation (3-4) and applied to all the panels of all the bodies:

$$\sum_{k=1}^{M} \sum_{i=1}^{N_k} \frac{\sigma_{ik}}{4\pi} \left[n_{xjl} C_{xik}(x_{jl}, y_{jl}) + n_{yjl} C_{yik}(x_{jl}, y_{jl}) \right] \qquad (3\text{-}62)$$
$$- \sum_{k=1}^{M} \frac{3\Gamma_k}{\pi S_k^2} \sum_{i=1}^{N_k} \Sigma_{ik} \left(1 - \frac{\Sigma_{ik}}{S_k}\right) \left[n_{xjl} G_{xik}(x_{jl}, y_{jl}) + n_{yjl} G_{yik}(x_{jl}, y_{jl}) \right]$$
$$= -\left[n_{xjl} V_{\infty jl} \cos\alpha_{jl} + n_{yjl} V_{\infty jl} \cos\alpha_{jl} \right]$$
$$j = 1,2,...., N_l$$
$$l = 1,2,..., M$$

The application of the Kutta condition on body *l* yields:

$$\mathbf{V}_{ml} \cdot \mathbf{t}_{ml} = -\mathbf{V}_{nl} \cdot \mathbf{t}_{nl} \text{ or} \qquad (3\text{-}63)$$
$$\left[\mathbf{V}_{\infty ml} + \nabla\phi(x_{ml}, y_{ml}) \right] \cdot \mathbf{t}_{ml} = -\left[\mathbf{V}_{\infty nl} + \nabla\phi(x_{nl}, y_{nl}) \right] \cdot \mathbf{t}_{nl}$$

Substitution of equation (3-61) into equation (3-62) yields:

$$\sum_{k=1}^{M}\sum_{i=1}^{N_k}\frac{\sigma_{ik}}{4\pi}\begin{bmatrix}t_{xml}C_{xik}(x_{ml},y_{ml})+t_{yml}C_{yik}(x_{ml},y_{ml})\\+t_{xnl}C_{xik}(x_{nl},y_{nl})+t_{ynl}C_{yik}(x_{nl},y_{nl})\end{bmatrix} \tag{3-64}$$

$$-\sum_{k=1}^{M}\frac{3\Gamma_k}{\pi S_k^2}\sum_{i=1}^{N_k}\Sigma_{ik}\left(1-\frac{\Sigma_{ik}}{S_k}\right)\begin{bmatrix}t_{xml}G_{xik}(x_{ml},y_{ml})+t_{yml}G_{yik}(x_{ml},y_{ml})\\+t_{xnl}G_{xik}(x_{nl},y_{nl})+t_{ynl}G_{yik}(x_{nl},y_{nl})\end{bmatrix}$$

$$=-\mathbf{V}_{\infty ml}\cdot\mathbf{t}_{ml}-\mathbf{V}_{\infty nl}\cdot\mathbf{t}_{nl}$$

$$=-V_{\infty ml}\left[t_{xml}\cos\alpha_{ml}+t_{yml}\sin\alpha_{ml}\right]-V_{\infty nl}\left[t_{xnl}\cos\alpha_{nl}+t_{ynl}\sin\alpha_{nl}\right]$$

$$l=1,2,...,M$$

Equations (3-62) and (3-64) forms a non-singular set of linear algebraic equations from which the unknown source and vortex strengths can be solved for all the panels on all the bodies. Figure 3-7 graphically represents the system of linear algebraic equations.

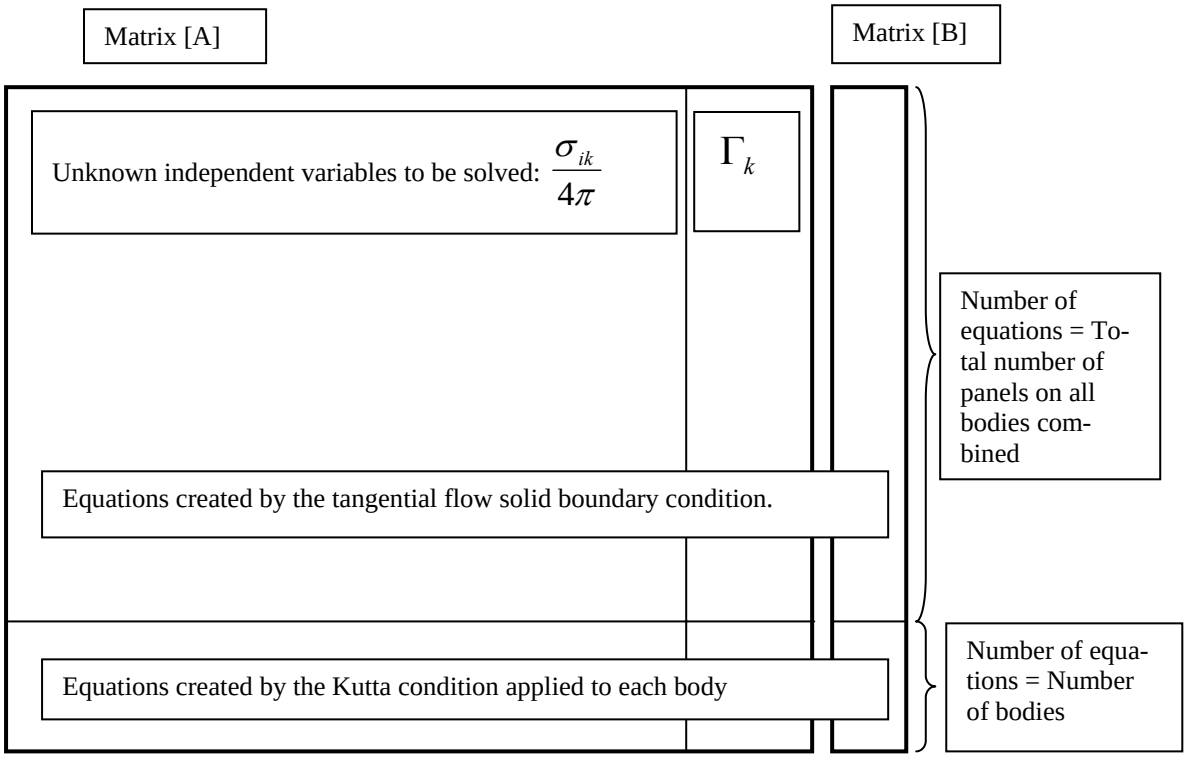

Figure 3-7. Linear equation system.

Substituting equation (3-61) into equation (3-41) yields the components of the velocity vector at the control point of a panel. From the resulting equation the flow velocity at the control point of panel *j* on body *l* by inspection yields:

$$V_x\left(x_{jl},y_{jl}\right)=V_{\infty jl}\cos\alpha_{jl}+\sum_{k=1}^{M}\sum_{i=1}^{N_k}\frac{\sigma_{ik}}{4\pi}C_{xik}\left(x_{jl},y_{jl}\right) \tag{3-65}$$
$$-\sum_{k=1}^{M}\frac{3\Gamma_k}{\pi S_k^2}\sum_{i=1}^{N_k}\Sigma_{ik}\left(1-\frac{\Sigma_{ik}}{S_k}\right)G_{xik}\left(x_{jl},y_{jl}\right)$$

$$V_y\left(x_{jl},y_{jl}\right)=V_{\infty jl}\sin\alpha_{jl}+\sum_{k=1}^{M}\sum_{i=1}^{N_k}\frac{\sigma_{ik}}{4\pi}C_{yik}\left(x_{jl},y_{jl}\right) \tag{3-66}$$
$$-\sum_{k=1}^{M}\frac{3\Gamma_k}{\pi S_k^2}\sum_{i=1}^{N_k}\Sigma_{ik}\left(1-\frac{\Sigma_{ik}}{S_k}\right)G_{yik}\left(x_{jl},y_{jl}\right)$$

The lift force on any body in the flow field is obtained by applying the Kutta-Joukowski law as expressed by equation (3-17) to that body:

$$L'_l=\rho_\infty V_\infty\Gamma_l \quad \text{where } l=1,2,...\text{or } M \tag{3-67}$$

A more cumbersome method of calculating the lift force on a body is by integrating the pressure distribution on the surface of the body. In fact, the circulation used in the Kutta-Joukowski law is a simple quantity determined from that pressure distribution.

3.6. Implementation of the source-vortex panel method

The source-vortex panel method was implemented by means of a Windows based computer program, called Abreast. It is written in Visual Basic 6. It uses a multiple document interface form as a user interface. Figure 3-8 shows that the Abreast interface window consists of a menu bar at the top and a fixed profile setting tool on the left. A Graph form and an output form occupy the remainder of the interface. A Flow setting tool that can be activated via the menu bar at the top is also provided.

The menu bar at the top contains the usual icons that are used to control a text window. Included are icons that activate the Excel spreadsheet that contains profile data. Abreast can upload this profile data and incorporates it in the flow project. Output from the Abreast flow project can also be dumped into the Excel spreadsheet for easy post processing.

A further addition to the menu bar at the top is an input tool for the ABCOL-commands. ABCOL is the acronym for Abreast Control Language. These com-

mands control the flow project setup and calculation processes. The progress in the setup and calculation of the flow project is reported in the output form in the lower right-hand side of the Abreast window.

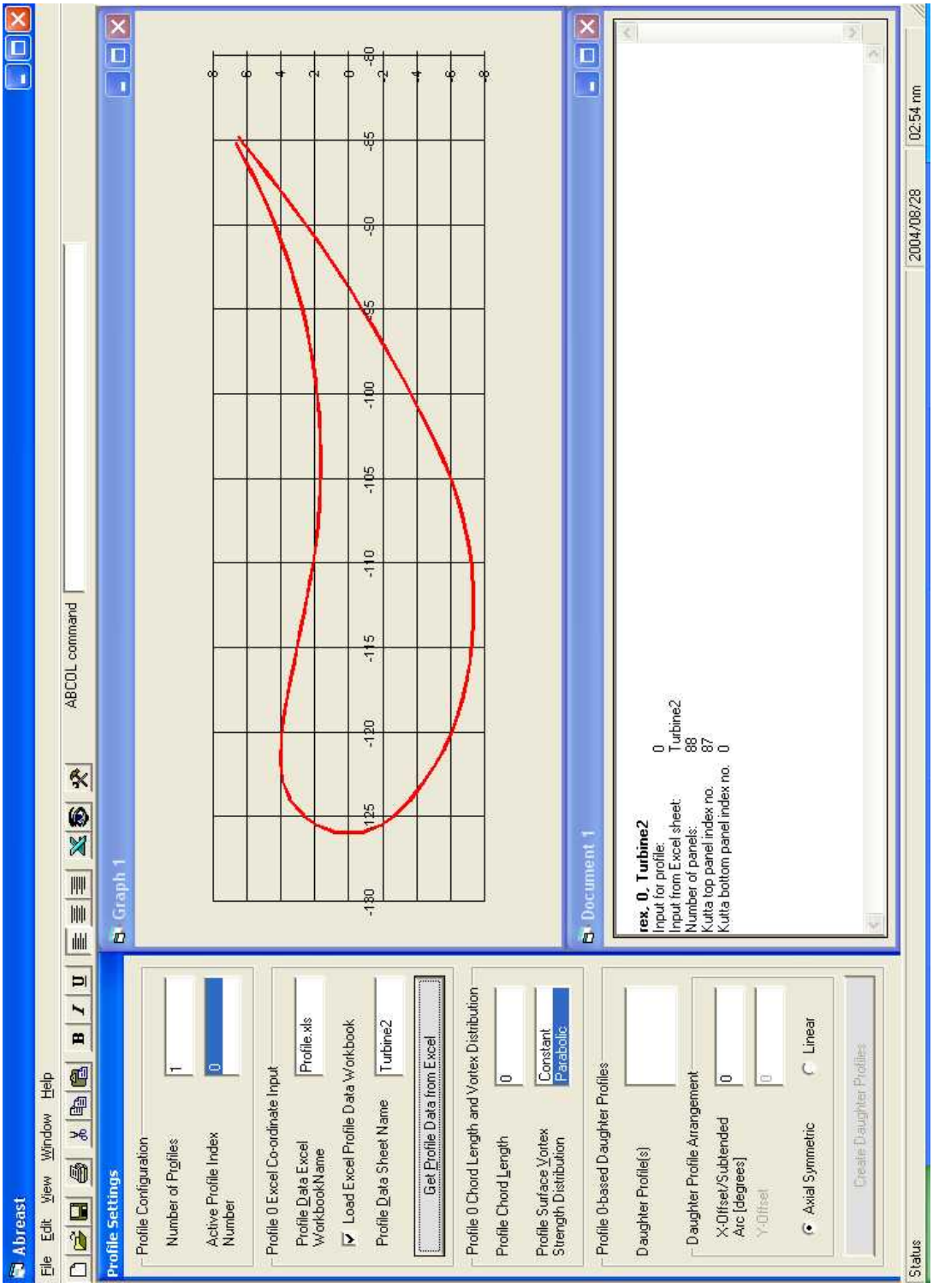

Figure 3-8. Abreast user interface.

The program consists of several forms with their customised methods and events procedures. These forms are the profile and flow setting tools, the graph form and the output document form. Attached to the program is a class module that interfaces with the main program by means of events and procedures. The class module receives profile data from the main program and on demand calculates the results and makes it available to the main program. Attached to the panel method class is an auxiliary class that solves a set of linear equations by means of Gaussian elimination with partial pivotal row interchanges and row scaling. The latter two techniques minimise truncation errors. Double precision floating-point data types are used in the calculation procedures to further minimise truncation errors. Both these classes are autonomous and may be used in other programs. The linear equations class interfaces with the panel method class, or any other program for that matter, by means of the necessary customised methods, events and properties. They are defined by means of program code inside them.

The profile setting tool is situated on the left-hand side of the Abreast window. This tool is used to modify the profiles in the flow project. Profile data are usually imported from an Excel spreadsheet where it can be easily pre-processed. It can also be input or modified via the ABCOL command box in the top menu. The usual method is to import or set up the base profile. The profile tool provides the facility to spawn daughter profiles based on the base profile in a specified cascade setup. The cascade can be arranged axial-symmetrically or rectilinearly. Multiple cascades of any arrangement can be set up. The vortex strength distribution on the surface of the profiles in the freestream can also be set individually to either a constant or a parabolic distribution. The individual profiles are displayed in the graph form in the upper right-hand side of the Abreast window.

The flow setup tool is invoked via an icon on the top menu bar. This tool is used to specify the freestream and the position of the reference point. The velocity at the reference point is used to calculate the pressure coefficients on the bodies. The freestream may be either uniform or radial. When the uniform freestream option is selected the freestream speed and angle must be set. In the case of the radial

freestream option, only the strength of the source that induces the flow needs to be set.

A flow speed calculating tool for the quick specification of a number of points where the flow speed is desired is also available. This tool acts like a pitot rake to obtain the speed at a number of points in a set pattern. The points can be specified in either a linear or a circumferential pattern. The specification of the points is according to a right-hand side Cartesian coordinate system for the case of a linear pattern. For the case of a circumferential pattern point positions are calculated according to a polar coordinate system with angles taken as positive in the anti-clockwise direction.

After the profile and freestream setup is completed, the calculation of the results is effected by means of an ABCOL command. Aspects of the flow project can be modified and the results recalculated. In order to calculate the results after modifications more efficiently, only the calculations necessitated by the changes are done to compute the new results. The results are displayed in the output box on the lower right-hand side of the Abreast window. The results can be copied to a program like Excel for post-processing. It can also be saved and printed.

3.7. Code validation

The mathematical model and the computer program were first validated by comparing its predictions of the salient flow properties of some known cases with the known values. Then the program is used to predict the flow through the second turbine. The predictions are compared against empirical values.

3.7.1. Single profile, uniform flow field

A single NACA 0012 profile in a uniform flow field at a 5-degree angle of attack was used to test the accuracy of the program for the case of a single profile. The chord length was taken as 41.293 to bring the profile to the same size order as the turbine blades that were studied in this project. This enables us to compare the sum

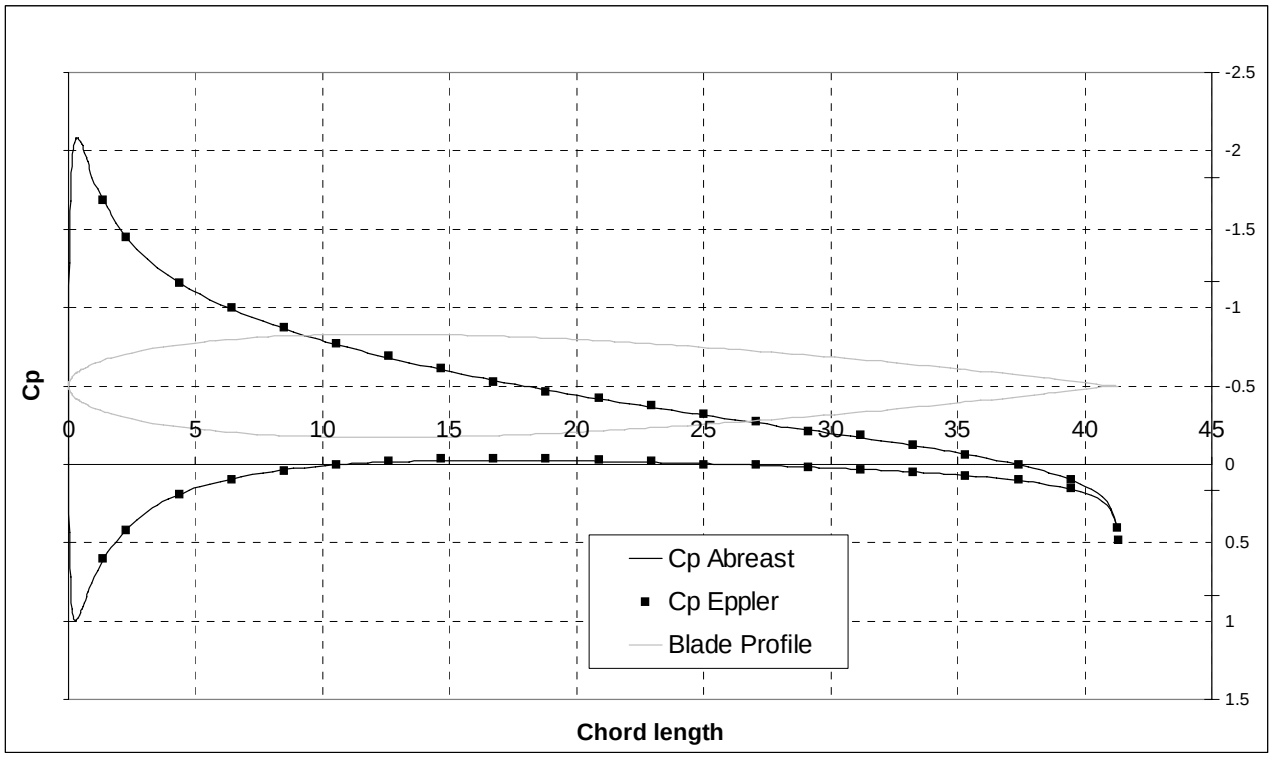

Figure 3-9. Pressure distribution on a NACA 0012 airfoil in a uniform freestream at a 5-degree angle of attack.

of the sources on the blade surface of this test with the same parameter of the torque converter results. Because the sum of the sources on the surface of a profile must be zero or else the body itself would be adding or absorbing mass from the flow, this parameter can be used as an accuracy indicator. If the body itself is adding or sub-

Freestream type	Uniform
Freestream speed	1
Freestream angle	5-degrees
Number of profiles	1
Number of panels	242
Total length of panels	84.215
Predicted C_l	0.60551
Total source strength	0.02568
Chord length	41.293

Table 3-1. Results of the NACA 0012 test.

tracting mass from the flow, it means that the flow across at least parts of the body surface is finite which is a clear violation of the solid wall boundary condition imposed here. The prediction obtained by the program is shown in figure (3-9) and compared with the results published in Eppler (1990). Excellent agreement with the published results is obtained. The salient parameters of the analysis are summarised in table (3-1).

3.7.2. Multiple profile cascade in a uniform flow field

Sixteen circles with a diameter of 2 units each separated by channels with a width of 1 unit were used to model a cascade of two-dimensional circular cylinders with a space-chord ratio of 1.5. The theoretical mass flow through a channel between two cylinders was then compared with the predicted mass flow through the channel through the middle of the model. One of the repeating units of the model is depicted

Figure 3-10. Flow between adjacent cylinders in a cascade of cylinders.

in figure (3-10). It consists of the two-dimensional stream tube approaching two cylinders. The flow that passes through the channel between two cylinders is between two streamlines *ab* and *fe* that stretch from infinity to the front stagnation points of the cylinders. The width of such a streamline channel at infinity for this cascade is 3 units. That consists of half the diameter of one of the cylinders, the width of the channel between them and half the diameter of the adjacent cylinder. The freestream was specified as uniform with a velocity of 1 unit per second.

When the principle of the conservation of mass is applied to a finite fixed control volume the integral conservation form of the continuity equation is obtained:

$$\frac{\partial}{\partial t}\iiint_{CV}\rho d(\text{vol}) + \oiint_{CS}\rho\mathbf{V}\cdot\mathbf{dS} = 0 \qquad (3\text{-}68)$$

Here, **V** is the velocity at a point **dS** on the surface of the control volume and ρ is the density at that point. Therefore equation (3-68) can be applied to the finite fixed control volume of figure (3-10) denoted by *abcdef*. Because the flow is steady, the first term of equation (3-68) which is a time derivative, vanishes throughout the control volume. The second term of equation (3-68) is applied at the control surface. The control surface sections denoted by *ab*, *bc*, *de* and *ef* are streamlines of the flow because no flow passes through them. Since by definition **V** is parallel to the streamlines and **dS** is perpendicular to the control surface, along these sections **V** and **dS** are perpendicular vectors, and hence $\mathbf{V} \cdot \mathbf{dS} = 0$. Thus, the only contributions to the integral in equation (3-68) come from control surface sections *fa* and *cd*.

The control volume, being two-dimensional, has a unit depth in the z direction. Hence, for sections *fa* and *cd* which are oriented in the y direction, $dS = dy(1)$. The remaining term in equation (3-68) then becomes

$$\oiint_{CS} \rho \mathbf{V} \cdot \mathbf{dS} = -\int_f^a \rho u_1 dy + \int_c^d \rho u_2(y) dy = 0 \qquad (3\text{-}69)$$

The minus sign in front of the first term on the right-hand side of equation (3-69) is due to **V** and **dS** being in opposite directions along *fa*. This is an inflow boundary. Note also that the flow is incompressible, and hence $\rho = \text{const}$. From equation (3-69) it follows that

$$\int_f^a \rho u_1 dy = \int_c^d \rho u_2(y) dy \text{, or}$$

$$u_1 \int_f^a dy = \int_c^d u_2(y) dy \qquad (3\text{-}70)$$

Because the distance from *f* to *a* in the model is 3, the integral on the left-hand side of equation (3-70) evaluates to 3. The integral on the right-hand side indicates that the lengths of the infinite number of infinitesimally small line segments between *c* and *d* are multiplied by the velocity $u_2(y)$ at each segment. In order to solve the integral numerically with the velocity known at only a finite number of points, the integral must be discretised. The average velocity along the finite line segments is approximated by choosing the line segments in such a way that the points at which the velocity is known is situated in the middle of that line segments. Noting that the freestream velocity was specified as 1, equation (3-70) becomes

$$3 = \sum_{i=1}^{N} u_{2i} \cdot y_i \tag{3-71}$$

where y_i is the length of the ith line segment and u_{2i} is the velocity at the middle of the ith line segment at station 2. N is the number of finite length line segments into which segment *cd* has been divided. If the line segments are of equal length, equation (3-71) evaluates to

$$\Delta y \sum_{i=1}^{N} u_{2i} = 3 \tag{3-72}$$

where Δy is the length of each of the line segments of *cd*. The central channel of the cascade of 16 cylinders was divided into 40 sections, each with a length of 0.025.

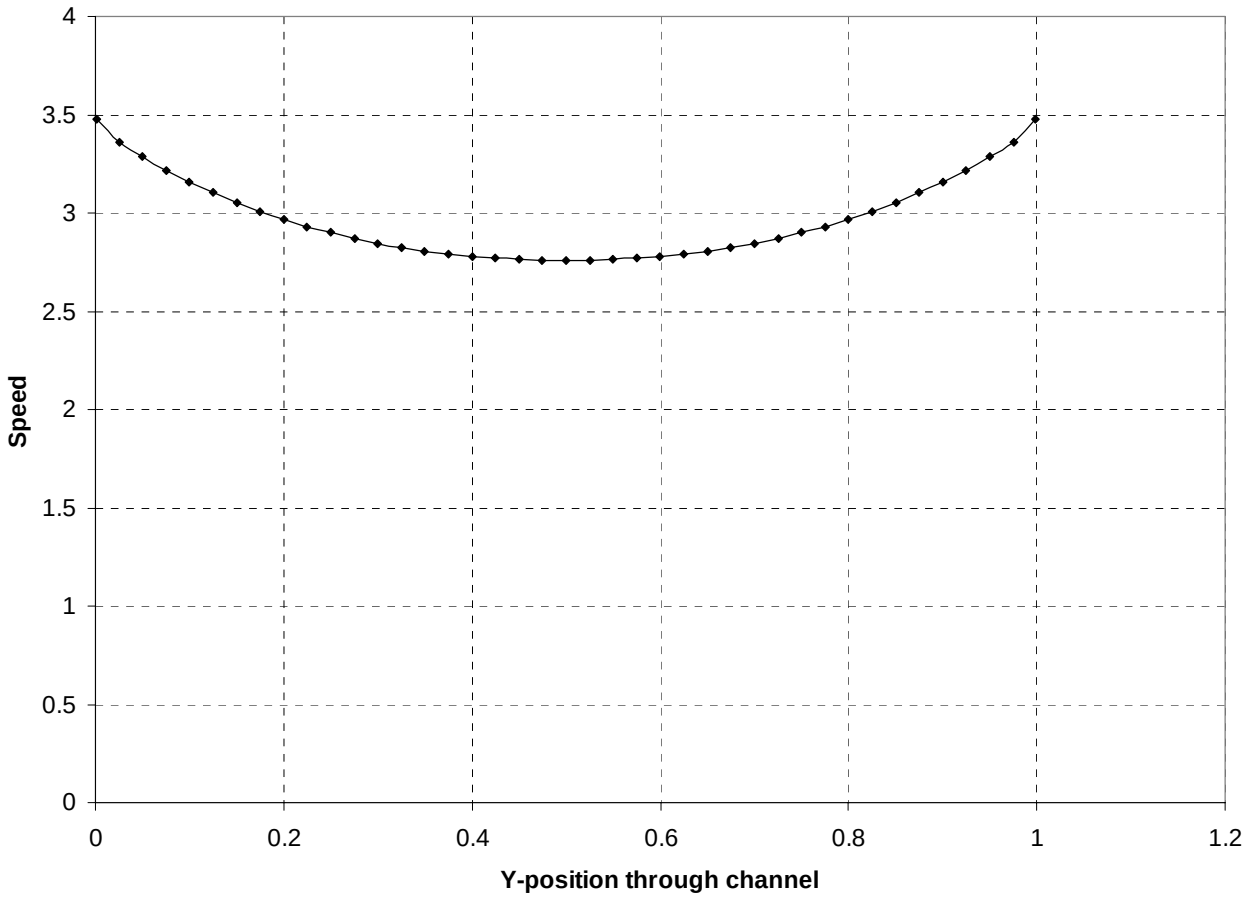

Figure 3-11. Predicted speed distribution in a typical channel in a cascade of cylinders.

The velocity in the middle of each section was calculated. The results are shown in table (3-2).

$\sum_{i=1}^{N} u_{2i}$	118.5
Δy	0.025
$\Delta y \sum_{i=1}^{N} u_{2i}$	2.963
% difference between theoretical and predicted values	1.22%

Table 3-2. Main attributes of the velocity distribution in a typical channel of a cascade of cylinders.

As shown in table (3-2), substituting these velocities in equation (3-72) yields 2.963447. This value differs by 1.22% from the theoretical value of 3.0. The velocity distribution through the channel is shown in figure (3-11). This shows a perfectly symmetric pattern as expected.

3.8. The second turbine cascade

An important prerequisite for the success of a potential flow analysis is that the boundary layer on the blades of the second turbine cascade is too thin to have a discernible influence on the freestream. The Reynolds number calculated by Venter (1993) for the flow at the trailing edge of the turbine blades is 2.6×10^5. This is less than the transition point to turbulent flow for flat plates, even in the presence of a slight amount of freestream turbulence. One of the lowest transition points predicted for flat plate flow is at a Reynolds number of 2 027 000 by Smith and Gamberoni (1956) as reported by White (1991). The boundary layer on the blades of the second turbine blade row can therefore with reasonable certainty be taken as laminar for most of the blade. The parameter that specifies the displacement of the streamlines due to the flow retardation caused by the boundary layer is the displacement thickness. The velocity profile, and therefore the displacement thickness of the boundary layer on the actual blade wall will be different from that of the boundary layer on a flat plate due to different pressure gradients over the respective surfaces. Computing the simpler flat plate boundary layer displacement thickness nevertheless gives an idea of the magnitude of the displacement on the second turbine blades. Blasius'

formula for the displacement thickness of the boundary layer on flat plates as reported by White (1991) is

$$\frac{\delta^*}{x} = \frac{1.7208}{\sqrt{\mathrm{Re}_x}} \tag{3-73}$$

For a chord length of 41.2mm and a Reynolds number of 2.6 X 10^5 as reported by Venter (1993) the displacement thickness at the trailing edge from Blasius' flat plate formula is 0.14mm. Hence the boundary layer over the largest part of the blade surface will be less than about 0.3% of the channel width between two consecutive blades. The boundary layer can therefore be expected to have a negligible influence on the streamlines around the second turbine blade row in the absence of boundary layer separation. Its influence on the streamline pattern around the blades can be safely neglected.

Due to their close proximity to the entrance of the 2nd turbine cascade the stator blades play a crucial role in the velocity distribution of the flow field through the second turbine cascade and they have to be included in the analysis. It was further established that to improve the accuracy of the numerical model, the number of panels on any element had to be increased. Hence, with the severe limitation of the available memory on the computer on which the problem can be calculated, a judicious trade-off between more elements and more panels on the elements had to be found. Eventually 10 turbine elements and 23 stator elements were used to simulate the complete stator and turbine cascades. The freestream was specified as a radial freestream with a source strength of –110. The negative value is to change the source flow of the freestream into sink flow. For comparative purposes the reference point was specified in the same position as the reference point used by Venter (1993) when he measured the pressure distribution around a turbine blade. The position of the freestream reference point is shown in table (3-3). The panel distribution of the original 2nd turbine blade from which the rest of the turbine blades in the turbine cascade was copied is shown in figure (3-12).

Our predicted direction of the velocity at the freestream reference point is very close to the value measured by Venter (1993) as shown in table (3-3). The predicted pres-

Freestream type	Radial inflow
Freestream source strength	-110
Reference point x-coordinate	-124.4 mm
Reference point y-coordinate	19.71 mm
Predicted velocity direction at the reference point with the stator by Abreast.	54.6 degrees
Predicted velocity direction at the reference point without the stator by Abreast.	87.07 degrees
Measured velocity direction at the reference point by Venter (1993)	54.3 degrees

Table 3-3. Panel method freestream data.

sure distribution is depicted in figure (3-13). This is compared with the values measured by Venter (1993) as well as the values that he predicted with his panel method. Venter's (1993) pressure distribution was predicted by means of a second order source panel method. He specified the second turbine blade row in isolation in a free spiral vortex instead of a purely radial inflow freestream. This arrangement

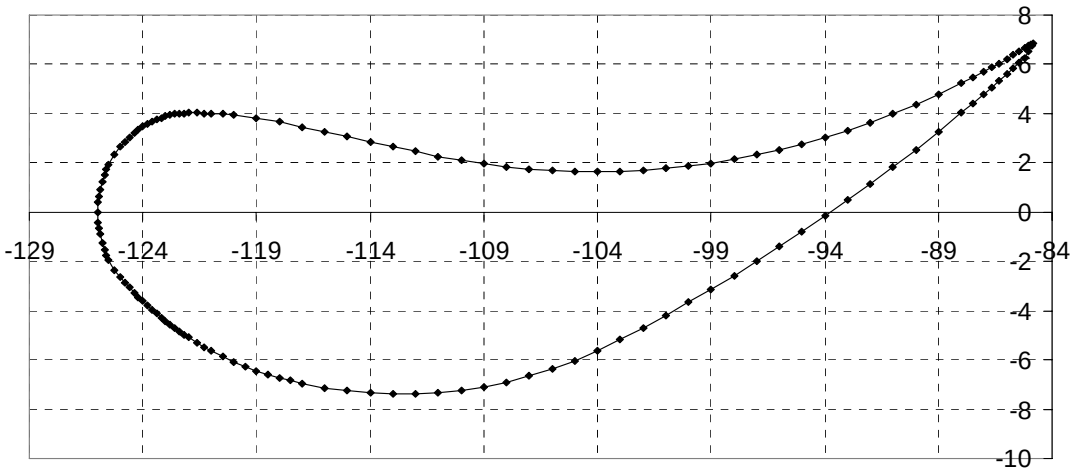

Figure 3-12. Panelled turbine blade.

forced the freestream to flow at an angle with respect to the cascade elements. Venter (1993) investigated several methods to improve the prediction of the pressure distribution on a blade in the second turbine cascade. The methods differ in the criteria that are used to determine the ratio of the vortex strength with respect to the

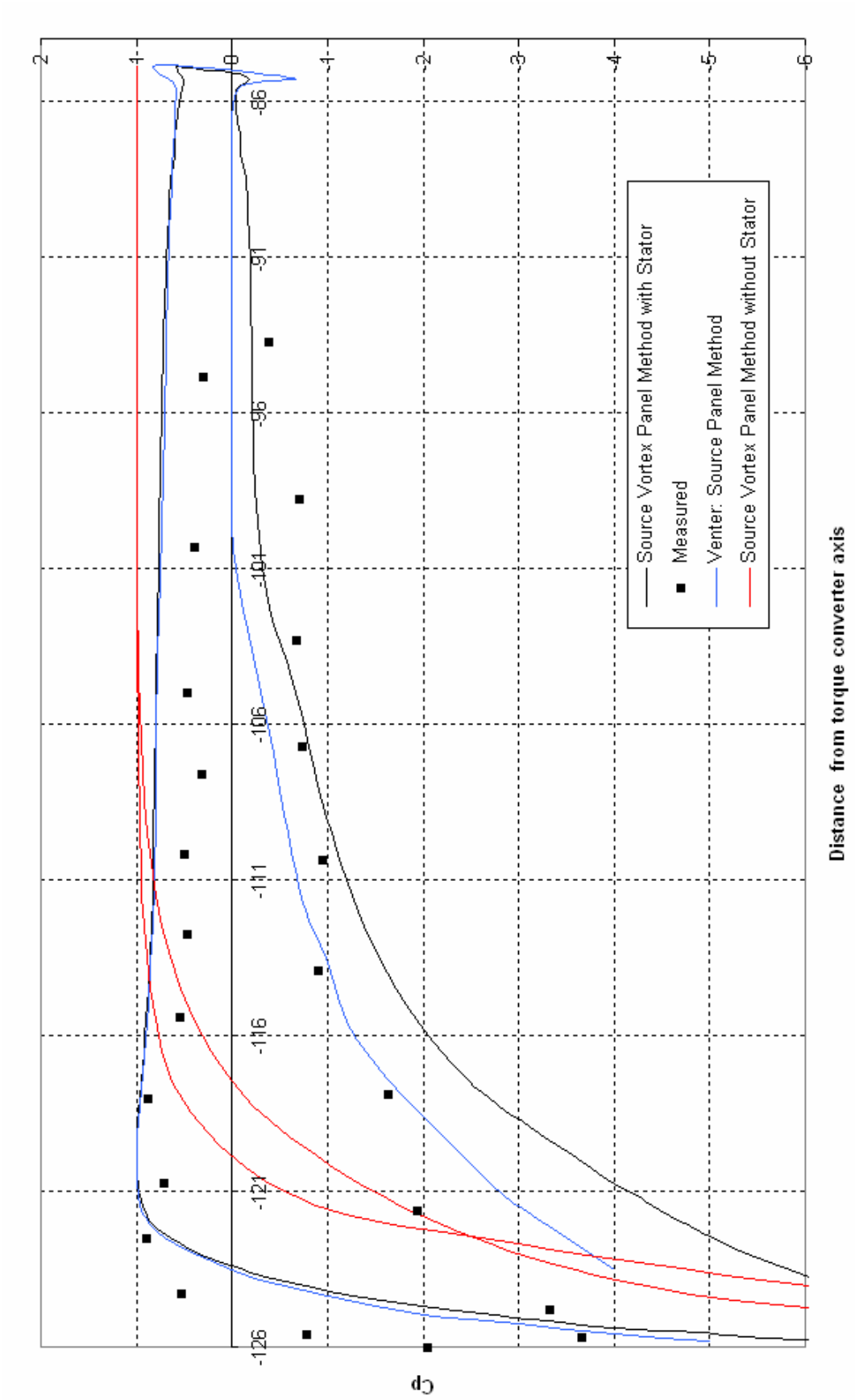

Figure 3-13. Pressure distribution on the surface of a 2nd turbine blade.

negative source flow strength which produces the desired free spiral vortex pattern. One method requires that the free spiral vortex must be set to predict the measured velocity direction of the reference point midway between the noses of two consecutive blades correctly. Venter's (1993) results from this method for the unmodified blade are compared with his measured pressure distribution as well as the results of this study in figure (3-13). Venter (1993) reports poor correlation between this method's predicted dimensionless pressure distribution and his measured dimensionless pressure distribution. Venter's preferred method led to an improved correlation between his predicted and measured dimensionless pressure distributions but at the same time poorly predicted the flow velocity direction at the reference point. The difference between his predicted and measured reference flow angles (Venter 1993) were in the order of 19 degrees.

Our predicted pressure distribution almost coincides with Venter's (1993) predicted pressure distribution on the suction surface. The predicted stagnation points also coincide as shown in figure (3-13). The predictions begin to deviate from the stagnation point and along the suction surface up to the trailing edge. The reasons for the differences lies in the different types of freestream utilised as well as the fact that the stator was included in the analysis of our panel method while it was ignored in Venter's (1993) panel method. The correlation between the pressure predictions of both panel methods and the measured values for the unmodified blade profiles are poor. Neither the distribution of the pressure around a typical blade nor the position of the stagnation point was correctly predicted as shown in figure (3-13).

To investigate the influence of the stator blade row, our panel method with the radial inflow freestream was used to analyse the pressure distribution on a second turbine blade without the presence of the stator blade row. The results are also shown in figure (3-13). The correlation between the predicted pressure distribution without the stator and the measured pressure distribution is extremely poor. It can therefore be inferred that it is important to include the stator blade row in the flow model of the 2nd turbine when a radial freestream is used since it directs the flow entering the turbine in the right direction. Even with this arrangement though, our panel method cannot accurately predict the pressure distribution on a turbine blade.

A further comparison was made with the velocities measured by Steenkamp (1996). The measurements were taken in a region between the stator and 2nd turbine blade rows and in another region in the channel between two consecutive blades of the 2nd turbine blade row. These measurements were taken in a two-dimensional plane at mid span of the second turbine blades. The measurements between the blade rows were made at twelve positions on a radius of 130mm from the torque converter axis. The measurement points were evenly distributed at intervals of 2.25 degrees from each other. The first point was placed directly in front of the leading edge of a blade of the second turbine blade row. The measurements in the channel between two consecutive blades were made at seven positions on a radius of 108mm from the torque converter axis. These measurement points were also evenly distributed at intervals of 1.75 degrees from each other. The positions of these points are listed in tables (3-4) and (3-5). The coordinate system used to fix the measurement points is a cartesian system with the origin placed at the axis of the torque converter. This is the same system used in figure (3-12). The blade in figure (3-12) can therefore be used as a reference blade.

No	X-coordinate	Y-Coordinate
1	-130	1.59E-14
2	-129.9554522	3.40300328
3	-1.30E+02	6.803674312
4	-129.5992534	10.19968244
5	-129.2878464	13.58870022
6	-128.887832	16.96840499
7	-128.3994843	20.33648046
8	-127.823138	23.69061831
9	-127.1591881	27.02851981
10	-126.4080897	30.3478973
11	-125.5703574	33.64647586
12	-124.6465655	36.92199481

Table 3-4. Measurement points in front of the 2nd turbine cascade.

No	X-coordinate	Y-Coordinate
1	-107.8972079	4.710893836
2	-107.70302	8.003716941
3	-107.4083647	11.28907403
4	-107.0135169	14.56390047
5	-106.5188449	17.82514143
6	-105.9248103	21.06975477
7	-105.231967	24.29471386

Table 3-5. Measurement points in the channel through the 2nd turbine cascade.

The speed values measured by Steenkamp (1996) and predicted by the Abreast program are depicted in figure (3-14) and figure (3-15) for the measurements in front of the 2nd turbine blade row and through the passage between two blades respectively. The speed values in figure (3-14) are plotted on an arc with a radius of 130mm. The arc begins at the first measurement point in front of the leading edge of a 2nd turbine blade and ends at the corresponding point in front of the consecutive blade. From figure (3-14) it is clear that the speed values predicted by the panel method and the viscous flow model vary much more smoothly than the corresponding measured speed values. The measured speed values tend to vary around a mean value. The patterns of the predicted values of the panel method and the viscous flow model are almost similar but seem out of phase. This may be attributed to the bulk of the flow being directed in slightly different directions by the two flow models. The predicted speed values of the viscous model as calculated by Flo++ have distinct minimum value in the region 10mm along the arc length where after it rises uniformly as it approaches the area in front of the nose of the next turbine blade. The predicted speed values of our panel method as calculated by our Abreast program have the same minimum value but it is shifted further along the arc length at 15mm. The shape of our panel method's speed distribution graph is almost the same as the shape of the viscous flow model's speed values as calculated by Flo++. The two distinctive local minimum values in the graph of the measured speed values are not readily explainable since they are about 24mm apart on the radius while the stator blade extensions from their trailing edges are 17mm apart at the radius on which the measurements were taken. The two speed discrepancies therefore are probably not due to the influence of stator blade wakes as might be expected at first glance.

The speed values in figure (3-15) are plotted on an arc with a radius of 108mm. The arc begins at an angle of 3.12 radians with respect to the x-axis of the reference co-ordinate system used in tables (3-4) and (3-5). It ends at an angle of 2.89 radians. The difference between the measured and predicted values in the passage between two adjacent blades is not as large as the difference between the measured and predicted speed values in front of the turbine blade row. Both the speed values predicted by our panel method and the values measured by Steenkamp (1996) have the same increase in speed from the pressure side to the suction side. The pressure side

is at the beginning of the arc and the suction side at the end of the arc. The speed curve that is predicted by the viscous flow model has about the same rate of increase as the panel method's predicted speed curve when moving along the arc from the pressure side towards the suction side. The viscous flow model's predicted speed distribution is discussed in chapter 4.

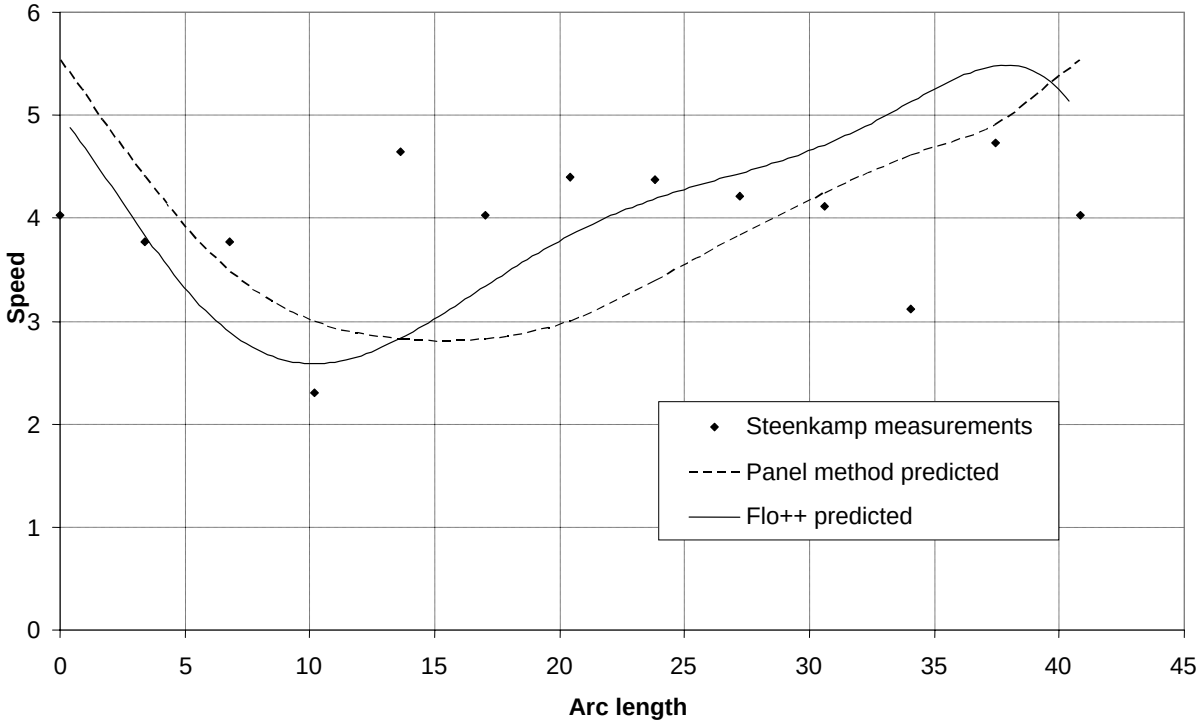

Figure 3-14. Speed distribution in front of the 2nd turbine cascade from the leading edge of one blade to the leading edge of the next.

The predicted two-dimensional pressure and speed distributions of our potential flow model around the radial inflow 2nd turbine do not correlate well with the measured values. Steenkamp (1996) measured significant secondary three-dimensional flow patterns especially in the region between the 2nd turbine blades. This together with the fact that significant freestream turbulence levels are always present in turbo machinery would explain the poor predictions obtained from a potential flow model on the flow field through our torque converter's turbine. By and Lakshminarayana (1995) for example, concluded that a potential flow model could not accurately predict the static pressure distribution even at mid span of a torque converter turbine under all speed ratios since the flow was not irrotational. Their turbine was of the

mixed flow type. The results from this study correspond with their observation for the flow through a torque converter radial inflow or mixed flow turbine.

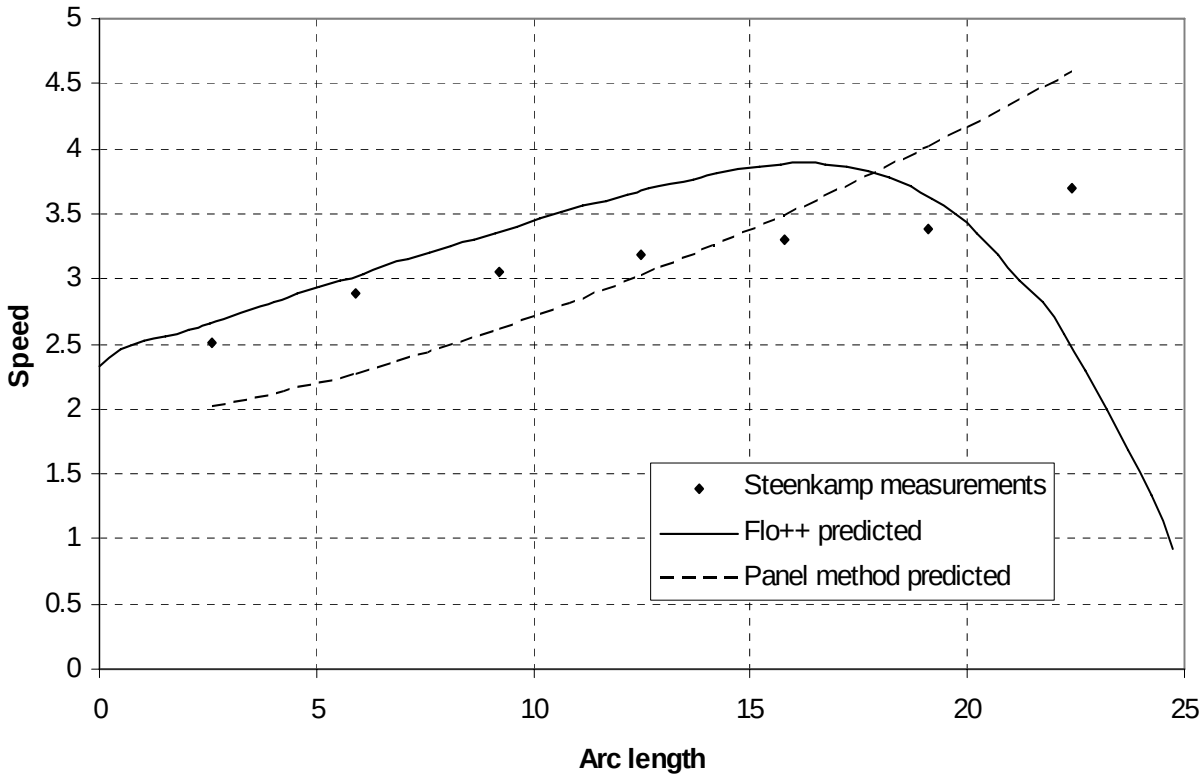

Figure 3-15. Speed distribution in the channel between two blades of the 2nd turbine cascade.

Cases have been reported though where the panel method was successfully employed to predict the pressure distribution on a blade row in a torque converter. These cases are for an axial flow stator blade row in an area where the geometry in the axial direction is two-dimensional. By and Mahoney (1989) as well as By and Lakshminarayana (1995) employed a three-dimensional potential flow method applied by means of the finite element method to compute the flow through a torque converter stator cascade. They concluded that a three-dimensional potential flow code could fairly well predict the two-dimensional static pressure distribution at the stator blade mid-span section since the flow is fairly irrotational there. Elsewhere the predicted pressure distribution on the blade surface was poor. By and Lakshminarayana (1991) used a two-dimensional panel method to predict the pressure distribution at the midspan of the stator in their test bed torque converter. They

achieved good correlation on the pressure surface except for the trailing edge region. Poorer agreement was achieved on the suction surface. It seems as if the validity of potential flow solutions to torque converters is restricted to two-dimensional axial cascades and should be used with caution.

3.9. Conclusion

Important conclusions drawn from this investigation are:

1. The two-dimensional potential panel method does not predict the pressure distribution on a blade of our radial inflow turbine accurately.
2. The two-dimensional panel method does not predict the flow distribution around our radial inflow turbine accurately.
3. The potential flow method can fairly accurately predict the flow through an axial flow stator where the geometry is strictly two-dimensional as stated in the literature.
4. The validity of potential flow solutions to torque converters is seemingly restricted to two-dimensional axial cascades and then only to the calculation of the pressure distribution at midspan of a stator in such a configuration where the flow is fairly irrotational.

Chapter 4

VISCOUS FLOW FIELD MODELLING: THE FINITE VOLUME METHOD

4.1 Introduction

In this chapter the finite volume method as embodied in the commercial CFD programme Flo++ 3.02 is used to calculate the viscous flow model flow field through the second turbine blade row of the torque converter outlined in appendix A. A two-dimensional flow field is used to predict the flow field and pressure distribution at mid span of a typical blade of the blade row. The predictions are compared with empirical data obtained by Venter (1993) and Steenkamp (1996). This consists of the pressure distribution on a typical second turbine blade and the velocity distribution in front of and between two consecutive turbine blades.

4.2 Governing equations

The governing equations used by Flo++ are given by the Flo++ manual as follows for the conservation of mass [equation (4-1)] and momentum [equation (4-2)]:

$$\frac{1}{\sqrt{g}}\frac{\partial}{\partial t}\left(\sqrt{g}\rho\right)+\frac{\partial}{\partial x_j}\left(\rho\,\tilde{u}_j\right)=s_m \tag{4-1}$$

$$\frac{\partial}{\partial t}\left(\rho u_i\right) + \frac{\partial}{\partial x_j}\left(\rho u_j u_i - \tau_{ij}\right) = \frac{\partial p}{\partial x_j} + s_i \tag{4-2}$$

The stress tensor τ_{ij}, for laminar flows is expressed as

$$\tau_{ij} = \mu s_{ij} - \frac{2}{3}\mu\frac{\partial u_k}{\partial x_k}\delta_{ij} \tag{4-3}$$

and for turbulent flows as

$$\tau_{ij} = \mu s_{ij} - \frac{2}{3}\mu\frac{\partial u_k}{\partial x_k}\delta_{ij} - \bar{\rho}\overline{u_i' u_j'} \tag{4-4}$$

The $'$ indicates the fluctuating component of the raw variable and the overbar denotes the averaging process. The rate-of-strain tensor s_{ij} is given by

$$s_{ij} = \frac{\partial u_i}{\partial x_j} + \frac{\partial u_j}{\partial x_i} \tag{4-5}$$

The source term s_m in the case of the continuity equation (4-1) may be used to represent the effect of mass injection. Mass injection serves the same purpose as that of an inlet boundary, i.e. introducing or extracting mass, momentum, or energy from the flow domain. In the case of the momentum equation (4-2), the source term s_i may be used to represent momentum forces not included in the equation. These may include buoyancy forces, rotational forces, and other user-defined sources.

When the governing equations are averaged to calculate turbulent flows, the so-called Reynolds stress $\overline{\rho u_i' u_j'}$ appears. Because the turbulent components of the velocities that appear in the Reynolds stress term cannot be computed directly, the Reynolds stress term must be modelled. In order to add turbulence conservation relations to the time-averaged continuity, momentum and energy equations, a relation for the turbulence kinetic energy *k* of the fluctuations was defined:

$$k \equiv \frac{\overline{u_i' u_i'}}{2} \tag{4-6}$$

Together with *k*, an additional turbulence parameter, turbulent dissipation, also appears in related equations. The turbulent dissipation is defined as:

$$\varepsilon \equiv -\nu \overline{\frac{\partial u_i'}{\partial x_j} \frac{\partial u_j'}{\partial x_i}} \tag{4-7}$$

These two turbulence parameters are successfully modelled by means of the commonly used *k*-ε model that gives good results in the absence of separated flow. This model is available for use in the Flo++ program. The model consists of two equations namely the turbulent kinetic energy equation and the dissipation equation. The turbulent kinetic energy equation as employed by Flo++ is

$$\frac{1}{\sqrt{g}}\frac{\partial}{\partial t}\left(\sqrt{g}\rho k\right)+\frac{\partial}{\partial x_j}\left(\rho\tilde{u}_j k-\frac{\mu_{\text{eff}}}{\sigma_k}\frac{\partial k}{\partial x_j}\right)= \tag{4-8}$$

$$\mu_t\left(S_s+S_b\right)-\frac{2}{3}\left(\mu_t\frac{\partial u_i}{\partial x_i}+\rho k\right)\frac{\partial u_i}{\partial x_i}-\rho\varepsilon$$

with

$$\mu_{\text{eff}}=\mu+\mu_t \tag{4-9}$$

$$\mu_t=f_\mu\frac{C_\mu\rho k^2}{\varepsilon} \tag{4-10}$$

$$S_b=-\frac{g_i}{\sigma_{h,t}}\frac{1}{\rho}\frac{\partial\rho}{\partial x_i} \tag{4-11}$$

$$S_s=s_{ij}\frac{\partial u_{\text{i}}}{\partial x_{\text{j}}} \tag{4-12}$$

The turbulence dissipation equation employed in Flo++ is

$$\frac{1}{\sqrt{g}}\frac{\partial}{\partial t}\left(\sqrt{g}\rho\varepsilon\right)+\frac{\partial}{\partial x_j}\left(\rho\tilde{u}_j\varepsilon-\frac{\mu_{\text{eff}}}{\sigma_\varepsilon}\frac{\partial\varepsilon}{\partial x_j}\right)= \tag{4-13}$$

$$C_1\frac{\varepsilon}{k}\left[\mu_t\left(S_s+C_3S_b\right)-\frac{2}{3}\left(\mu_t\frac{\partial u_i}{\partial x_i}+\rho k\right)\frac{\partial u_i}{\partial x_i}\right]-C_2\rho\frac{\varepsilon^2}{k}-C_4\rho\varepsilon\frac{\partial u_i}{\partial x_i}$$

The modelling constants are:

C_μ	σ_k	σ_ε	C_1	C_2	C_3	C_4	κ	E	f_μ
0.09	1.0	1.22	1.44	1.92	1.44	-0.33	0.42	9.0	1.0

Venter (1993) reports that no flow regions where boundary layer seperation occur are noticeable in the stalled state in the second turbine blade row. Therefore the *k*-ε model will be used in the viscous flow calculations that is done with Flo++.

Furthermore, wall functions can be used to model the direct influence of the wall on the viscous flow field. This avoids the problem of solving through the laminar sub-layer to the wall in order to calculate the direct influence of viscosity. Between 10 and 30 grid points would otherwise have been required to resolve this layer accurately. The wall functions employed to circumvent this problem relies on empirical data gleaned from viscous fluid flow over a flat plate. Flo++

approximates the boundary layer by employing two wall functions namely the viscous sub-layer and the log-law layer. The transition between the two layers are at $y^+ = 11.63$ which is modelled from empirical data obtained from flat plate flows. Here, $y^+ = yv^*/\nu$ is a dimensionless sub-layer variable where $v^* = (\tau_w/\rho_w)^{1/2}$, the wall-friction velocity.

4.3 Parameters influencing the pressure distribution over a turbine blade.

Dimensional analysis indicates that the dimensionless pressure distribution C_p on a turbine blade will depend on the Reynolds number *Re*, the freestream turbulence level *I*, the dimensionless distance from the leading edge *x/c* and the angle of attack α:

$$C_p = f\left(Re, I, \frac{x}{c}, \alpha\right) \tag{4-14}$$

where *x* is the distance from the leading edge and *c* is the chord length. According to empirical results obtained by Venter (1993) the pressure distribution is relatively independent of the Reynolds number at the torque converter's stall condition. The available empirical data are obtained only for the angle of attack at the stalled condition. This reduces the number of independent variables for this specific case to the freestream turbulence level and the dimensionless distance from the leading edge:

$$C_p = C_p\left(I, \frac{x}{c}\right) \tag{4-15}$$

Due to the reported freestream turbulence levels in the region of 5% or more in turbomachinery the freestream turbulence levels specified at the inlet boundary were varied between 0% and 15% to test its influence on the dimensionless pressure distribution C_p.

In order to compare the pressure distribution results obtained from CFD with the empirical data obtained by Venter (1993) his relation between C_p and the stagnation pressure P_{stag} and reference pressure P_{ref} is used:

$$C_p = \frac{P_{surf} - P_{ref}}{P_{stag} - P_{ref}} \tag{4-16}$$

Venter (1993) took the reference pressure P_{ref} at the wall at the inlet of the 2nd turbine blade row halfway between two consecutive turbine blades. The procedure for determining C_p from the predicted pressure field entails solving for P_{ref} and P_{stag} and substituting the solutions into equation (4-16). Then C_p can be computed along the surface of the blade by substituting the surface pressures P_{surf} into equation (4-16).

4.4 Computational grids

Figure (4-1) shows the computational grid. The grid points are clustered at regions where high pressure and velocity gradients are expected. These are near the nose and in the passage between two blades. A relatively course grid is used in the region of the stator upstream of the turbine. Table (4-1) shows the grid spacing.

In the initial development of the grid, the inlet region between the inlet boundary and the leading edge region of the turbine blades were modelled without stator blades or flat plates. The measured inlet reference flow angle identified and measured by Venter (1993) as 54.3 degrees is one of the parameters with which the calculated results are compared. Without the stator blades or any other means of directing the inlet flow, the maximum predicted reference angle was 41 degrees. This indicated that the presence of the stator just upstream of the turbine might play an important role in the flow field at the inlet of the turbine and because of that, through the turbine too. The purpose of the stator blades in this case are to smoothly and efficiently change the direction of the flow received at the stator entrance and discharge it in the right direction at the turbine entrance. In our grid the flow direction at the inlet boundary can already be specified in the desired direction, thereby obviating the need for carefully contoured turbine blades. The stator was therefore simply simulated by two or three flat plates. It was found that there was no discernible difference in the flow field through the

turbine when either of the two flat plate arrangements was utilised. The only purpose of the flat plates was to discharge the flow at the estimated stator outlet direction at the stator outlet position on the grid. This angle was estimated at 63.3-degrees by means of the Ainley and Mathieson method for flows below half the speed of sound as described by Dixon (1978). This simplified arrangement saves considerable grid generation effort and computer calculation time.

The inlet region also serves to separate the flow region surrounding the turbine blades in which we are interested as far as possible from the inlet boundary. It is difficult to achieve in an internal flow field like this. Lakshminaryana (1996) advised that inlet and outlet boundaries should be separated from the flow region under study by at least one cord length.

Behind the exit of the stator simulation region, a separate rectangular region is constructed and attached to the stator simulation region. By specifying this separate region it is possible to do grid refinement in this critical region of expected high gradients and flow turning without affecting the less critical grid around the flat plates simulating the stator influences. Furthermore, a far less distorted grid between the stator outlet and the turbine inlet was made possible by this technique compared with just a simple extension of the stator region grid right up to the leading edges of the turbine blades. This arrangement improves the computational accuracy in this region.

Cyclic boundaries are specified on both the stator region and the region between the stator outlet and the turbine inlet. The number of stator blades is not an integer multiple of the number of turbine blades. This implies that the sector upstream of two consecutive turbine blades does not have the same stator blade arrangement as the next such sector. Hence, although the sector of the grid containing the turbine passage is axially symmetric, the extension of that sector in the upstream direction that includes the stator blades is not axially symmetric. If the flow field of the stator blades had to be included in the analysis, a ninety degree sector of the stator and 2^{nd} turbine blade rows had to be included in the grid to obtain overall

axial symmetry. Such an arrangement would have been necessary to enable the use of cyclic boundary conditions on the lateral fluid boundaries. This requirement highlights another advantage of simulating the stator blades with a simple flat plate arrangement. The flat plates in the sector upstream of the single turbine channel in the grid of figure (4-1) can now be arranged to enable the use of cyclic boundary conditions on the lateral sides of the inlet region too. To obtain cyclic symmetry, the flat plates in the stator section are placed equal distances apart.

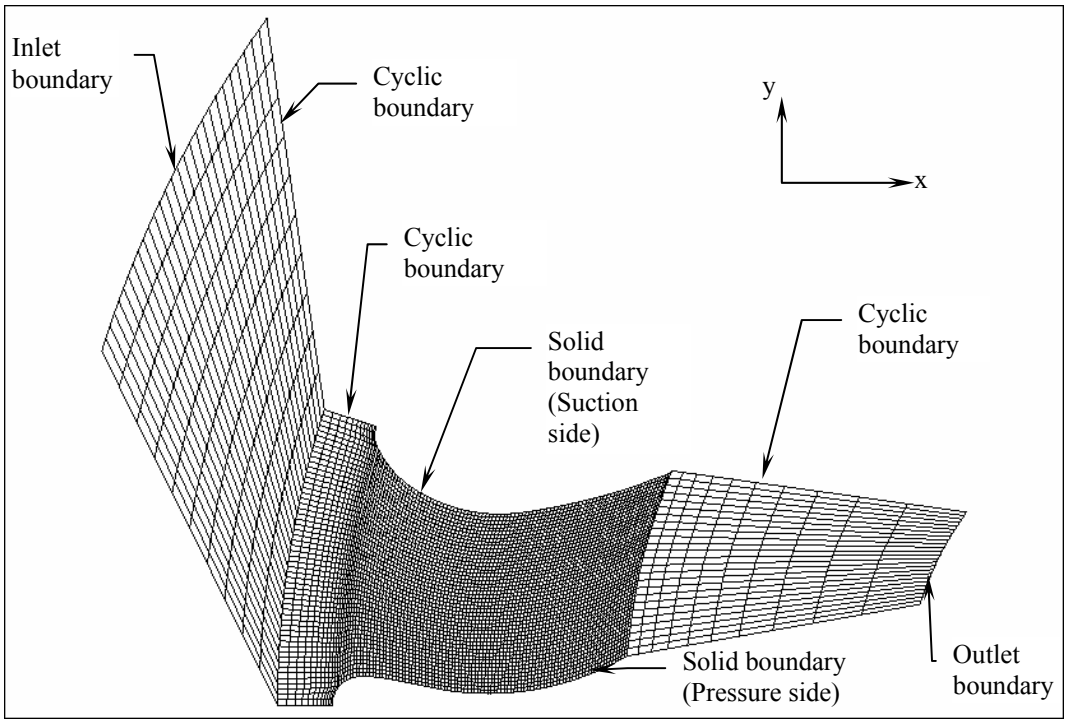

Figure 4-1. Computational grid.

Region	Cells in x-direction	Cells in y-direction
Stator	10	28
Between stator exit and turbine inlet	12	56
Passage between two turbine blades	90	56
Behind the turbine blades	10	28

Table 4-1. Grid size.

The passage between the suction side and compression side of two adjacent turbine blades has a very fine and almost orthogonal grid. This grid is attached to the outlet grid behind the turbine blade row. The outlet grid has been made much coarser than that of the preceding region because we are not interested in the flow through this region. It only serves to dampen the influence of the specified outlet boundary flow field properties on the flow field region under scrutiny. The outlet boundary is specified at the tail end of this last region as shown in figure (4-1).

4.5 Boundary conditions

Several types of boundaries are used in this analysis. These are inlet boundaries, outlet boundaries, solid walls and symmetrical boundaries. The specification of the conditions at the inlet boundary needs special attention due to the many different parameters that have to be specified there. On the other boundaries, except for the outlet boundary, no special specifications are needed. The only specification placed on the outlet boundary is that of a constant pressure distribution. The distance between this boundary and the region of interest dampens any inaccuracy that is involved in this approximating specification.

4.5.1 Inlet boundary

The distributions of all variables apart from pressure are prescribed directly at the centres of the faces on this boundary. These variables are the three velocity components, density, temperature, turbulent kinetic energy k and the dissipation rate ε. For the high Reynolds number turbulence model used in this analysis, care must be taken to prescribe realistic values of the turbulent kinetic energy and dissipation rate. They must be scaled correctly with the speed at the inlet boundary. These values are scaled by means of the definitions for turbulence level I as well as ε.

The freestream turbulence level I is defined as:

$$I \equiv \frac{1}{U}\left[\frac{1}{3}\left(\overline{u'^2} + \overline{v'^2} + \overline{w'^2}\right)\right]^{1/2} \tag{4-17}$$

or

$$I^2U^2 = \frac{1}{3}\left(\overline{u'^2} + \overline{v'^2} + \overline{w'^2}\right) \tag{4-18}$$

where U is the mean freestream velocity and u', v' and w' are the fluctuating velocities in the freestream. The term $\overline{u'^2}$ is the mean square fluctuations averaged over a long period of time:

$$\overline{u'^2} = \frac{1}{T}\int_{t_0}^{t_0+T} u'^2 dt \tag{4-19}$$

where T is large compared to the relevant period of the fluctuations. Substituting equation (4-18) into equation (4-6) yields a relationship between k and I from which a proper value of k can be computed for the inlet boundary:

$$k = \frac{3}{2}I^2U^2 \tag{4-20}$$

In order to derive a relation for the computation of ε it should be noted that the turbulent viscosity is linked to k and ε via

$$\mu_t = f_\mu \frac{C_\mu \rho k^2}{\varepsilon} \tag{4-21}$$

and to k and l via

$$\mu_t = f_\mu C_\mu^{1/4} \rho k^{1/2} l \tag{4-22}$$

By equating equations (4-21) and (4-22) an expression relating k, ε and l can be obtained. Hence,

$$\varepsilon = C_\mu^{3/4} \frac{k^{3/2}}{l} \tag{4-23}$$

From equation (4-23) ε can be computed from k and a prescription of the turbulence length scale l. A plausible value for l can be obtained from the literature (Schlichting, 1979) or, failing that, estimated. A length scale of at least an order of magnitude smaller than half the channel width for fully developed channel flow is a realistic estimation [White (1991)]. Here the channel width was estimated as 20mm, which is approximately the width between two consecutive

flat plates at the inlet boundary. The length scale was therefore taken as 0.9mm. The flow at the inlet boundary then essentially approximates fully developed channel flow between the flat plates used in the inlet region.

4.6 Results

The pressure distribution was tested against the empirical data of Venter (1993) for inlet boundary freestream vorticity levels of 0%, 5%, 10% and 15% on an older program, PHOENICS 1.4, which solves the governing fluid flow equations in a similar way as Flo++. The test was done with three flat plates in the inlet region in place of the stator. The results are depicted in figure (4-2). The results differed mainly on the suction side towards the last 80% of the chord length. To highlight the differences, the scale of the abscissa was enlarged. There is a variation in the predicted pressure distribution for inlet boundary freestream vorticity levels varying between 0%, 5% and 10%. For inlet boundary freestream vorticity levels above 10 % the variations in the predicted pressure distribution are negligible. The results of the inlet boundary freestream vorticity levels above 10% also approximated the experimental measurement data of Venter (1993) the closest. Hence the inlet boundary freestream turbulence level was set at 15%. This setting corresponds with measured freestream turbulence levels in the literature. Bahr, et. al. (1990), for instance, reported measured flow-averaged turbulence levels in the range of 10% to 25% in the vicinity of their torque converter's stator. The velocity distribution for the 15% case is shown in figure (4-3).

The complete pressure distribution for an inlet boundary freestream vorticity specification of 15% is depicted in figures (4-4) and (4-5). It very closely predicts the measured values of Venter (1993). The reference velocity angle for this case is 55.4 degrees which is 1.1 degree more than the measured 54.3 degrees. This constitutes an error of 2%. The positions of the predicted and measured stagnation points also coincide very well. The streamline between two turbine blades is depicted in figure (4-6).

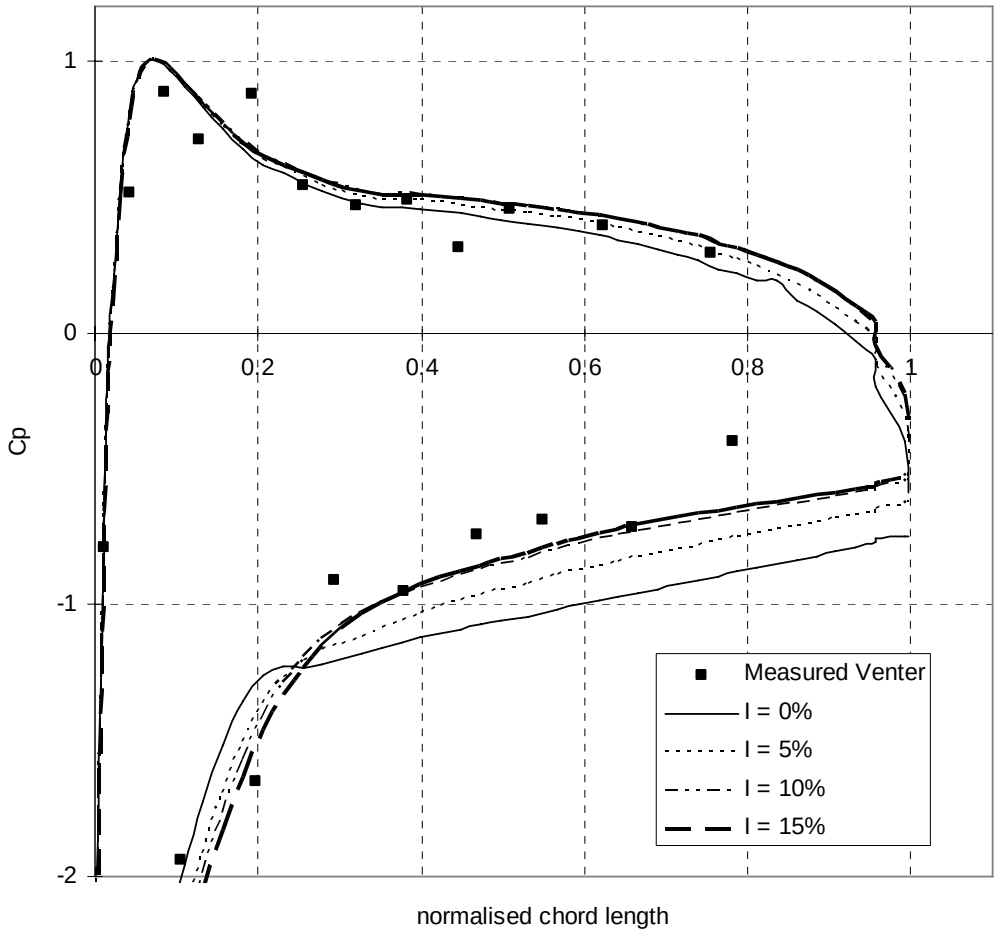

Figure 4-2. Pressure distribution for various inlet boundary freestream turbulence levels.

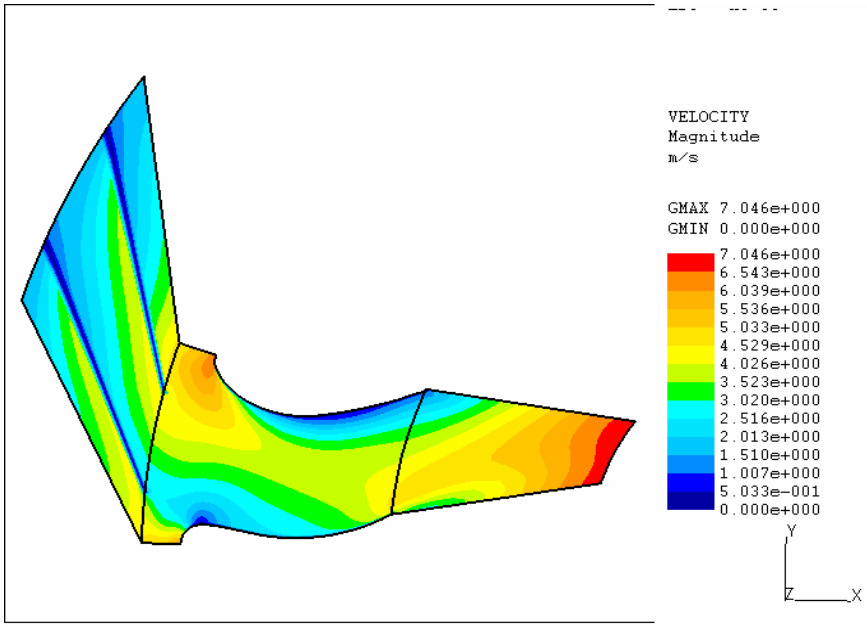

Figure 4-3. Velocity distribution for inlet boundary freestream turbulence level of 15%.

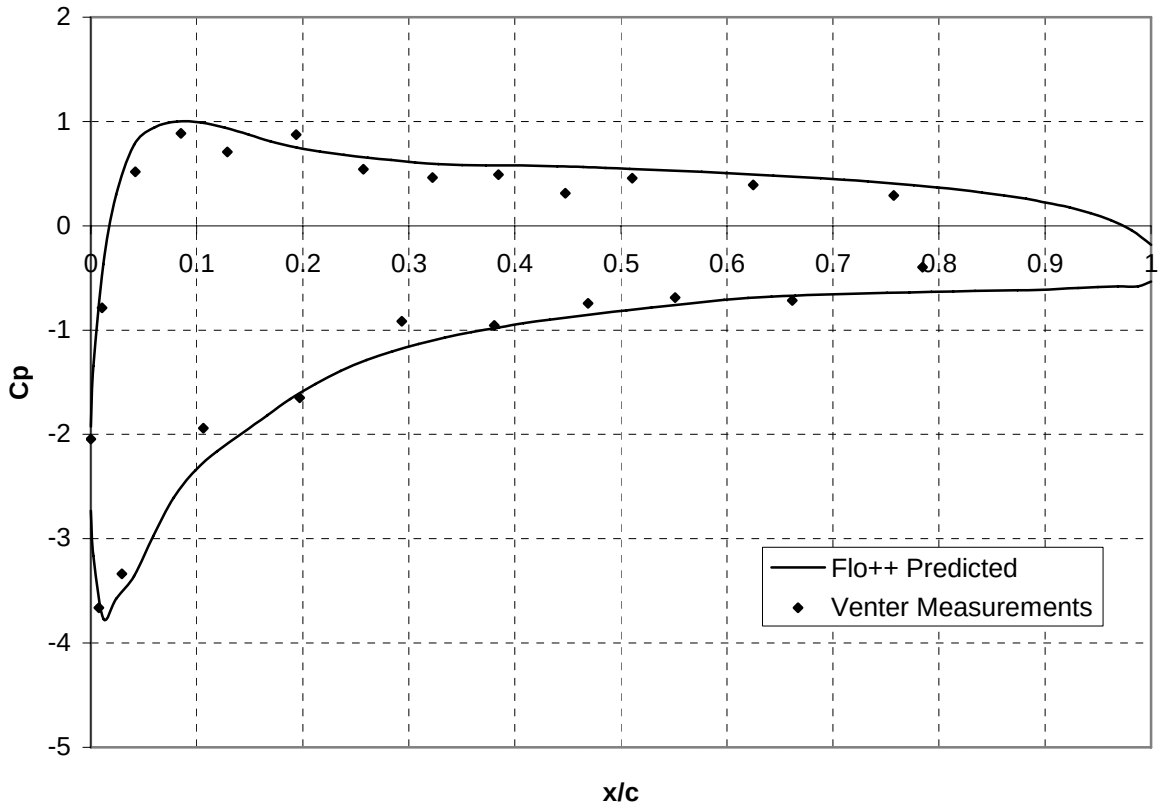

Figure 4-4. Dimensionless pressure distribution for a 15% inlet boundary freestream turbulence level.

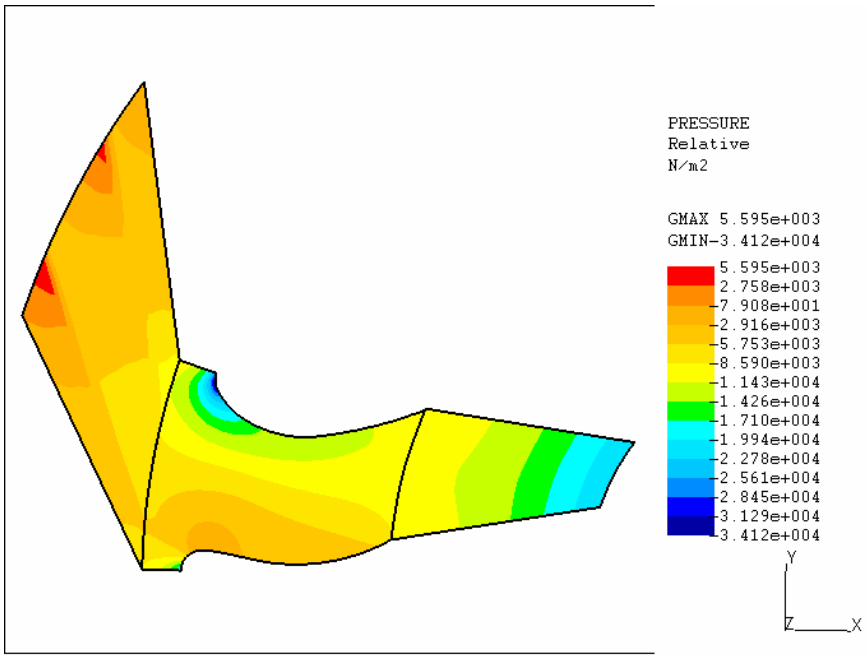

Figure 4-5. Pressure distribution for inlet boundary freestream turbulence level of 15%.

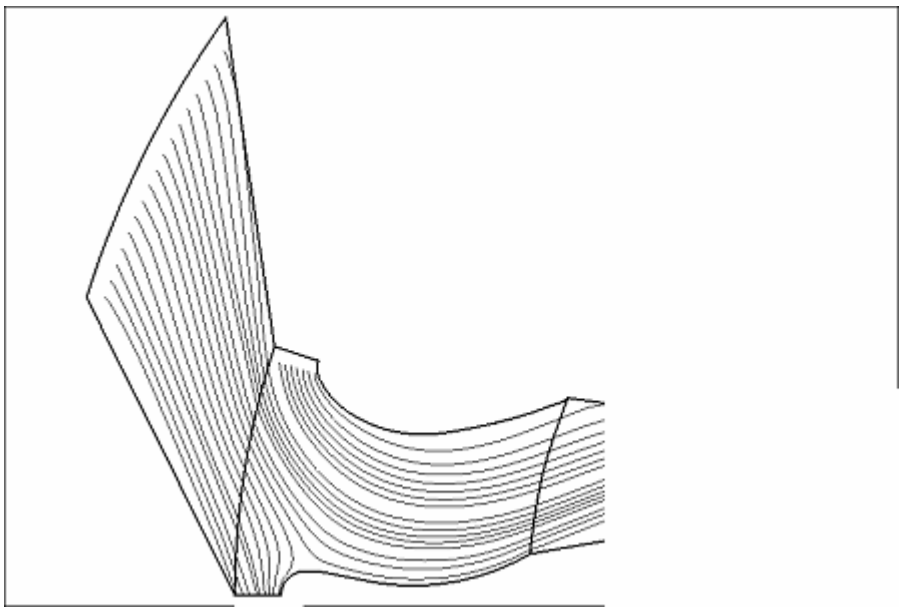

Figure 4-6. Streamlines between two turbine blades.

In figure (4-7) the Flo++ predicted speed distribution in front of the 2nd turbine cascade is compared with the measured speed distribution of Steenkamp (1996).

A description of the position of the speed distribution is given in chapter 3. The predicted values correlate poorly with the measured values though. Also included in the comparison is the predicted speed distribution by the panel method as implemented by Abreast. The patterns of the predicted speed distribution are similar but slightly displaced. This may be due to differences in the predicted direction of the flow in front of the turbine cascade. This may be caused by the different models used to include the influence of the stator on the flow at the entrance of the turbine. The panel method utilised the actual stator blades while the grid in the viscous flow model utilised flat plates to simulate the influence of the stator.

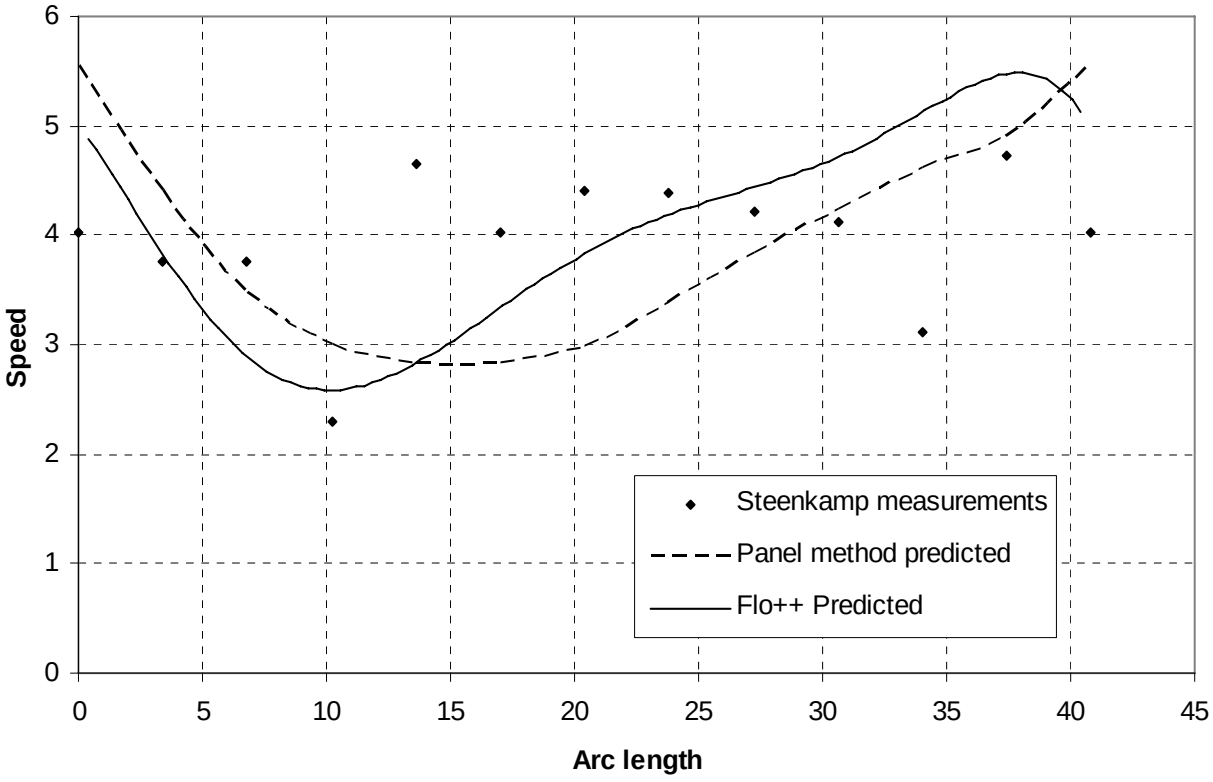

Figure 4-7. Speed distribution in front of the 2nd turbine cascade from the leading edge of one blade to the leading edge of the next.

The Flo++ predicted speed distribution through the channel between two consecutive turbine blades is compared with the measured speed distribution of Steenkamp (1996) in figure (4-8). A description of the position of the speed

distribution through the channel is given in chapter 3. The speed as predicted by the viscous flow model diminishes sharply towards the suction surface of the channel. The suction surface lies at the high-end of the arc on which the speed measurements are taken. The measured speed values do not indicate this sharp decline in speed though. This may be due to the interference of the measuring probe in the flow field near the suction surface. Towards the pressure surface, at the low end of the arc in figure (4-8), excellent correlation between measured speed and the speed predicted by the viscous flow model is obtained.

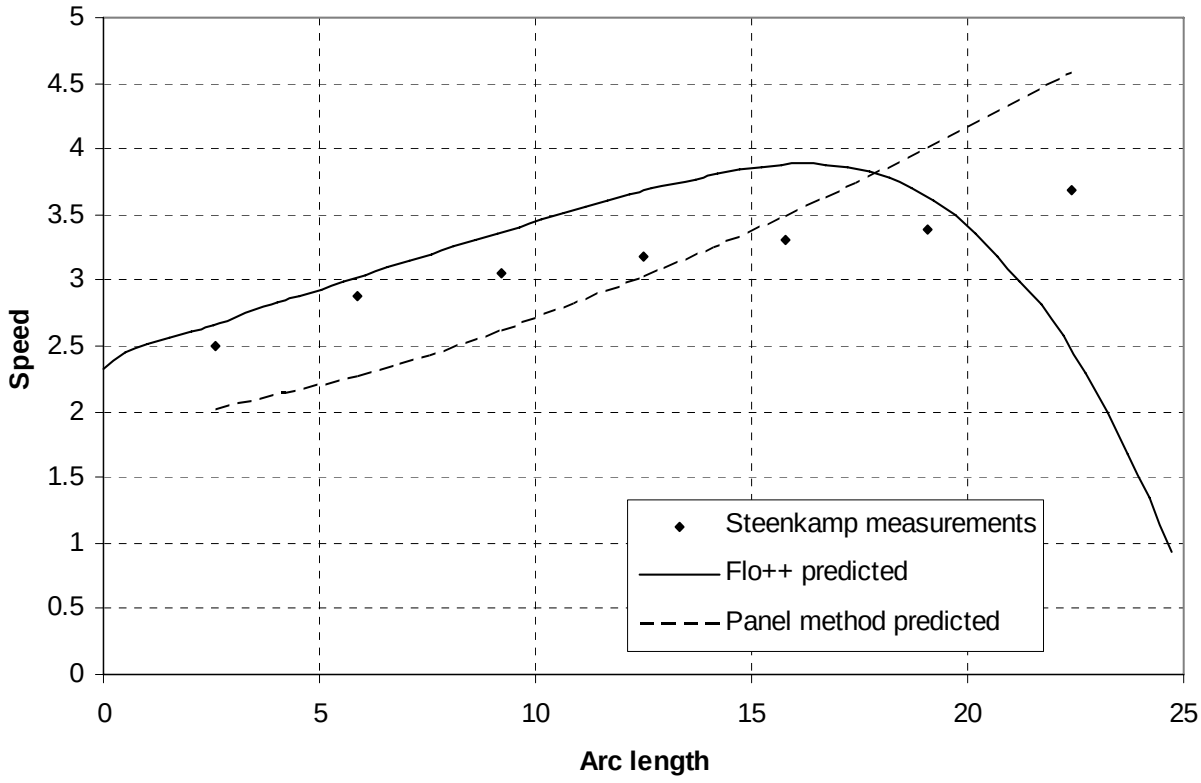

Figure 4-8. Speed distribution in the channel between two blades of the 2nd turbine cascade.

4.7 Conclusions

The following conclusions can be drawn regarding the 2nd turbine of our torque converter in the stall condition:

1. The two-dimensional viscous flow model with the high-speed k-ε-viscosity model predicted the pressure distribution at midspan of a typical blade of the radial inflow 2nd turbine to a high degree of accuracy. This is where the hub and shroud geometry is almost two-dimensional in the radial direction. It also predicted the reference velocity angle at the inlet of the blade row accurately.
2. Care has to be taken to specify realistic values for k and ε at the inlet boundary. A Freestream turbulence level of 15% works well.
3. Furthermore, care must also be taken to ensure that the numerical model's flow field at the entrance of the 2nd turbine blade row accurately resembles the real flow field. This can be done economically by estimating the outlet flow angle of the preceding blade row by means of, for example Ainley and Mathieson's technique and then modelling the preceding blade row by means of flat plates placed at the predicted outlet angle. The flat plates should be made as long as possible in order to take the inlet boundary as far away as possible from the flow field around the blade row under scrutiny. The flat plates must however end at the same distance away from the inlet of the 2nd turbine blade row as the real model's preceding blade row exit.
4. A fairly good prediction of the speed values in the channel between two blade rows was obtained.

Chapter 5

CONCLUSIONS

In this project the flow through the stationary 2nd turbine blade row of a torque converter in the stall condition is analysed by means of a potential flow panel method and a viscous flow model. The geometry of the hub and shroud surrounding the blade row is highly two-dimensional in the radial direction. The preceding stator blade row is modelled in a radial inflow freestream. This differs from Venter's (1993) panel method where a free spiral vortex is used to simulate the spiral flow caused by the preceding stator blade row that was not included in that simulation. The advantage of including the preceding stator blade row in the simulation is that the necessity to specify the strength of the free spiral vortex that has to be known a priori in Venter's case is eliminated. Only the strength of the radial inflow freestream needs to be specified in our case. In the case of the potential flow model, it does not matter what the strength of the inflow freestream is because the Reynolds number does not enter the analysis. In the case of the viscous flow model the strength of the inflow freestream can be specified according to the desired Reynolds number.

It was found that for the 2nd turbine blade row at midspan:

1. Our panel method predicts the pressure distribution on a typical blade poorly.
2. Our panel method predicts the velocity distribution in the flow field poorly.
3. Our panel method predicts the direction of the reference velocity at the entrance of the blade row accurately.
4. The most successful application of potential flow models was when the model was applied by means of a three dimensional finite element method in an axial flow field. Accurate predictions were obtained only at midspan of a stationary stator blade row.
5. The viscous flow model predicts the pressure distribution at midspan on a typical blade of a stationary turbine blade row accurately.

6. The viscous flow model predicts the direction of the reference velocity at the entrance of the stationary blade row accurately.
7. The viscous flow model's predicted flow velocities at midspan between the blades of the stationary turbine blade row correlate well with the measured values considering the potential errors of the measured values near the suction side.
8. It is necessary to take the preceding blade row into account to ensure the accurate calculation of the flow field near the entrance of the blade row under observation. Modelling the blades of the preceding blade row with flat plates placed in the estimated outlet direction simplifies the grid and consequently reduces the computer CPU-time necessary to arrive at a satisfactorily converged solution for the viscous flow model.
9. Care must be taken to specify realistic values for k and ε at the inlet boundary. A freestream turbulence level of 15% at the inlet boundary of the viscous flow model accomplishes this.

References

Anderson, J.D., 1991, *Fundamentals of aerodynamics*, 2nd edition, McGraw Hill.

Bahr, H. M., Flack, R. D., By, R. R. and Zhang, J. J., 1990, *Laser velocimeter measurements in the stator of a torque converter*, SAE Paper No. 901769.

Brun, K., Flack, R.D. and Gruver, J.K., 1996, *Laser velocimeter measurements in the pump of an automotive torque converter: Part 2 – unsteady measurements*, Journal of Turbomachinery, Vol. 118, Julie.

By, R.R., Kunz, R. and Lakshminarayana, B., 1995, *Navier-Stokes analysis of the pump flow field of an Automotive Torque Converter*, Journal of Fluids Engineering, Vol. 117.

By, R.R. and Lakshminarayana, B., 1991, *Static pressure measurements in a torque converter stator*, SAE Paper no. 911934.

By, R.R. and Lakshminarayana, B., 1995, *Measurement and analysis of static pressure field in a torque converter pump*, Journal of Fluids Engineering, Vol. 117, pp. 109 - 115.

By, R.R. and Mahoney, J.E., 1989, *Technology needs for the automotive torque converter – Part 1: Internal flow, blade design and performance*, SAE paper no. 880482.

Dixon, S.L., 1978, *Fluid mechanics and thermodynamics of turbomachinery*, Pergamon Press, Oxford, 3rd ed.

Eksergiian, R., 1943, *Fluid torque converter and coupling*, Journal of Franklin Institute, Vol. 235, No. 5, pp. 441-478.

Frederick, D., and Chang, T.S., 1972, *Continuum mechanics*, Scientific Publishers, Boston

Groiss, F.H., 1991, *An anlysis of hydrodynamic torque converters for design applications in heavy vehicles*, MSc thesis, Rand Arfikaans University.

Gruver, J. K., Flack, R. D. and Brun, K., 1996, *Laser velocimeter measurements in the pump of an automotive torque converter: Part 1 – average measurements*, Journal of Turbomachinery Vol. 118, pp. 562 – 569.

Hess, J.L. and Smith, A.M.O., 1966, *Calculation of potential flow about arbitrary bodies, Progress in Aeronautical Sciences*, Vol. 8.

Hirch, C., 1988, *Numerical computation of internal and external flow*s, *Vol.1*, John Wiley.

Ishihara, T. and Emori, R.I., 1966, *Torque converter as a vibrator damper and its transient characteristics*, SAE Paper 660368.

Jandasek, V.J., 1963, *The design of a single stage three-element torque converter*, Passenger Car Automatic Transmissions, SAE Transmission Workshop Meeting, 2nd Edition, Advanced Engineering, Volume. 5, p 201.

Kotwicki, A.J., 1982, *Dynamic models for torque converter equipped vehicles*, SAE Paper 820393.

Lamprecht, J., 1983, *Die ontwerp van 'n hidroulise wringomsetter*, MSc thesis, University of Pretoria.

Lakshminarayana, B., 1996, *Fluid dynamics and heat transfer of turbomachinery*, John Wiley & Sons, New York.

Marathe, B. V., Lakshminarayana, B., and Dong, Y., 1996, *Experimental and numerical investigation of stator exit flow field of an automotive torque converter*, Journal of Turbomachinery, Vol. 118, pp. 835-843801.

Moran, Jack, 1984, *An introduction to theoretical and computational aerodynamics*, John Wiley & Sons.

Reynaud, F.P., 1991, *Hydrodynamic modelling of torque converters*, M.Eng. thesis, University of Stellenbosch.

Richardson, L.F., 1922, *Weather prediction by numerical process*, Cambridge University Press.

Rodi, W., 1980, *Turbulence models and their applications in hydraulics*, IAHR, Netherlands.

Salas, S.L., Hille, E. and Ettgen, G.J., 2002, *Calculus, one and several variables*, 9th edition, John Wiley & Sons.

Schlichting, H., 1979, *Boundary-layer theory*, McGraw-Hill, VSA.

Schulz, H., Greim, R., and Volgmann, W., 1996, *Calculation of three-dimensional viscous flow in hydrodynamic torque converters*, Journal of Turbomachinery, Vol. 118.

Sinclair, P.M., 1986, *An exact integral (field panel) method for the calculation of two-dimensional transonic potential flow around complex configurations*, Aeronautical Journal, Vol. 90.

Smith, A. M. O. and Gamberoni, N., 1956, *Transition, pressure gradient and stability theory*, Douglas Aircraft Report ES-26388 [see alos Proc. Ninth Internat. Cong. Appl. Mech., vol. 4, pp. 234-244 (1957)].

Steenkamp, M., 1996, *Die meet van die snelheidsprofiele in die turbine van 'n koppelomsitter*, B.Eng project, University of Stellenbosch.

Strachan, P.J., Reynaud, F.P. and Von Backström, T.W., 1992, *The hydrodynamic modelling of torque converters*, N&O Joernaal, April.

Spannhake, E.W., 1949, *Hydrodynamics of the hydraulic torque converter*, SAE Summer Meeting, June, French Lick, Inc.

Van der Merwe, J.C., Von Backström, T.W. and Harms, T.M., 1996, *Flow calculation through a torque converter turbine*. Presented at the SACAM96 Conference, Gauteng S.A., July 1996.

Venter, A A, 1993, *The flow around torque converter turbine blades*, M.Eng. thesis, University of Stellenbosch.

Von Backström, T.W. and Lakshminarayana, B., 1996, *Perspective: fluid dynamics and performance of automotive torque converters: an assessment*, Journal of Fluids Engineering, Vol. 118, pp. 665 – 678.

White, F M, 1991, *Viscous fluid flow*, second edition, Mcgraw-Hill, VSA.

Wislicenus,G F, 1965, *Fluid mechanics of turbomachinery*, second ed., Dover Publications, New York.

Xia, H and Oh, P., 1999, *A dynamic model for automotive torque converters*, Int. J. Vehicle Design, Vol. 21, Nos 4/5 (Special Issue), pp. 344-354.

Appendix A

THE EXPERIMENTAL TORQUE CONVERTER

The experimental torque converter on which Reynaud (1991), Venter (1993) and Steenkamp (1996) made flow measurements is an adapted full-scale model of a commercial torque converter, the Renk MS 80 0,85. The experimental unit is manufactured from yellow copper and aluminium. A modified Perspex cover covers the turbine side. The turbines and stator of the experimental unit are fixed in order to facilitate the making of the pressure and velocity measurements. The experimental unit therefore simulates a commercial torque converter in the stalled state.

Figures (A-1) and (A-2) shows that the experimental unit consists of a centrifugal pump that discharges into an inflow turbine blade row, followed by an inflow stator blade row and a second inflow turbine blade row. The first turbine consists of 50 blades, the stator has 48 blades and the second turbine has 20 blades. These three blade rows are almost axially symmetrical. Only the channel thickness at the outlet of the second turbine varies significantly, which makes it the only element which is not entirely axial symmetric. Figure (A-3) is a photograph of the torque converter turbines and stator that appears in the drawing of figure (A-2).

Holes were drilled through the Perspex cover on the turbine side to give the measuring probes access to the flow channel in the vicinity of the second turbine blade row. The Perspex cover allows easy observation of the flow channel through the two turbine blade rows and the stator blade row. In order to carry out the experiments, water instead of oil was used. Reynaud (1991) explains the recommendation to use water. The two main reasons for using water instead of oil are that water has a lower viscosity than the oil that is used in the commercial torque converter. Dimensional analysis shows that lower speeds and less power are required to maintain the dynamic similarities between the water filled experimental unit and the oil filled commercial torque converter. Secondly, water improves the observation of the flow through the stator and turbines and as such facilitates the pressure and velocity measurements.

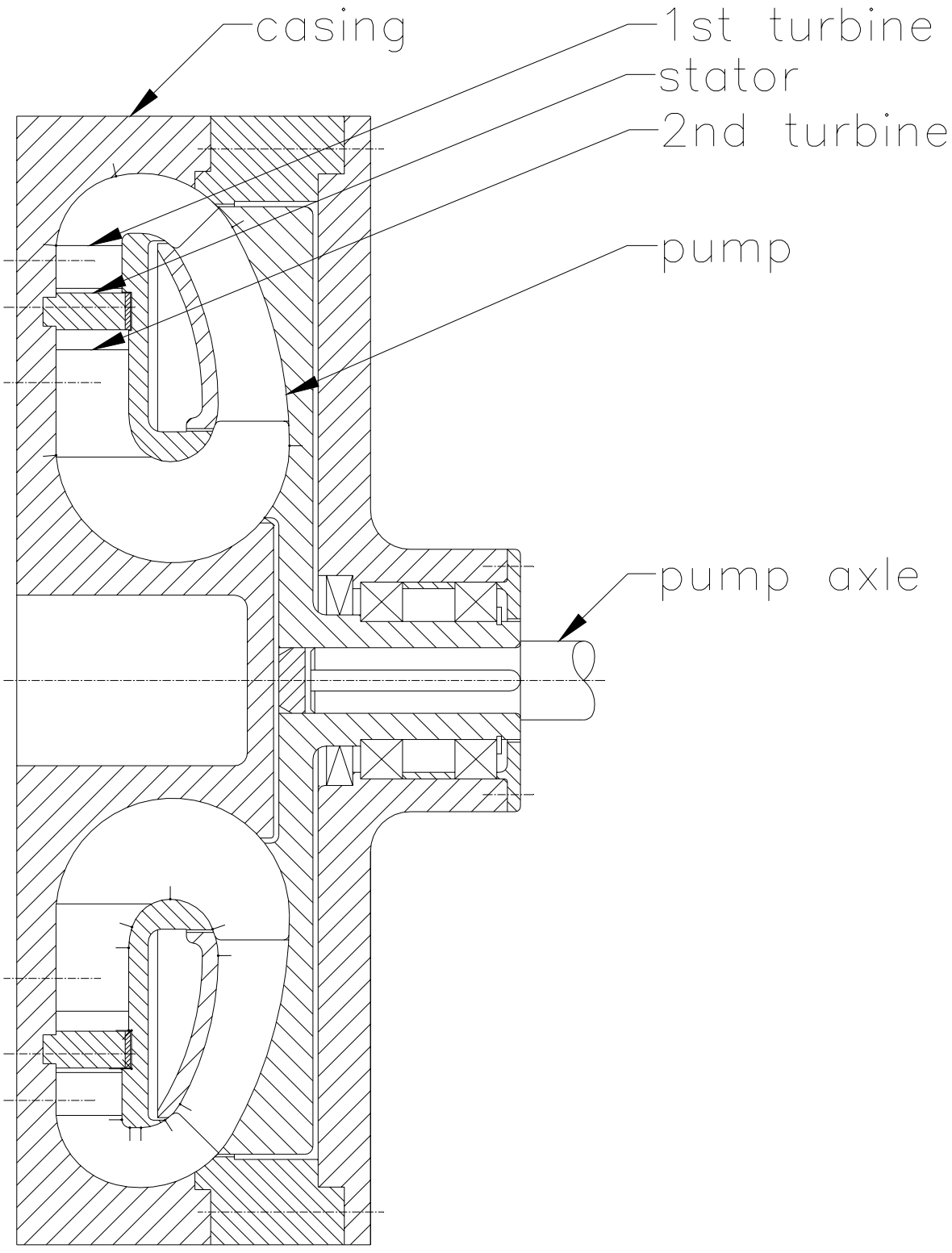

Figure A-1. Cross section of the experimental torque converter.

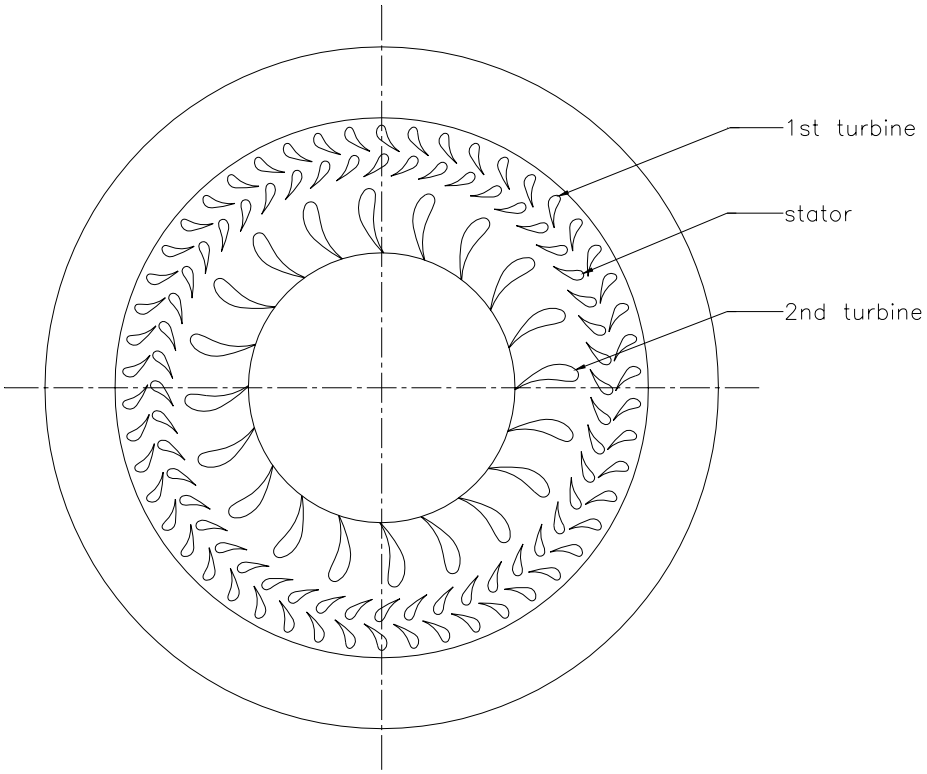

Figure A-2. Plan view of the turbine and stator side of the experimental torque converter.

Figure A-3. Plan view photograph of the turbine and stator side of the experimental torque converter.

Appendix B

DERIVATION OF THE PARABOLIC VORTICITY DISTRIBUTION

Every quadratic equation as expressed by

$$y = ax^2 + bx + c \tag{B-1}$$

symbolize a parabola. See for instance Salas et. al. (2002). It can be shown that equation (B-1) has two roots:

$$x_{1,2} = \frac{-b \pm \sqrt{b^2 - 4ac}}{2a} \tag{B-2}$$

Figure (B-1) depicts the vortex strength distribution along the surface coordinate s of an airfoil in a freestream. It is zero at the tail when approached both from the upper surface as well as the lower surface. Its maximum strength is in the region of the

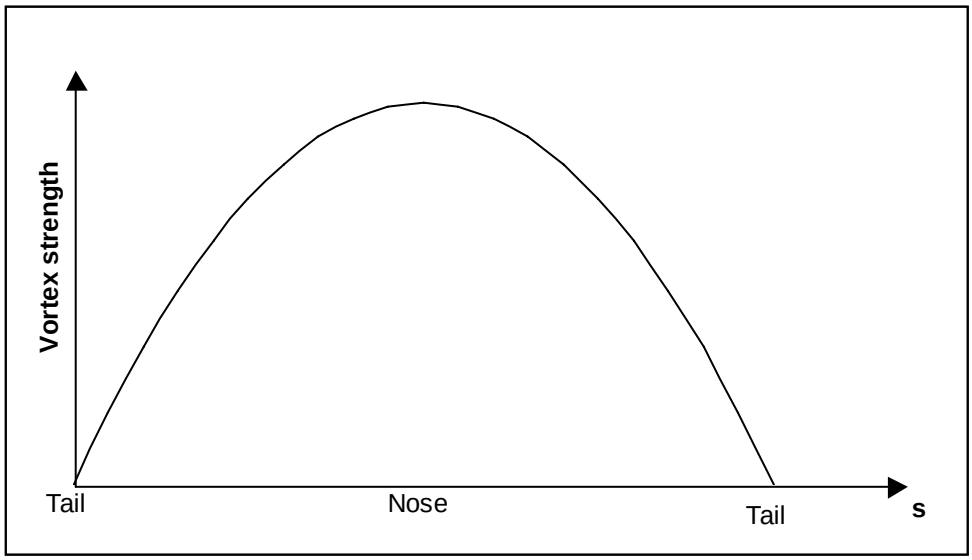

Figure B-1. Parabolic vorticity strength distribution along the surface coordinate s of an airfoil.

nose.

Let the length of the surface be *S*. Then, because the vortex strength, $\gamma(s)$, is zero at the tail, equation (B-1) will have roots at 0 and *S* if it is used to compute the vortex strength distribution along the surface of the body. In that case equation (B-1) becomes:

$$\gamma(s) = as^2 + bs + c \tag{B-3}$$

For the two roots equation (B-2) becomes

$$\frac{-b \pm \sqrt{b^2 - 4ac}}{2a} = 0, S \tag{B-4}$$

For the case where the root is at the origin, equation (B-4) yields:

$4ac = 0$ or $c = 0$ because $a \neq 0$ to prevent division by 0. (B-5)

Substituting this result into equation (B-4) and analysing it for the case where the root is at *S* yields:

$$\frac{-b \pm \sqrt{b^2}}{2a} = S \text{ or} \tag{B-6}$$

$b = -aS$

Substituting the results of equations (B-5) and (B-6) into equation (B-3) yields:

$$\gamma(s) = as^2 - aSs \tag{B-7}$$

By definition, the strength of the vortex is the circulation calculated along a closed curve surrounding the vortex. Hence, the circulation calculated along a closed curve surrounding the body must be the sum of the strengths of all the vortices specified on the surface of that body.

$$\Gamma = \int_0^S \gamma(s)ds \text{, or}$$

$$\Gamma = -\frac{aS^3}{6} \tag{B-8}$$

Substituting the results of equation (B-8) into equation (B-7) yields the equation for a parabolic distribution of vortex strengths along the surface of the body:

$$\gamma(s) = -\frac{6\Gamma}{S^3}s^2 + \frac{6\Gamma}{S^2}s \tag{B-9}$$

Appendix C

THE ABREAST PROGRAM

C.1. Introduction

This appendix introduces the Abreast program and explains how to set up a problem and obtain its solution.

The Abreast program was developed and used to apply the potential flow model to the flow through the experimental torque converter's 2nd turbine blade row. It uses a first order source-vortex panel method to calculate the potential flow field around one or several bodies in a freestream. The theory behind it is explained in chapter 3. The freestream can be specified as either uniform or radial. Options are available to distribute the vortex strength around each individual body either uniformly or parabolically for greater accuracy. Abreast is equipped with a tool for the creation of multiple element cascades based on a single base profile. This profile can be created in an Excel spreadsheet and imported via the Profile setting tool. Alternatively, simple bodies can be created in Abreast itself by means of a basic set of instructions called ABCOL (Abreast Command Language). It is also equipped with a tool for the quick creation of patterns of points in the flow field where the speed is calculated. Output is in the form of information written to a document that can be saved and in the form of elementary graphs that shows body shapes and pressure distributions.

C.2. Program installation and removal.

System requirements for the successful installation and operation of the program are:

- Microsoft Windows 98/Me/XP/2000
- PC with 200 MHz equivalent or higher processor

- 128 MB of system RAM for 2000/XP, 64 MB RAM for 98/Me
- 2 GB available hard disk space
- CD-ROM drive
- 4 MB video card
- Microsoft Mouse or compatible pointing device

The installation files are on a CD-ROM. Insert the installation CD in the CD-ROM drive and run the setup.exe program to activate the installation program. Follow the installation program's instructions. Together with the program files an Excel file with the name Profile.xls is installed in a sub-directory called Data Source Files. The program can be uninstalled by means of the standard Windows uninstall procedure which is usually found in the Windows Control Panel.

C.3. Specifying the problem.

After starting the program the flow problem to be solved needs to be specified in Abreast. The problem to be solved needs two groups of specifications to be properly specified in Abreast:

- The boundaries of the bodies in the freestream and
- The freestream particulars.

C.3.1. Boundary specification

The easiest way to specify the boundaries is by means of an Excel document from where the data can be loaded into Abreast. The Excel document's name must be Profile.xls and should preferably be placed in the same directory as the home directory of Abreast. Such a document was included in the installation and placed in a sub-directory called Data Source Files. This document can then be accessed from within Abreast by clicking on the Excel icon to activate it and then on the View icon to make it visible and use it. Table (C-1) shows an excerpt of one of the example sheets in the included Excel document to illustrate how the data must be entered into the sheet.

panel	Xb	Yb
1	0	0
2	0.00015	0.002170416
3	0.0005	0.003945478
4	0.001	0.005557469
5	0.0015	0.006785456
6	0.002	0.007814615
7	0.003	0.009528424
8	0.004	0.010960778
9	0.005	0.012213116
10	0.006	0.013337462

Table C-1. Example of a profile input data sheet.

As shown in table (C-1) three columns are used for data entry. The first column is used to number the panels, the second is used to enter the x-coordinate of the panel's start point and the third column is used to enter the y-coordinate of the panel's start point. The first row is used for descriptions and comments. From the second row onwards the profile is specified by entering the starting point coordinates of each panel. With the profile placed on a standard two-dimensional cartesian coordinate system, the panels must be specified sequentially in an anticlockwise direction starting with the panel where the Kutta condition is to be applied and ending with the other panel where the Kutta condition is to be applied. The numbering of the panels and the vertex points that must be entered to define the panels is illustrated in figure (C-1). When the panel start coordinates are entered into the spreadsheet, the spreadsheet should be given an appropriate name. The data is uploaded into Abreast by specifying the spreadsheet's name in Abreast in the Profile Data Sheet Name input box and then clicking on the Get Profile Data from Excel button just underneath it. The default profile number for this data will be 0. When more than one profile is specified, the option exist for loading the profile data under a different profile number. This can be chosen in the Active Profile list box near the top of the Profile Settings tool on the left of the screen.

For simple profiles settings or for minor changes to existing profiles, the ABCOL command *pbe, n, x, y* can be used. This will change the *x*- and *y*-coordinates of panel *n* on the active profile.

The minimum number of points that can be specified is two. This will ensure that the body formed by the panels is closed and will also provide enough panels for the application of the Kutta condition that is applied at two consecutive panels.

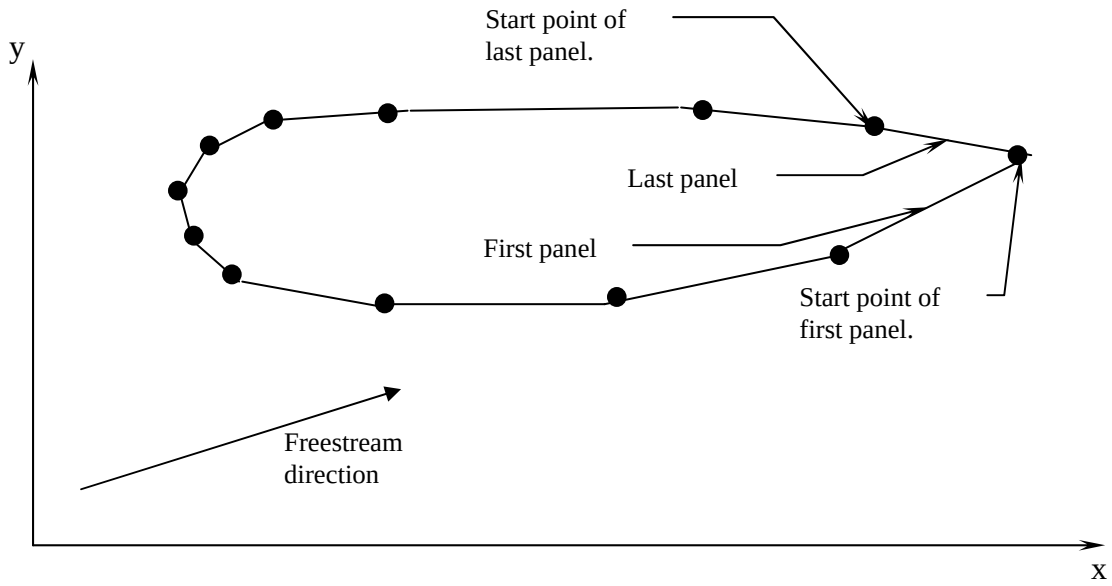

Figure C-1. Numbering method of a panelled body in the flow field.

Having registered the panel coordinates in Abreast, the next step is to specify the chord length of each profile. This is done by using the ABCOL command chl, *n*, *c* which enters the chord length *c* of profile *n* into Abreast. Alternatively the chord length can be entered into Abreast by specifying it into the appropriate input box in the Profile Settings tool. In the same frame the vortex strength distribution can also be picked. The choice is between constant and parabolic. The default value is a parabolic vortex strength distribution.

If the number of profiles in the profile configuration frame is specified as more than one, the choice of specifying these extra profiles at regular distances from the currently active profile is presented in the Daughter Profiles frame at the bottom of the Profile Setting tool. The profiles to be specified must be chosen in the Daughter Profiles list box. Then the choice between a circumferential and a linear arrangement of these profiles must be made. In the case of a circumferential arrangement the currently active profile is deemed to reside on the circumference of a circle with the centre at the origin of the two dimensional cartesian coordinate system used to

specify its panel coordinates. The arc subtending two consecutive profiles must then be specified in the Daughter Profile Arrangement frame. The panel coordinates of the daughter profiles will then be calculated at the specified arc intervals when the Create Daughter Profiles button is clicked. If the linear arrangement is chosen, the x- and y-direction offsets between each consecutive profile must be specified. When the Create Daughter Profiles button is clicked, the panel coordinates of the daughter profiles will then be calculated at the specified offsets. The first of these will be calculated with respect to the active profile. The next one will be offset again with respect to the previously created profile and so on. Each profile can be viewed on the graph by clicking on the appropriate profile number in the Active Profile Index Number box to make it the active profile.

C.3.2. Freestream specification

The freestream is specified by means of the Flow settings toolbox. This toolbox is activated by means of the Show Flow Settings Toolbox icon on the toolbar. In the Global Cp Reference Point frame the coordinates of the velocity with which the dimensionless pressure distribution on the profiles will be calculated are specified. In the Global Freestream Data frame a selection of the freestream type can be made between a uniform or a radial outflow freestream. In the case of a uniform freestream the speed and direction of the freestream velocity has to be entered. In the case of the radial outflow freestream the strength of the source has to be entered. Because the freestream must be irrotational, only basic potential flows are used to calculate them. The basic potential flow for a freestream that flows radially outward is a source based flow where the source is placed at the origin of the cartesian coordinate system used to specify the coordinates of the profile panels.

C.4. Calculating results.

To calculate the results the ABCOL command *res, n* is used. The parameter may be omitted in which case the results for all the profiles in the freestream are written to the output document. If the parameter is used, only the results for profile number *n* are written to the output document. The document can be saved. Results lists can

also be copied from it and pasted into an Excel spreadsheet for post-processing. The sample document Profile.xls that is installed with Abreast contains sample post processing spreadsheets that can be used for post processing.

A handy tool in Abreast is the Speed Query tool with which the velocity at a number of linearly or circumferentially distributed sampling points can be quickly calculated and displayed in the output document. The arrangement of the sampling points are specified in the same fashion as the arrangement of the new profiles in the Profile Setting tool.

C.5. ABCOL commands.

Several of the actions in Abreast is controlled by ABCOL commands. These commands are listed and briefly explained in table (C-2).

npr, n	Total number of profiles
pbe, n, x, y	Start coordinates of panel n of the active profile
vdi, n, linear/parabolic	Vortex strength distribution on the active profile surface panels
npa, n	Number of panels on a profile
cpx, x	x-co-ordinate of the reference point on which the pressure coefficients are calculated
cpy, y	y-co-ordinate of the reference point on which the pressure coefficients are calculated
fst, linear/radial	Freestream type: linear or radial
fsa, x	Freestream angle [degrees]
fss, x	Freestream speed (fst = linear) or source power (fst = radial)
pro, n	Set the active profile by its index number.
dat, n	Write the profile and freestream setup data into the output document.
res, n	Write the results of profile *n* into the output document.
lex	Load Excel profile workbook
uex	Unload Excel profile workbook
rex, n, *sheetname*	Read the panel start point coordinates of profile *n* from sheet *sheetname* in Profile.xls
cle	Clear output document.
chl, *profile*, *chordlength*	Set chord length of a profile.
rse, n	Reset profile n to zero or reset the whole setup if n is omitted.

Table C-2. ABCOL commands.